Joana Sofia Pereira Neto

Mestre em Engenharia Biomédica

Materials and neuroscience: validating tools for large-scale, high-density neural recording

Dissertação para obtenção do Grau de Doutor em Nanotecnologias e Nanociências

Orientador:	Doutor Pedro Miguel Cândido Barquinha, Professor auxiliar, Faculdade de Ciências e Tecnologia da Universidade Nova de Lisboa
Co-orientador:	Doctor Adam Raymond Kampff, Senior Research Fellow, Sainsbury Wellcome Centre, London, United Kingdom
	Júri:
Presidente:	Doutor Pedro Miguel Viana Baptista
Arguentes:	Doutor Henrique Leonel Gomes
	Doutor Alfonso Renart
Vogais:	Doutor Rui Alberto Garção Barreira do Nascimento Igreja
	Doutor João Carlos Azevedo Gaspar

FACULDADE DE CIÊNCIAS E TECNOLOGIA
UNIVERSIDADE NOVA DE LISBOA

Março 2018

Joana Sofia Pereira Neto

Mestre em Engenharia Biomédica

Materials and neuroscience: validating tools for large-scale, high-density neural recording

Dissertação para obtenção do Grau de Doutor em Nanotecnologias e Nanociências

Orientador:	Doutor Pedro Miguel Cândido Barquinha, Professor auxiliar, Faculdade de Ciências e Tecnologia da Universidade Nova de Lisboa
Co-orientador:	Doctor Adam Raymond Kampff, Senior Research Fellow, Sainsbury Wellcome Centre, London, United Kingdom
	Júri:
Presidente:	Doutor Pedro Miguel Viana Baptista
Arguentes:	Doutor Henrique Leonel Gomes
	Doutor Alfonso Renart
Vogais:	Doutor Rui Alberto Garção Barreira do Nascimento Igreja
	Doutor João Carlos Azevedo Gaspar

FACULDADE DE CIÊNCIAS E TECNOLOGIA
UNIVERSIDADE NOVA DE LISBOA

Março 2018

Materials and neuroscience: validating tools for large-scale, high-density neural recording

This work was developed in the context of the Nanotechnology and Nanoscience PhD program, in collaboration with the Champalimaud Research Programme, Champalimaud Center for the Unknown, Lisbon, Portugal. The project was carried out at Departamento de Ciência dos Materiais, CENIMAT/I3N and CEMOP/Uninova, Caparica, Portugal, Champalimaud Center for the Unknown, Lisbon, Portugal, and Sainsbury Wellcome Centre, University College London, London, United Kingdom.

This work was supported by funding from the European Union's Seventh Framework Programme (FP7/2007-2013) under grant agreement nr. 600925, and by the the Bial Foundation (Grant 190/12). Joana Neto was supported by the fellowship SFRH/BD/76004/2011 from Fundação para a Ciência e Tecnologia, Portugal, and a Visiting Research Fellow stipend from Sainsbury Wellcome Centre, University College London, London, United Kingdom.

‘Sempre chegamos ao sítio aonde nos esperam’

José Saramago, *A Viagem do Elefante*

Acknowledgements

The work presented in the next pages was developed through six years in two countries and three institutes. During this journey I had the privilege of meeting and working with extraordinary people from different academic backgrounds, what made this journey an exciting and rich learning experience.

First, I was given the unique opportunity to collaborate with the neuroscience community on the other side of the river. To Prof. Dr. Elvira Fortunato and Prof. Dr. Rodrigo Martins, I want to thank for the support given to bridge two different fields, materials science and neuroscience. To Pedro Barquinha, I want to thank for accepting me as a student and taking up this project. For his kindness and guidance during this journey.

To all my colleagues and friends from CENIMAT, DCM, Champalimaud Center for the Unknown and Sainsbury Wellcome Centre, I want to thank for all their support during this research. I have to give thanks to Lídia Santos, Joana Vaz Pinto and Tiago Monteiro for the enthusiastic and honest collaborations.

I also want to express my gratitude to the students who have collaborated with me and provided contributions for this work. I am grateful to Msc. Pedro Baião, Msc. Pedro Lacerda, Msc. Kinga Kocsis, Msc. Ana Crespo, Msc. Nuno Coelho, Msc. Júlio Costa, Msc. João Rosa, and Msc. Jesse Geerts.

Throughout these years, a lot of days and nights, were spent in the Intelligent Systems Lab. I have to give thanks to Gonçalo Lopes, the guy with a brig brain and even more bigger heart. This work was only possible because he was always there to help me. Also to Joana Nogueira and Lorenza Calcaterra, who always stayed with me, helped me during long surgeries, and made sure I was still breathing. To João Frazão, the guy who is 'always right' and helped me to overcome uncountable challenges. To George Dimitriadis, who taught me a lot about programming and the 'knows' and 'unknowns' in neuroscience. To Ataback Dehban, Danbee Kim and André Marques-Smith for the companionship and fruitful discussions.

To Adam R. Kampff for being a believer. He believed, even when I had myself lost hope. Thank you, for showing me, since the first day, the importance of opening 'black boxes'. Also, I want to thank him for the support and guidance in the experiments design, interpretation of results, and manuscripts writing.

Finally, I want to thank to my family for all the patience and love, and to Guilherme, for understanding and supporting my love for science.

Abstract

Extracellular recording remains the only technique capable of measuring the activity of many neurons simultaneously with a sub-millisecond precision, in multiple brain areas, including deep structures. Nevertheless, many questions about the nature of the detected signal and the limitations/capabilities of this technique remain unanswered.

The general goal of this work is to apply the methodology and concepts of materials science to answer some of the major questions surrounding extracellular recording, and thus take full advantage of this seminal technique.

We start out by quantifying the effect of electrode impedance on the amplitude of measured extracellular spikes and background noise. Can we improve data quality by lowering electrode impedance? We demonstrate that if the proper recording system is used, then the impedance of a microelectrode, within the range typical of standard polytrodes (~ 0.1 to 2 MΩ), does not significantly affect a neural spike amplitude or the background noise, and therefore spike sorting. In addition to improving the performance of each electrode, increasing the number of electrodes in a single neural probe has also proven advantageous for simultaneously monitoring the activity of more neurons with better spatiotemporal resolution. How can we achieve large-scale, high-density extracellular recordings without compromising brain tissue? Here we report the design and *in vivo* validation of a complementary metal–oxide–semiconductor (CMOS)-based scanning probe with 1356 electrodes arranged along approximately 8 mm of a thin shaft (50 μm thick and 100 μm wide). Additionally, given the ever-shrinking dimensions of CMOS technology, there is a drive to fabricate sub-cellular electrodes (< 10 μm). Therefore, to evaluate electrode configurations for future probe designs, several recordings from many different brain regions were performed with an ultra-dense probe containing 255 electrodes, each with a geometric area of 5 x 5 μm and a pitch of 6 μm.

How can we validate neural probes with different electrode materials/configurations and different sorting algorithms? We describe a new procedure for precisely aligning two probes for *in vivo* "paired-recordings" such that the spiking activity of a single neuron is monitored with both a dense extracellular silicon polytrode and a juxtacellular micro-pipette. We gathered a dataset of paired-recordings, which is available online. The "ground truth" data, for which one knows exactly when a neuron in the vicinity of an extracellular probe generates an action potential, has been used for several groups to validate and quantify the performance of new algorithms to

automatically detect/sort single-units.

Resumo

A gravação extracelular é a única técnica que permite a medição da atividade de vários neurónios simultaneamente, em várias áreas do cérebro (incluindo estruturas profundas), com uma precisão temporal de sub-milisegundos. Todavia, permanecem sem resolução várias questões concernentes à natureza do sinal detetado e às capacidades/limitações desta técnica.

O presente trabalho visa a apresentação de respostas a algumas das principais questões por solucionar relacionadas com a gravação extracelular de atividade neuronal, recorrendo para o efeito, à aplicação de metodologia e conceitos da ciência dos materiais.

Uma das questões à qual se procurou responder é relativa ao efeito da impedância do microelétrodo na amplitude dos potenciais de ação e do ruído de fundo. Podemos aumentar a qualidade do signal ao diminuir a impedância do elétrodo? Através do presente projeto demonstrámos que, utilizando-se um sistema de gravação apropriado, a impedância de um microelétrodo, dentro do intervalo típico dos elétrodos comerciais (~ 0.1 a 2 MΩ), não afeta significativamente a amplitude do potencial de ação ou o ruído de fundo e, consequentemente, a atribuição de cada potencial de ação ao respetivo neurónio.

Não se afigura, porém, apenas relevante melhorar o desempenho de cada elétrodo individualmente, sendo fundamental o aumento do número de elétrodos numa única sonda neural, por forma a permitir a monitorização simultânea da atividade de um número mais elevado de neurônios com melhor resolução espaciotemporal. Como podemos alcançar gravação extracelular de alta escala e densidade sem comprometer o tecido cerebral? Visando esse propósito descrevemos o design e validámos *in vivo* uma sonda de varredura baseada em tecnologia CMOS com 1344 elétrodos e 12 elétrodos de referência, dispostos ao longo de uma agulha fina (50 µm de espessura e 100 µm de largura) com aproximadamente 8 mm de cumprimento.

Considerando as dimensões cada vez menores alcançadas com a tecnologia CMOS, verifica-se uma tendência para fabricar elétrodos cada vez menores, com dimensões sub-celulares (<10 µm). Com efeito, para avaliar possíveis configurações dos elétrodos tendo em vista a produção de futuras sondas, realizámos gravações de diferentes áreas do cérebro com uma sonda ultradensa contendo 255 elétrodos, cada um dos quais com uma área geométrica de 5 x 5 µm e distância centro-a-centro de 6 µm.

Coloca-se, assim, a questão de como avaliar sondas com diferentes configurações de elétrodos e

diferentes algoritmos de classificação? Como resposta a esta questão descrevemos um novo procedimento para alinhar, com precisão, duas sondas para, posteriormente, gravar *in vivo* com ambas a atividade de um único neurónio, uma das quais uma agulha de silício com uma matriz densa de elétrodos e a outra uma micro-pipeta *juxtacelular*. Reunimos um conjunto de gravações nas quais ambas as sondas detetam o sinal do mesmo neurónio, as quais foram disponibilizadas *on-line*. As referidas gravações nas quais se obtiveram sinais extracelulares em que se mediram os potenciais de ação gerados por um neurônio na proximidade, foram utilizadas por vários grupos para avaliar e quantificar o desempenho de novos algoritmos com vista à deteção/classificação de neurónios.

Contents

List of Figures

List of Tables

Abbreviations

AC	alternating current
ADC	analog-to-digital converter
Ag-AgCl	silver-silver chloride electrode
AP	action potential
B	bregma
c	cortex
CE	counter electrode
cg	cingulum
CIS	CMOS image sensor
CMOS	complementary metal-oxide-semiconductor
DAC	digital-to-analog converter
DC	direct current
DMUX	de-multiplexer
EDL	electrical double layer
EIS	electrochemical impedance spectroscopy
FET	field-effect transistor
fs	sampling frequency
G1 to G12	group 1 to group 12
GND	ground
GPU	graphics processing unit
h	hippocampus
HD	high definition
IA	interaural line
IC	integrated circuit
IM	intramuscular
IP	intraperitoneal
ISI	interspike interval
IVM	in-vivo manipulator
JTA	juxtacellular triggered average
LFP	local field potential
MOS	metal-oxide-semiconductor

MOSFET	metal-oxide-semiconductor field-effect transistor
MUX	multiplexer
NMOS	n-channel metal-oxide-semiconductor
P2P	peak-to-peak amplitude
PBS	phosphate buffer saline solution
PCB	printed circuit board
PEDOT-PSS	poly(3,4-ethylenedioxythiophene) - polystyrene sulfonate
PETH	peri-event time histogram
PMOS	p-channel metal-oxide-semiconductor
PS	patchstar
RE	reference electrode
RMS	root-mean-square
SC	subcutaneous
SCE	saturated calomel electrode
SEM	scanning electron microscopy
SHE	standard hydrogen electrode
SNR	signal-to-noise ratio
t	thalamus
t-sne	t-student stochastic neighbour embedding
WE	working electrode

Symbols

Au	gold
C_d	capacitance of an ideal polarized electrode
C_e	capacitance of the electrical double layer
C_i	capacitance of the integrating capacitor
C_{SCE}	capacitance of an SCE electrode (reference electrode)
C_{sh}	shunt capacitance to ground from the electrode to the input of the amplifier
d_1	thickness of the Helmholtz layer
E	voltage source
f_1 and f_2	lower and upper limits of frequency bandwidth
i	current measured
I	current source
Ir	iridium
IrO_x	iridium oxide
k	Boltzmann's constant
K^+	potassium ion
Na^+	sodium ion
Pt	platinum
R_e	leakage resistance due to charge carriers crossing the electrical double layer
r_e	position in space where potential V_e is measured
R_m	resistance of the metallic portion
R_s	resistance of the solution
R_{sh}	shunt resistance to ground from the electrode to the input of the amplifier
R_z	resistance of a large resistor
T	temperature
T_i	integration time
TiN	titanium nitride
V	potential measured
V_e	potential created in the volume conductor with respect to a point at infinity
$V_{e'}$	potential at the input of the amplifier from the electrode
V_{rec}	potential difference between $V_{e'}$ and $V_{ref'}$
V_{ref}	potential on the reference electrode

V_{ref}	potential at the input of the amplifier from the reference
X, Y and Z	axes
Z	impedance
Z’	real part of the impedance
Z”	imaginary part of the impedance
Z_{a}	amplifier input impedance
Z_{a_e}	effective amplifier input impedance for the electrode
Z_{a_ref}	effective amplifier input impedance for the reference
Z_{e}	effective electrode impedance
Z_{ref}	effective reference impedance
ρ	extracellular conductivity
σ	background noise
Φ	electric potential
φ	phase shift
ω	angular frequency (rad s^{-1})
⊣⊢	capacitive current

Chapter 1. Motivation

Summary

In this dissertation we focus on extracellular recording, the oldest technique used to measure brain activity. Extracellular microelectrodes are used to measure the activity of neurons from outside the cell membrane at the sub-millisecond time scale. Recently, neural probes with thousands of microelectrodes have become available, allowing one to simultaneously observe the activity of hundreds, or even thousands, of neurons. Despite these incredible technological advances, many questions about the nature of the detected signal and the limitations of this technique remain unanswered. Hence, the motivation for this work arrives from the need to better understand the neural probes used for large-scale, high-density extracellular recordings, and thus explore their full potential. Finally, this chapter ends with overall research goals and an outline of the thesis.

1.1 Scientific context: sensing neuronal activity from the extracellular space

We currently lack a theory describing how the brain works (Krioukov, 2014). Efforts have thus focused on creating techniques and tools capable of advancing our understanding of the physiological properties of the nervous system. Today, extracellular recording remains the only technique capable of measuring the activity of many neurons simultaneously with sub-millisecond precision in multiple brain areas, including deep structures (e.g., thalamus).

In the 1920s, Edgar Adrian measured extracellularly the signals transmitted to the brain from single sensory nerve fibres, and described how these signals were related to the stimulus which produced them (i.e., pressure on the muscle). These signals were found to use a common vocabulary. They consisted of a series of brief and uniform changes in electric potential (so-called action potentials or spikes) (Adrian, 1928).

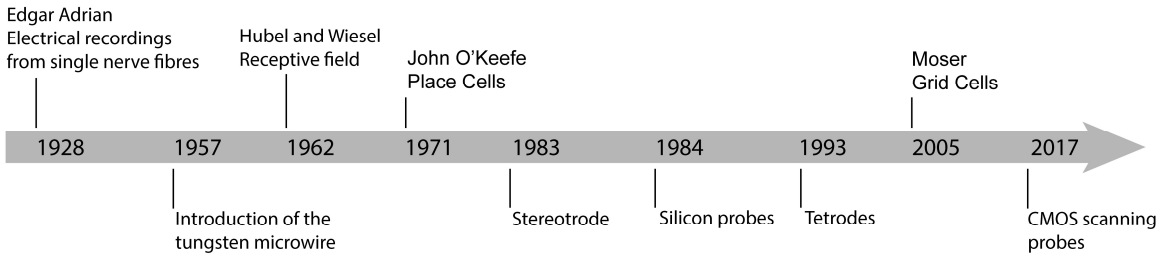

Figure 1.1 Historical summary highlighting the ties between tools and discoveries in neuroscience. The development of extracellular microelectrodes enabled researchers to monitor the activity pattern of individual neurons in relation with external stimuli and behavior. The diagram shows the introduction of new tools (Hubel, 1957; McNaughton, O'Keefe, & Barnes, 1983; Najafi, Wise, & Mochizuki, 1985; O'Keefe & Recce, 1993; Takahashi & Matsuo, 1984; Wilson & McNaughton, 1993) together with the key findings resulting in Nobel Prize awards in neuroscience (Adrian, 1928; Hubel & Wiesel, 1962; O'Keefe & Dostrovsky, 1971; Hafting, Fyhn, Molden, Moser, & Moser, 2005). Adapted from Yuste, 2015.

Since Adrian, quantifying brain activity (spikes from individual cells), and its relationship to sensory and behavioural variables, has become the cornerstone for understanding brain function (Hafting et al., 2005; Hubel & Wiesel, 1962; O'Keefe & Dostrovsky, 1971). A thin insulated metal microwire with an exposed tip have become the tool of choice to measure action potentials of single neurons in the brains of behaving animals, since pioneering studies of the 1950s (Figure 1.1). The focus on the properties of individual neurons was a natural consequence of the use of a single microelectrode (Hubel, 1957). Over the years, technological progress has contributed to a move from microwires (McNaughton et al., 1983; O'Keefe & Recce, 1993) to microfabricated silicon probes with dozens of microelectrodes, also called polytrodes (Najafi et al., 1985; Takahashi & Matsuo, 1984).

Today, CMOS-based probes with thousands of microelectrodes packed in a high-density array are being developed using modern methods for integrated circuit design and fabrication. Why do researchers need thousands of microelectrodes? The number of simultaneously identified neurons in a single experiment largely depends on the number of individual microelectrodes on the neural probe (Stevenson & Kording, 2011) and many neuroscientists hope that simultaneously monitoring the activity of more individual neurons will help us to understand how the constituent parts of the nervous system lead to the emergent properties of the whole behaving organism (Buzsáki, 2004). A helpful metaphor is our visual comprehension of an image presented to us on a computer screen. Imagine that someone is trying to comprehend the image by looking at individual random pixels. This task is almost impossible to accomplish with view of only a small number of pixels, and to decipher the image, it is important to simultaneously view as many pixels as possible (Yuste, 2015).

However, one must remember that extracellular recordings are an imperfect representation of the underlying neuronal activity (Harris, Quiroga, Freeman, & Smith, 2016; Moore-Kochlacs, 2016; Shoham, O'Connor, & Segev, 2006). Each microelectrode captures a mixture of activity from multiple neurons together with noise. Noise sources, both of biological (e.g., electric activity from neurons further away the recording microelectrode) and non-biological (e.g., thermal noise) origin, contribute for the background noise.

"What contributes to the amplitude of action potentials as well as the background noise? Can we improve data quality by physical design choices (e.g., the individual microelectrode impedance and size)? How will these be reflected in the subsequent sorting analysis? What arrangement of electrodes is optimal for isolating individual neurons from background noise? How can we validate probes with different electrode configurations and different sorting algorithms? How can we achieve the full potential of large-scale, high-density extracellular recordings?"

This work aims to settle such questions as they relate to extracellular recording, and to help researchers take full advantage of this seminal technique.

1.2 Research goals

In order to understand and achieve the full potential of neural probes (with dozens, or even thousands, of microelectrodes) used for large-scale, high-density extracellular recordings, the research was split into four main tasks:

1) Identify the factors that govern the efficiency of signal transfer from the neuronal activity into digital recorded voltages;

2) Quantify the effect of electrode impedance on the amplitude of measured extracellular spikes and background noise;

3) Validate a large-scale, ultra-high density CMOS-based probe developed in collaboration with the NeuroSeeker consortium. These CMOS probes represent a major innovation, but also a major challenge for current analysis methods. Additionally, due to the ever-shrinking dimensions of CMOS technology, validate electrode configurations for future probe designs;

4) Develop a method for efficiently gathering "ground truth" data to quantify the performance of different electrode configurations and spike sorting methods.

1.3 Thesis outline

The structure of the work presented in this dissertation follows the order of the tasks described above, and in each of the chapters we set out to accomplish one of the mentioned tasks.

In Chapter 2 we provide some fundamental background regarding the operating principles of extracellular recording, highlighting the factors that can affect the extracellular recording voltages, and subsequent analysis.

In Chapter 3 we discuss how a commercial electrode impedance affects data quality in spikes recording. We compare, side-by-side, the same extracellular signals measured by coated (low impedance) microelectrodes and non-coated (high impedance) microelectrodes.

In Chapter 4 we report the design and *in vivo* validation of a CMOS-based scanning probe with 1356 electrodes arranged along approximately 8 mm of a thin shaft. We also present new methods for analysing large-scale extracellular recordings. Additionally, to evaluate electrode configurations for future probe designs (i.e., electrode size, density and geometry), several recordings from many different brain regions were performed with an ultra-dense probe containing 255 electrodes, each with a geometric area of 5 x 5 μm and a pitch of 6 μm.

In Chapter 5 we describe a procedure for precisely aligning two probes for *in vivo* "paired-recordings" such that the spiking activity of a single neuron is monitored with both a dense extracellular silicon polytrode and a juxtacellular micro-pipette.

Finally, in Chapter 6 we discuss the implications of our experimental findings and the future of extracellular recordings.

Chapter 2. General Introduction

Summary

Herein, our goal is to make intelligible the factors that govern the efficiency of signal transfer, from the brain to a digital record using extracellular recordings. Therefore, we provide some fundamental background regarding the operating principles of extracellular recordings and the electrode-brain interface. We also describe the challenges for analysis of an extracellular recording. Finally, this chapter ends with a brief historical perspective on extracellular microelectrodes, and the new technologies that will probably shape the field of recording tools for brain research.

2.1 In Brief

Figure 2.1 frames the introduction and will serve as a guide throughout the discussion of different topics in this chapter.

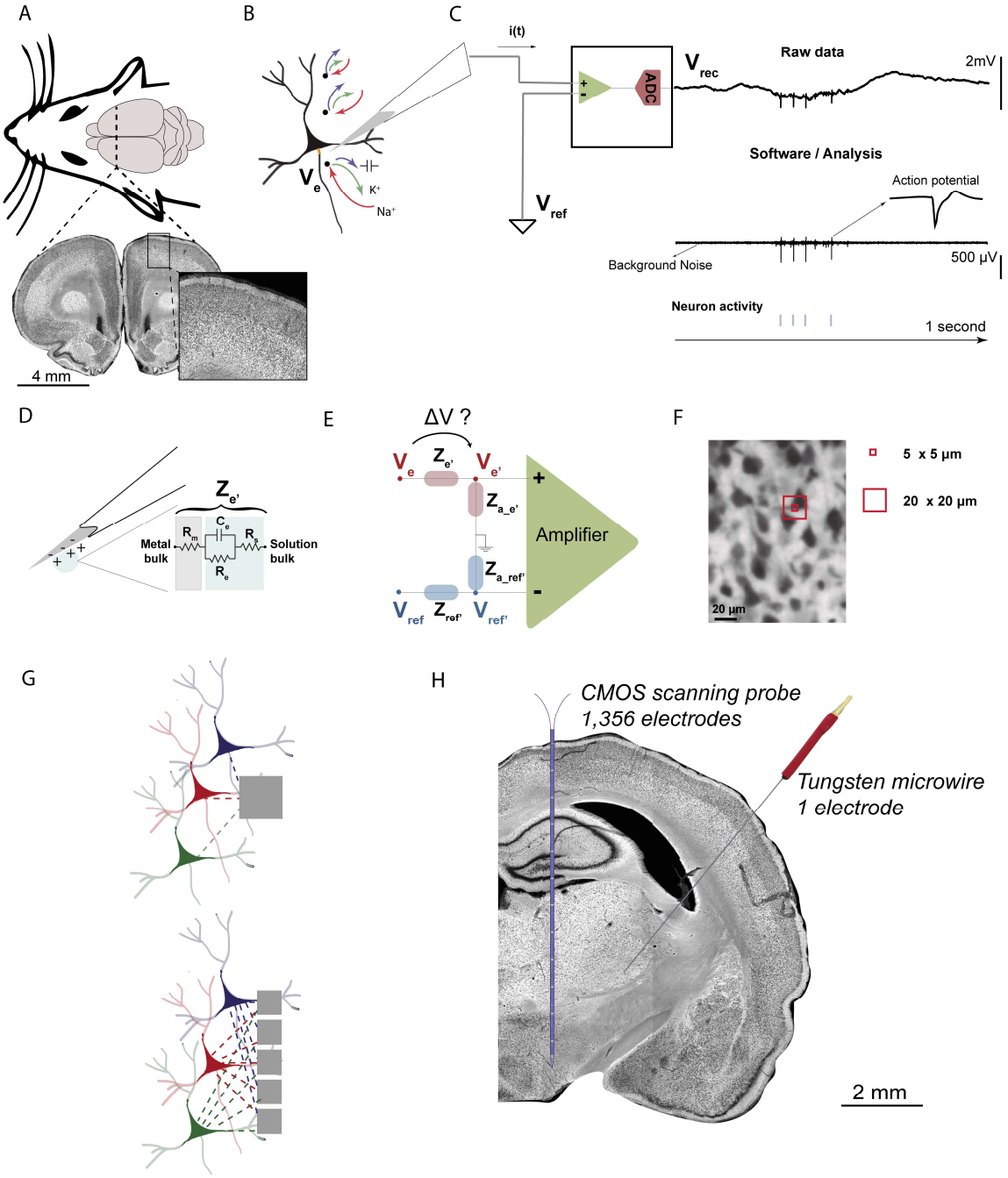

Figure 2.1 Graphical overview of the introduction where each panel highlights the main topics discussed throughout Chapter 2. (a) 2.2 Brain, neurons and extracellular space; (b) 2.3 Neuronal activity, extracellular currents and potentials; (c) 2.4 Extracellular recording systems; (d) 2.5 Microelectrode-extracellular space interface and impedance measurement; (e) 2.6 Effects of the electrode impedance on data quality; (f) 2.7 Effects of electrode size on data quality; (g) 2.8 Effects of electrode density on spike sorting algorithms; (h) 2.9 Large-scale recording of neuronal activity.

Neurons are the building blocks of the brain, and they are connected together into networks that process information within milliseconds. Figure 2.1a shows a section of the rat brain (our model organism) where each densely packed dot is a neuron cell body. Brain tissue comprises neural cell bodies (somas), connecting fibres (axons and dendrites), glial cells, and blood vessels.

When a neuron is active, transient changes in its membrane cause currents (ionic and capacitive) to flow into and out of the cell (Figure 2.1b). The strongest and fastest currents across the neural membrane are caused by Na^+ ions rushing into the cell at the start of an action potential, followed by an outward flow of K^+, which co-occurs with a small capacitive current across the entire cell membrane as the membrane is charged by the influx of Na^+ ions at the initial segment of the axon (marked in orange). Each of these transmembrane currents superimpose in the extracellular medium (which acts as a volume conductor), defining an electric potential field. To detect the presence of an active neuron, we measure the electric potential (V_e) in the extracellular space near the neuron, relative to some distant reference. The activity of a neuron generates a stereotypical temporal deflection of the electric potential, known as an extracellular action potential, or a spike. The largest electric potential deflection occurs near the initial segment of the axon.

Therefore, in extracellular recordings, the recorded voltage (V_{rec}) reflects the potential difference between a microelectrode that is usually inside the brain, close to neurons, and the reference electrode. Our goal is to position our recording electrode as close as possible to the soma. Note that the recorded signal imperfectly represents what is happening around the cell because each electrode captures the spiking activity of several neurons in its vicinity together with noise. Moreover, the recorded electric potential will also depend on the recording system. Currently, the entire recording system is composed of the microelectrode(s), reference electrode and the hardware connected to them, including amplifiers, filters and analog-to-digital converters (ADCs) (Figure 2.1c). The amplification of the potential difference between the microelectrode and the reference electrode (on the order of microvolts) is a crucial step, and is accomplished with differential amplifiers that amplify the differences, rejecting the noise that is often introduced as common-mode potential in the circuit.

The mechanism that underlies the transduction of the neuronal activity into recorded voltages begins with the electrode-extracellular interface. In Figure 2.1d the effective electrode impedance (Z_e) is the sum of the resistance of the solution (R_s), the resistance of the electrode metal (R_m), and the resistance (R_e) and capacitance (C_e) of the double-layer that forms on the metal electrode-extracellular interface (i.e., the charge on the metal is equal and opposite to the total charge on the extracellular side of the interface).

The quality of the data depends on the amplitude of the extracellular action potentials relative to the background noise. What then contributes to the amplitude of the observed action potentials, as well as the background noise? One common confusion is how the electrode impedance affects the recorded signal, and therefore spike's amplitude. To better understand the voltage drops and current pathways that occur in a recording system, a simplified circuit is shown in Figure 2.1e. The effective electrode impedance (Z_e) and effective amplifier input impedance (Z_{a_e}) form a voltage divider. The effective amplifier input impedance is the total impedance to ground, as seen from the electrode, and it includes a path through the amplifier and shunting routes to ground. Therefore, as long as the input impedance amplifier is larger than the impedance of the electrode-extracellular interface, the voltage drop in the electrode-extracellular interface is neglected and the potential difference at the amplifier inputs should reflect the actual difference in electric potential, $V_e - V_{ref}$.

A separate question from whether the impedance of an electrode influences the recorded voltage, is the question of whether the size of the recording site has an impact on the recorded spikes. Larger electrodes can reduce the signal amplitude due to the averaging with nearby regions with smaller signals. High density arrays of small electrodes (5-20 μm) can reduce spatial averaging of action potentials and increase the probability of finding "the sweet spot" near a neuron's soma (Figure 2.1f). When using small electrodes, the only limiting factor is electrode noise, which scales as a factor of size. How small can you make recording electrodes? Decreasing electrode size lowers electrode capacitance and increases its resistance, both increasing impedance, which increases thermal noise. On top of the thermal noise, biological noise (i.e., the activity of many distant neurons) also adds to the noise background magnitude.

The data quality is important for the subsequent steps of detection and isolation where spike sorting algorithms extract and identify the activity of individual neurons from the extracellular voltage traces. In our recording devices, besides the impedance and size of electrodes, another physical design choice, can play an important role in the subsequent analysis - the density and arrangement of the electrodes (Figure 2.1g). What arrangement of electrodes is optimal for isolating individual neurons from background activity?

To understand how the brain works, possibly we will need to simultaneously record and analyse a large number of neurons from different brain areas. Extracellular probes have been fabricated with an increasing number of electrodes in order to capture the activity of an increasing number of neurons. In 2017, the European project NeuroSeeker resulted in the development of probes with 1356 electrodes on a single 8 mm shank, which allowed us to record *in vivo* the activity of hundreds of neurons across several structures in the brain (Figure 2.1h).

2.2 Brain, neurons and extracellular space

In the eighteenth century, the individual components of which the whole brain is built were finally revealed by Santiago Ramón y Cajal under the microscope, after adapting the Golgi staining protocol (Kandel, Schwartz, & Jessel, 2000). In *Texture of the Nervous System of Man and the Vertebrates*, Ramón y Cajal presented detailed drawings of brain cells scattered across different brain regions (Ramon y Cajal, 1899). In Figure 2.2b we can see several connecting fibres (dendrites and axon) growing out from the cell body. Each neuron may establish direct contact with thousands of other neurons through specialized communication sites called synapses. In general, each neuron receives input from many other neurons through dendritic synapses, while sending its own output through the axon, which can establish synapses with a large population of other brain cells (Eccles, 1973). In Figure 2.2a only the neuron cell bodies are stained black, unlike the Golgi staining used by Ramón y Cajal (Figure 2.2b). If all the dendrites and axons from every neuron were stained in a slice of brain tissue, the result would be a solid black picture. A rat brain has about 200 million (and a human brain has about 86 billion) neurons tightly packed together (Azevedo et al., 2009; Herculano-Houzel, 2009). The density in the rat cortex, according to the literature, is between 40,000 to 100,000 neurons per mm^3 (DeFelipe, Alonso-Nanclares, & Arellano, 2003; Markram et al., 2015; Meyer et al., 2010). In addition to neuronal cell bodies, axonal fibres, and dendritic structures, the brain also contains glial cells and blood vessels. Thus very little of the extracellular space is actually "space". Indeed, extracellular fluid is thought to comprise only 12–25 % of the brain's volume (Li et al., 2015; Nelson, Bosch, Venance, & Pouget, 2013; Tønnesen, Inavalli, & Nägerl, 2018).

Cajal once described the brain as an 'impenetrable jungle where many investigators have lost themselves' (Ramon y Cajal, 1923). However, it is through these large and distributed neural networks that the brain runs, builds and stores detailed models of the world, and continuously adapts them to new environments (Nicolelis, 2011).

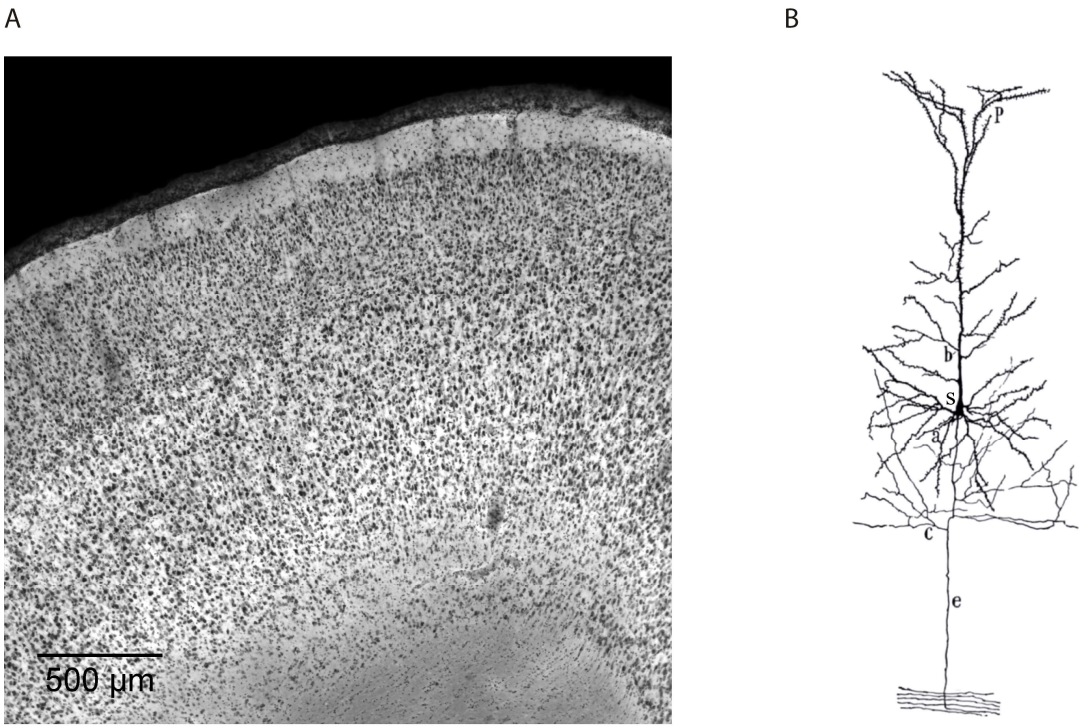

Figure 2.2 Neurons: the building blocks of brains. (a) Nissl-stained section of the rat cortex. All neuron cell bodies (somas) are stained; (b) Drawing by Ramon y Cajal from pyramidal cell of the rabbit cerebral cortex. In the pyramidal cell, 'a': basal dendrites, 'b': dendritic trunk and its branches, 'c': axon collaterals, 'e': long axon, 'P': apical dendrites, and 's': soma. Adapted from Ramon y Cajal, 1899. More recent studies on cortex cell morphology and function are available (Jiang et al., 2015; Markram et al., 2015).

2.3 Neuronal activity, extracellular currents and potentials

Neuronal activity gives rise to transient changes in the flow of current into and out of the cell. Briefly, when an input signal (a receptor potential or synaptic potential) depolarizes the cell membrane, this change in membrane electric potential opens Na^+ ion channels, allowing Na^+ to flow from outside the cell, where the Na^+ concentration is high, to the inside of the cell, where Na^+ concentration is low (Kandel, Schwartz, & Jessel, 2000). In neurons, voltage-sensitive Na^+ channels are usually concentrated at the initial segment of the axon (marked in orange in Figure 2.1b). Therefore, it is more likely that the action potential arises at the initial segment of the axon, rather than in other regions of the cell. The sudden influx of Na^+ ions through these voltage-sensitive channels in the cell membrane upsets the balance of processes that maintain the neuron at its resting equilibrium, and leads to a series of further changes which constitute the action potential (Hodgkin & Huxley, 1939).

All of the transmembrane currents within a volume of brain tissue superimpose in the extracellular medium (r_e), and generate a potential, V_e (a scalar measured in Volts), with respect

to a point at infinity (Figure 2.3). By infinity we mean a location that is far from all of the sources of electric potential (Einevoll, Kayser, Logothetis, & Panzeri, 2013). The electric field and therefore the potential V_e induced in a volume conductor by the transmembrane currents depends on the magnitude, sign and location of the current sources, and on the conductivity of the extracellular medium (Buzsáki, Anastassiou, & Koch, 2012; Nunez & Srinivasan, 2009).

Figure 2.3 depicts the time-varying extracellular potential at given locations (r_e) that resulted from the superposition of the ionic and capacitive transmembrane currents formed when a neuron was active. The difference in potential waveforms at different locations in the extracellular medium is mainly given by the shape of the net current (Figure 2.3, first column) across the membrane. Furthermore, the peaks in the potential waveforms correspond to the current (Figure 2.3, second column) that is dominant at that time-point: the first positive peak of the waveform is attributed to the positive capacitive current resulting from the strong Na^+ current entering the axon initial segment; the main negative peak is attributed to the influx of Na^+; and finally, the second positive peak results from repolarizing K^+ current flowing out of the cell (Gold, Henze, Koch, & Buzsáki, 2006).

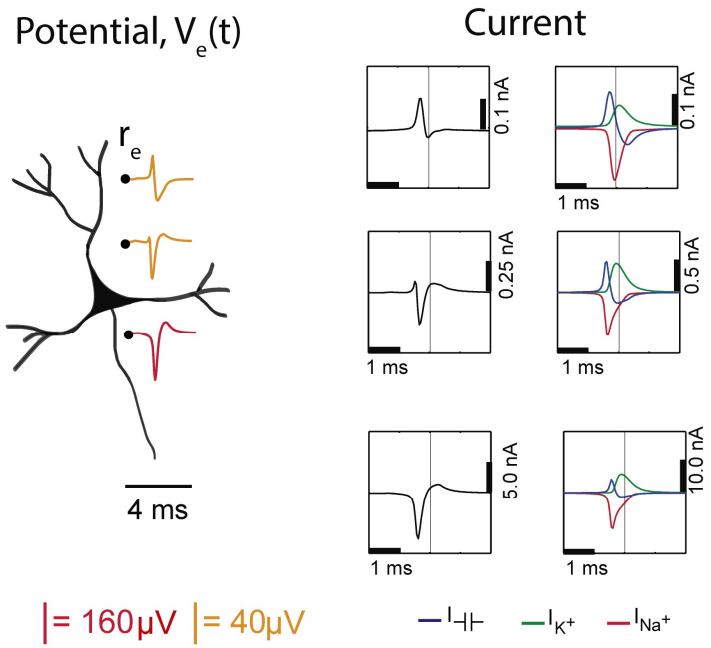

Figure 2.3 Electric potential generated by current sources in a conductive volume. The extracellular potentials and currents are adapted from Gold et al., 2006. Extracellular potential waveforms at selected spatial positions, r_e (marked with black dots) are simulated for a CA1 pyramidal neuron. Currents: simulated net membrane current (first column) across the soma and proximal dendrites that best estimates the extracellular potential waveform and membrane current components in terms of Na^+, K^+ and capacitive currents (second column). In the soma, the positive capacitive current coincides with the larger Na^+ current. At locations along the apical trunk, the initial capacitive peak becomes visible. In dendritic compartments the membrane depolarization is initially driven by Na^+ current from the soma, until local Na^+ currents are activated and the action potential regenerates. In the brief time before the local Na^+ currents activate, the positive capacitive current is the dominant membrane current and a capacitive-dominant phase is visible in the net current (Gold et al., 2006).

In more detail, the extracellular potential V_e at position r_e can be computed with the following equation, described in several works (Einevoll et al., 2013; Nunez & Srinivasan, 2009; Pettersen, Lindén, Dale, & Einevoll, 2010), as:

$$V_e(r_e, t) = \frac{1}{4\pi\rho} \sum_{n=1}^{N} \frac{I_n(t)}{|r_e - r_n|}$$

Equation 2.1

Conceptually, the point-source equation (Equation 2.1) is key for computing the extracellular potential in response to any transmembrane current (Buzsáki et al., 2012). $I_n(t)$ represents the n^{th} point current source and $r_e - r_n$ represents the distance between the point source and the position of measurement, with n = 1...N, where N is the number of individual point sources and ρ is the extracellular conductivity. If the extracellular medium is considered homogeneous and isotropic that means a constant conductivity value (Einevoll et al., 2013).

Therefore, to detect the presence of an active neuron nearby in the extracellular space, the electric potential relative to some distant reference point must be measured. The model presented in Figure 2.3 illustrate how the electric potential varies nearby an active neuron. The extracellular potential waveforms usually last on the order of 1-2 ms, and are in the range of tens to hundreds of microvolts in amplitude, with the largest potential deflections being detected close to the soma of a neuron. These stereotypical temporal deflection of the electric potential in the extracellular space are called action potentials or spikes.

2.4 Extracellular recording systems

In Figure 2.1c, an extracellular recording in rat cortex under anesthesia is represented as V_{rec}. This voltage trace contains 40–500 μV action potentials (1 ms wide) from a population of neurons nearby, as well as slower fluctuations that range from tens to thousands of microvolts. The low-frequency band of the recorded signal (< 300 Hz) contains local field potentials (LFPs) that reflect synchronized synaptic currents. The idea that synaptic currents contribute to the LFP stems from the recognition that extracellular currents from many individual neurons must overlap in time to induce a measurable signal, and such overlap is most easily achieved for relatively slow events, such as synaptic currents (Buzsáki et al., 2012; Einevoll et al., 2013). Since, our focus is on the fast voltage deflections known as spikes, the lower frequency signal is separated from the spike

signal by high-pass filtering around 250 Hz (Buzsáki et al., 2012; Schomburg, Anastassiou, Buzsáki, & Koch, 2012).

As shown in Figure 2.1b and c, the voltage measured (V_{rec}) should reflect the potential difference between a microelectrode close to a neuron and a reference electrode at a much larger distance from all the current sources. The potentials V_e and V_{ref} are the potentials just below the electrodes' interface and are also the voltages impressed at the microelectrode and reference, respectively. As mentioned above in **2.3 Neuronal activity, extracellular currents and potentials,** the V_e is created in the volume conductor by the transmembrane currents. In an ideal recording system the V_{rec} will be equal to $V_e - V_{ref}$, and it will be the potential difference that would exist if the tip had no net current flowing into it (Robinson, 1968). However, the recorded voltage V_{rec} relies on a recording system. Currently, for recording extracellular activity, researchers use a system composed of electrodes (i.e., microelectrode(s) and reference), amplifiers, filters, and digitizers, and finally software to visualize, save and analyze data. Here we will focus on the acquisition of extracellular action potentials measurements.

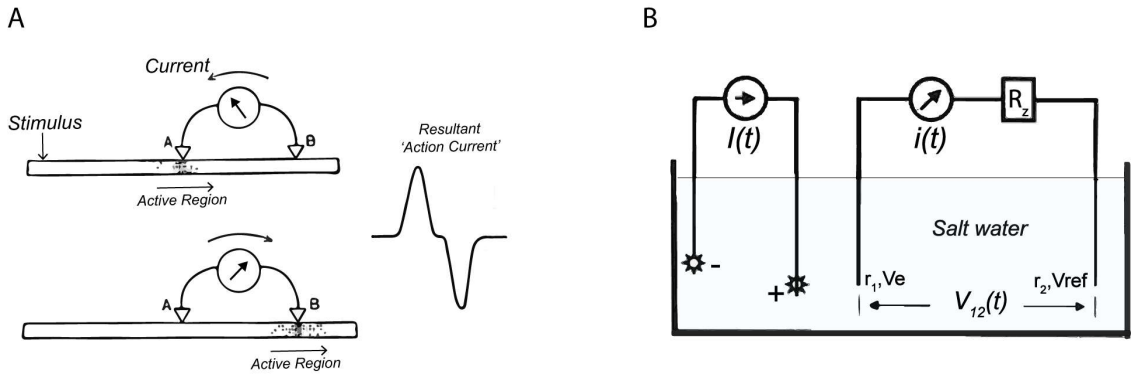

Figure 2.4 Circuits to measure potential differences caused by flow of ions. (a) A simple circuit to detect potential changes in nerves using a galvanometer. Adapted from Adrian, 1928; (b) A current source I(t) generates a potential field in a salt water tank. The circuit to record reliably the potential difference between V_e at location r_1 in the tank with respect to a 'reference' electrode V_{ref} at location r_2, needs to meet two conditions: first, the resistance (R_z) is much larger than the impedance of the salt water plus electrode-salt water interface plus the galvanometer resistance, so that the small measured current i(t) is simply related with $V_{12}(t)$, and second, the current i(t) must be large enough to meet the sensitivity requirement of the current instrument, but small enough to avoid distorting the potential field (Nunez & Srinivasan, 2009).

The first recording of action potentials, also called 'action currents', was performed in nerves using galvanometers (see Figure 2.4a). This very simple measurement system can be created by connecting an electrode in series with a galvanometer to a reference electrode. This defines a simple circuit, where the potential difference between the electrode and the reference drives a current in the galvanometer. However, the current flowing in this circuit can distort the potentials that are being measured. The use of relatively high current movements can load the voltage under

test, giving incorrect readings. One simple solution to this problem is to connect a large resistor in series with the galvanometer as shown in Figure 2.4b. This defines a circuit, where the potential difference between the electrode and the reference is given by Ohms law ($V_e - V_{ref} = V_{12} = i(t)\ R_z$). Unfortunately, this recording system configuration does not offer sufficient sensitivity (potential differences are less than 1 mV) for recording the potential variation from a single neuron. Edgar Adrian in *The Basis of Sensation* wrote: 'A great deal of the difficulty in physiological research is due to the microscopic size of the living cell – the unit out of which the organism is built. ... all the changes which we wish to investigate are very small too, and the experiments, which would be simple enough theoretically, are continually checked by the technical difficulties of work on a minute scale.' He was one of the first to study the activity of the nervous system at a cellular level in the 1920s. How did he manage to accurately measure the potential changes resulting from the activity of a single neuron? Using a valve amplifier to magnify electric potential changes, he could record spikes in single nerve fibres (axons) (Adrian, 1928). Valve amplifiers were developed during the first World War for detecting wireless signals and were applied to physiological research as soon as the war was over (Nicolelis, 2011). It is important to note that the measurement of a 'clean' signal was possible with this recording system because the nerve was inside a metal box that shielded from electromagnetic disturbances (i.e., Faraday cage). Nowadays, to measure the faint signal arising from brain activity, recording systems are designed to amplify the potential difference between electrodes and to reject the common-mode potential (i.e., noise identical in the recording and reference electrodes typically caused by capacitive coupling of the body and electrode lead with power line fields (Nunez & Srinivasan, 2009)). Usually this is accomplished with differential amplifiers characterized by high input impedance and low noise (Ferree, Luu, Russell, & Tucker, 2001). In Figure 2.5, a simple recording system diagram shows all the modules of a typical recording system that contribute to the recorded voltages, including the differential amplifier.

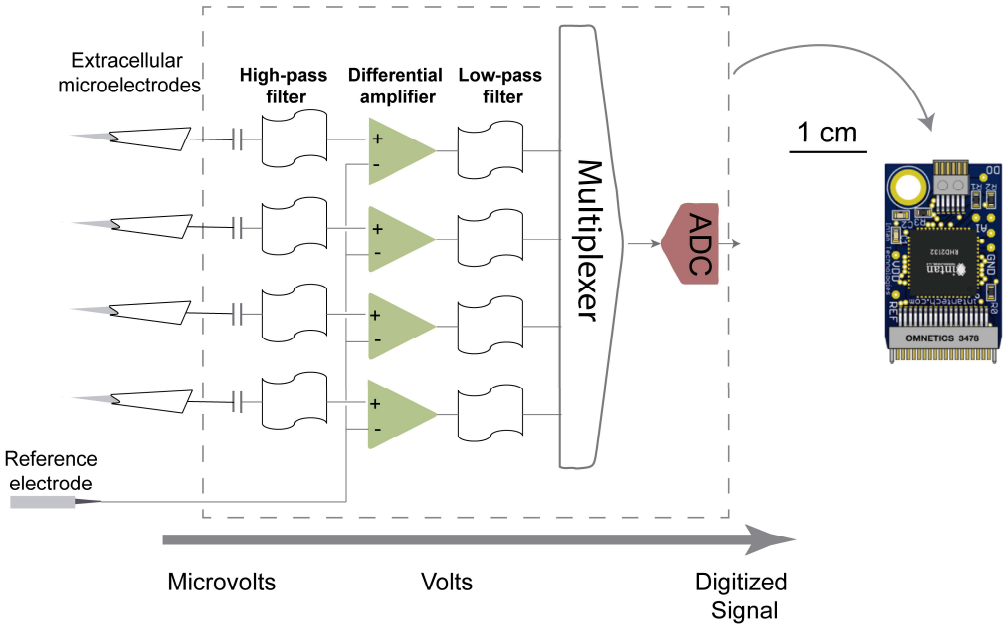

Figure 2.5 Diagram showing the modules of a typical recording system that contribute to the recorded voltages. Adapted from Intro to Intan Amplifier Chips | Intan Technologies, 2017. The signals from the electrodes are amplified and digitized with a sampling frequency in the range of 20–30 kHz. First, high-pass filters must be used to remove the large DC offsets present at the electrode-extracellular interface, along with any undesired low-frequency signals (e.g., movement artifacts). Second, high gain differential amplifiers are used to boost the signals to the larger voltage levels required by the ADC and to reject common-mode noise. Additionally, low-pass filters must be configured to less than half of the ADC frequency sampling rate to prevent aliasing, and may also be used to block undesired high-frequency signals and artefacts (Intro to Intan Amplifier Chips | Intan Technologies, 2017). An example of a headstage from Intan wich allows simultaneously recording from 32 microelectrodes. Adapted from Open Ephys, 2017.

2.5 Microelectrode-extracellular space interface and impedance measurement

The mechanism that underlies the transduction of neuronal activity into recorded voltages relies on the electrode-extracellular space interface.

Extracellular microelectrodes are usually made from metallic conductors. A thin insulated metal wire with an exposed tip is the most basic, and still widely used, device for *in vivo* extracellular recording from brains. Metals such as platinum, gold, tungsten, iridium, titanium nitride, stainless steel, iridium, iridium oxide, and alloys, nickel-chrome, platinum-iridium and platinum-tungsten have all been used in neural electrodes.

The measurement of electric potentials caused by the flow of ions in the extracellular space, where the conductivity is roughly six orders of magnitude lower than that in metals, is possible due to the transfer of ionic current, and the resulting potential, to the movement of electrons in

the metal electrode and lead connected to the external recording circuit. This transition from ion flow to electron flow is made through the double layer interface.

What is the double layer interface? When a metal is placed in a saline solution two phenomena occur: water dipoles close to the metal surface become oriented, and assuming the metal surface is negatively charged, the solution close to the metal surface become depleted of negative ions (anions), leaving behind a cloud of positive ions (cations). This cloud of cations screens the electric field caused by the excess of charge on the metal. Electroneutrality across the interface requires that the charge on the metal is always equal and opposite to the total charge on the solution side of the interface (Musa et al., 2012). The resulting charge distribution - two narrow regions of equal and opposite charge - is known as the electrical double layer (EDL).Figure 2.6a shows a model for the distribution of electric potential across a metal-solution interface, where the double layer region (represented in pink in the schematics) yields a capacitance, C_e which typically has a value around 20 μF cm^{-2} (Musa, 2011).

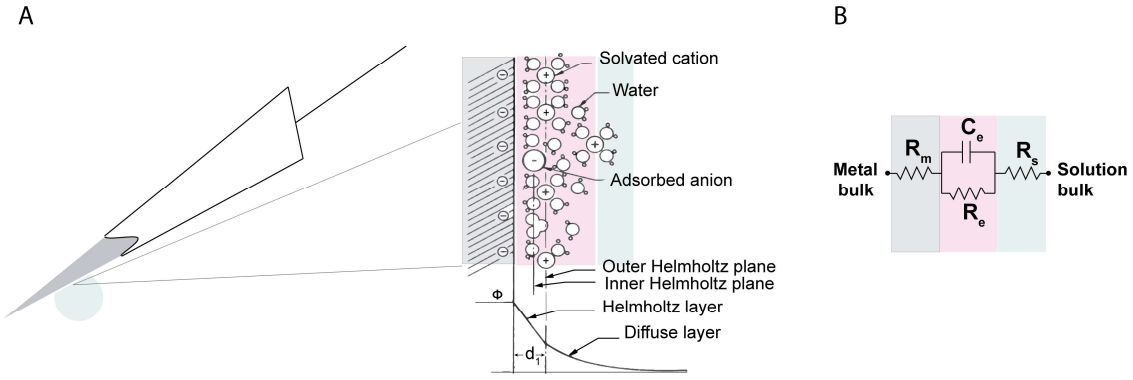

Figure 2.6 The electrical double layer at an electrode surface. Adapted from Wise, Angell, & Starr, 1970. (a) Electric potential (ϕ) profile across the double-layer region in the absence of specific adsorption of ions. The thickness of the Helmholtz layer, d_1 is of the order of an ionic radius (2 to 4 Å). The potential difference between the metal and the solution appears as DC offset in the measured signal and usually is removed by hardware high-pass filtering at 0.1 Hz. Thus, this potential difference known as the half-cell potential is established between the metal and the bulk of the solution; (b) Equivalent circuit model of the interface of a metal microelectrode recording in the brain. Adapted from Robinson, 1968.

The signal transduction takes place across the electrode-extracellular space when the charge distribution changes on the extracellular fluid side. In the previous section it was shown that ionic flow during the action potential gives rise to measurable time-varying electric potentials. The electric potential variation in the extracellular space is accompanied by a redistribution of the ion concentration close to the metal electrode and hence induce changes in the electrode's charges. In Figure 2.6b we introduce a simple model of the electrode-solution interface. The electrode-solution interface can be represented by a parallel R_eC_e combination in series with the resistances, R_m and R_s, due to the metal lanes and the solution, respectively. R_e is the charge transfer associated

with leakage resistance due to charge carriers crossing the electrical double layer. C_e is the capacitance of the electrical double layer at the interface of the exposed metal and the solution. This model is strictly limited to small potentials being relevant for the case of neural recording where extracellular signals are in the order of a few hundred microvolts.

The transition from ion flow in the solution to electron flow in the electrode could be of capacitive nature, involving the charging and discharging of the electrode-solution double layer (purely electrostatic), or faradaic, in which surface-confined species are oxidized and reduced (Bard & Faulkner, 2001; Merrill, Bikson, & Jefferys, 2005).

Electrodes at which faradaic processes occur are called charge transfer electrodes or 'non-polarized'. The well-known silver-silver chloride (Ag-AgCl) electrode approaches the ideal non-polarizable type. Moreover, non-polarizable electrodes have a small R_e allowing charge-transfer across the electrode-solution interface. If R_e is small, it bypasses the capacitor C_e thus providing a DC path for the measurement of steady potential levels. On the other hand, noble metals (e.g., stainless steel, gold and platinum) electrodes are so-called 'polarizable' electrodes and thus no charge transfer can occur across the metal-solution interface. Instead, electrode polarization is required to motivate current flow in the external recording circuit. The value of R_e of polarized electrodes is large, in the order of several megohms, and the effective equivalent circuit is dominated by the capacitor, C_e. Therefore, processes in polarizable electrodes are purely electrostatic in nature and caused by the charging and discharging of the double layer capacitance. Although charge does not cross the interface, external currents can flow (at least transiently) when the potential or solution composition changes (Cooper, 1971).

If one is interested in evaluating the individual circuit elements of the electrode-solution interface, it is possible to perform an electrochemical characterization. One can fully describe the processes governing the electrode's behaviour by applying an electrical perturbation to the system and measuring the response. The response of an electrode-solution interface can be modelled in terms of an equivalent circuit where the individual circuit elements describe the various phenomena occurring at the interface (Musa et al., 2012).

For example, consider a typical electrochemical experiment, as shown in Figure 2.7a, where an electrode under evaluation (working electrode) and a reference electrode are immersed in a solution, and the potential difference between them is varied by means of an external power supply.

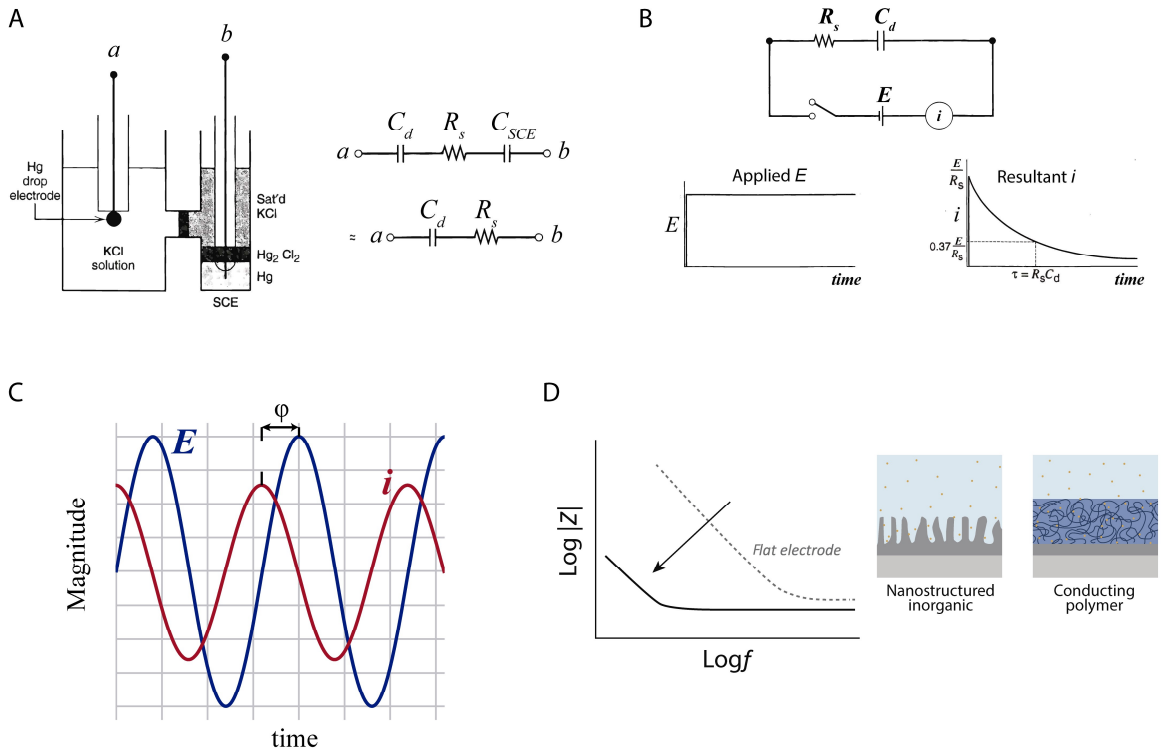

Figure 2.7 Electrochemical characterization of the electrode-solution interface. (a) Two-electrode cell with an ideal polarized mercury drop electrode and a SCE reference electrode. Representation of the cell in terms of linear circuit elements. Adapted from Bard & Faulkner, 2001; (b) Current transient resulting from a potential step applied to the working electrode with respect to the reference. The R. and Cd value can be computed from i-E curves. Adapted from Bard & Faulkner, 2001; (c) Graphical representation of the time dependent sinusoidal current response to a small ac voltage; (d) Increasing the electrode surface area or coating the electrode with conducting polymers enables an increase of C. value, and consequently a drop in impedance. The comparison of impedance is shown for a flat electrode (gray, dotted) and for an electrode with an enhancing coating (black line; for example, conductive polymers). Adapted from Rivnay, Wang, Fenno, Deisseroth, & Malliaras, 2017.

This system can be approximated by an electrical circuit with a resistor, R_s representing the solution resistance and a capacitor, C_d representing the double layer interface of an ideal polarized electrode. Usually, reference electrodes are made up of phases having constant composition (e.g., standard hydrogen electrode (SHE), saturated calomel electrode (SCE) and silver-silver chloride electrode (Ag-AgCl))(Bard & Faulkner, 2001). A reference electrode, such as SCE, approaches an ideal non-polarized where the passage of current does not affect its potential. Therefore, the contributions from the reference electrode are usually negligible. Herein, the variation in potential presented in Figure 2.7b, will produce a current to flow in the external circuit that depends on the circuit impedance and it reflects the response of the electrode, represented by the circuit elements R_s and C_d in series. The impedance is a measure of the ability of a circuit to resist the flow of charge across the electrode-solution interface phases (i.e., electronic conductor and an ionic conductor).

Usually, impedance is measured by applying a time-varying sinusoidal voltage signal, $E(\omega t) = E_0 \sin(\omega t)$, to the electrode under study (working electrode), where E_0 is the amplitude applied and

ω (rad s^{-1}) the angular frequency, and the current response is monitored, $i(\omega t) = i_0 \sin(\omega t+\varphi)$ with i_0 being the current amplitude and φ the phase shift (see Figure 2.7c). The impedance can be computed as $E(\omega t)/ i(\omega t)$ and represented as a vector defined in terms of magnitude $|Z|$ and phase shift φ. The measurement is made over a broad frequency range, typically from 1 Hz to 10 kHz, and the magnitude of the excitation is sufficiently small that a linear current-voltage response is obtained at each frequency (Cogan, 2008). In complex analysis, a projection of the vector on the x-axis is called the real part of the vector and a projection on the y-axis is called the imaginary part. This approach simplifies considerably the calculations and the impedance is generally represented using the complex notation $Z(j\omega)$, where j is the imaginary number and ω is the angular frequency (Musa, 2011). Equation 2.2 represents the impedance of the circuit for the interface of a metal microelectrode recording in the brain shown in Figure 2.6b.

$$\boldsymbol{Z\,(j\omega) = Z' + jZ'' = R + \frac{R_e}{1 + (\omega R_e C_e)^2} - j\frac{\omega R_e^2 C_e}{1 + (\omega R_e C_e)^2}}$$

Equation 2.2

Where R (equals to $R_s + R_m$) is the lumped series resistance, and Z' and Z'' are the real and imaginary part of the impedance, respectively. Z' and Z'' depend on the nature of the dominant conductive behaviour (i.e., resistor or capacitor) present within the system at a given frequency range. For example, for extracellular electrodes at 1 kHz (characteristic frequency of spikes, 1ms) the Equation 2.2 can be approximated as:

$$\boldsymbol{Z(j\omega) = R - j\frac{1}{\omega C_e}}$$

Equation 2.3

In practice, at this frequency, the electrode is primarily a capacitor in series with R, whose leakage resistance R_e, while not negligible, does not make an important contribution (Robinson, 1968). Hence, increasing C_e will decrease the impedance at this frequency (1 kHz). How can one increase the C_e value in microelectrodes (small area)? As shown in Figure 2.7d by increasing the surface area or by using materials complemented with pseudo-capacitance, such as conducting polymers, but also transition metal oxide films, such as IrO_x (Green, Lovell, Wallace, & Poole-Warren, 2008; Musa, 2011). Note that for microelectrodes, DC and low frequency potential oscillations in brain will encounter a very high electrode-extracellular impedance. Usually the

electrode impedance is 10-45 times higher at 10 Hz than at 1 kHz (Nelson, Pouget, Nilsen, Patten, & Schall, 2008).

2.6 Effects of the electrode impedance on data quality

For those interested in spike recording, the quality of the data depends on the amplitude of the extracellular spike relative to the background noise. Do high impedance electrodes reduce the amplitude of the signal?

Whenever electric current flows through a circuit with high impedance, there is an associated potential drop (Ohms law). So one might expect, a large voltage drop at the electrode-extracellular space interface where usually the impedance value is high, and consequently some attenuation of signal amplitude. But it is worth noting that, when high impedance electrodes are used in conjugation with a recording system that was designed to tolerate these high impedances, there shouldn't be a significant attenuation of the signal. Why?

In order to have a visual representation of the voltage drop and current pathways that occur during a recording, the equivalent circuit shown in Figure 2.8 given by Ferree et al. is used to represent all the physical elements of the electrodes and the input circuit prior to the first amplifier (Ferree et al., 2001). Only the first amplifier input impedance is critical for the measurement, as this is the only amplifier that interacts with the electrode (Nelson et al., 2008). In Figure 2.8a, the potentials V_e and V_{ref} are the potentials impressed at the microelectrode and reference, respectively. Ferree et al. wanted to quantify how the potential difference measured by the amplifier ($V_{e'} - V_{ref'}$) differs from the difference we are trying to measure ($V_e - V_{ref}$). He found a relationship between $V_{e'} - V_{ref'}$ and $V_e - V_{ref}$ as a function of electrode impedance and amplifier input impedance (Equation 2.4). In an ideal recording system, the $V_{e'} - V_{ref'}$ will be equal to $V_e - V_{ref}$. However, due to currents that flow to ground through the series combination of the effective electrode impedance and the effective amplifier input impedance, these potentials may differ.

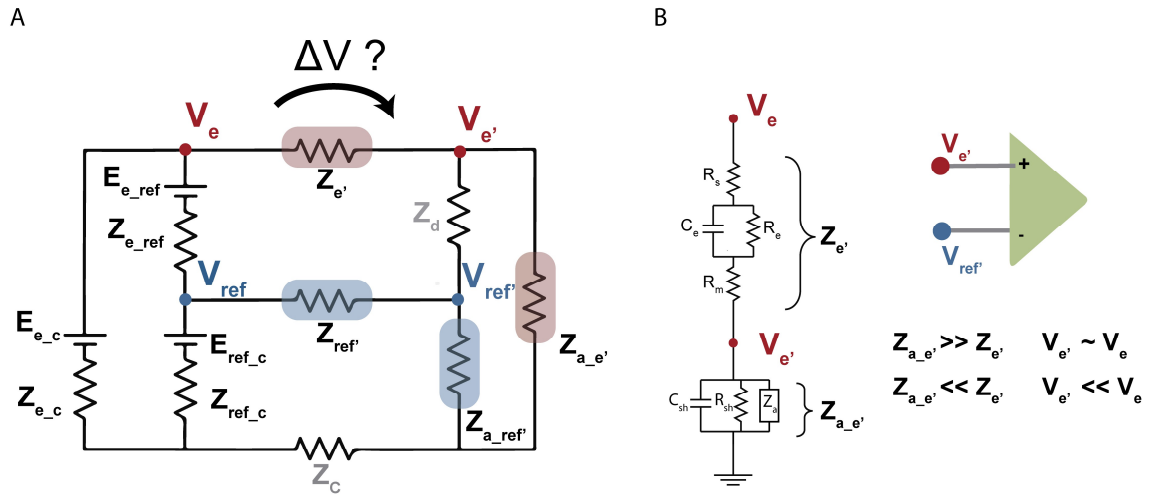

Figure 2.8 Circuit diagram used by Ferree et al. for understanding the relationship between electrode impedance and amplifier input impedance. (a) $Z_{e'}$ and $Z_{ref'}$ represent the effective electrode impedance for recording and reference electrodes, respectively, and Z_c represents the electrode impedance for an 'isolated common' electrode. In this configuration, the potential of both electrode and reference are measured relative to this common electrode. $Z_{a\_e'}$ and $Z_{a\_ref'}$ represent the effective amplifier input impedance for the electrode and the effective amplifier input impedance for the reference, respectively. Z_d represents the amplifier differential input impedance (Z_d is usually neglected because $Z_d >> Z_{a\_e'}$ and $Z_{a\_ref'}$). E_{e_ref}, E_{e_c} and E_{ref_c} represent bioelectric sources located between the designated electrodes. In reality, brain sources are not DC but are oscillatory and broad-banded. However, since the physics of volume conduction in biological tissue is quasi-static at each time point these AC sources may be considered as effective DC sources. Z_{e_ref}, Z_{e_c} and Z_{ref_c} represent the bulk impedance of the tissue between the designated electrodes (Z_{e_ref}, Z_{e_c} and $Z_{ref\_c} << Z_{e'}$) (Ferree et al., 2001); (b) Voltage divider. The effective electrode impedance $Z_{e'}$ is connected in series with input amplifier impedance $Z_{a\_e'}$ which includes the actual input amplifier impedance and the shunting paths to ground outside the amplifier. The shunting routes to ground outside the amplifier are R_{sh} and C_{sh} (Baranauskas et al., 2011; Lempka & McIntyre, 2013; Nelson et al., 2008).

$$V_{e'}(t) - V_{ref'}(t) = \left(1 - \frac{Z_{e'} + Z_{ref'}}{Z_{a\_e'} + Z_{a\_ref'}}\right)\left[V_e(t) - V_{ref}(t)\right]$$

Equation 2.4

As shown in Figure 2.8b, the effective electrode impedance, $Z_{e'}$ is the sum of impedances due to the resistance of the solution, the resistance of the electrode metal and the resistance and capacitance of the double layer at the electrode-solution interface. The effective amplifier input impedance, $Z_{a\_e'}$ is the total impedance to the ground seen from the electrode, and it includes a path through the amplifier and shunting routes (shunt resistance and capacitance) to ground outside the amplifier. The amplifier input impedance, Z_a represents its tendency to oppose the flow of current from the electrodes through the amplifier to ground. By designing amplifiers which have high input impedances, the current flow becomes low (Ferree et al., 2001). In general, the current in the measuring circuit should be smaller than the current flow in the brain to ensure that it is not distorted by the measuring circuit (Nunez & Srinivasan, 2009).

Equation 2.4 reflects the attenuation of the signal as a function of the effective electrode impedance and amplifier input impedance. It can provide numerical estimates of signal loss for various electrode and amplifier systems. A simplified circuit is represented in Figure 2.8b and the appearance of a voltage divider is undeniable. If $Z_{a\_e'}$ is not substantially larger than $Z_{e'}$, $V_{e'}$ will be less than V_e. Some differential amplifier systems, like the ones from Intan Technologies, have input impedances (Z_a) close to 13 MΩ at 1kHz. Assuming electrode impedances of 1 MΩ and 100 kΩ and that $Z_{e'} >> Z_{ref'}$ and $Z_{a\_e'} >> Z_{a\_ref'}$, the signal loss is around 7 % and 1 %, respectively, which may be negligible for most purposes.

Even if the Z_a is large, the shunting capacitance is another component that can reduce the effective amplifier input impedance, especially at higher frequencies (Nelson et al., 2008; Obien, Deligkaris, Bullmann, Bakkum, & Frey, 2015; Robinson, 1968). This shunt capacitance arises mainly from the capacitance across the thin insulation isolating an electrode shaft and the surrounding electrolyte, as well as the cumulative capacitance along cables and connectors (Robinson, 1968). This route to ground, parallel to the amplifier, reduces the effective amplifier impedance, and being capacitive, this effect increases with signal frequency (Nelson et al., 2008). Therefore, the shunt capacitance should be small to create a large shunt impedance, especially when the electrodes have a large impedance, which are thus more susceptible to attenuation by shunt capacitance at high frequencies (Obien et al., 2015; Robinson, 1968).

If the proper recording equipment is used, the voltage that is ultimately amplified and recorded should not be appreciably affected by the electrode impedance. This does require some attention from neurophysiologists. The input impedance amplifier must be much larger than the impedance of the electrode-solution interface for the potential difference at the amplifier inputs reflect the actual potential difference between V_e and V_{ref}.

2.7 Effects of electrode size on data quality

A separate question from whether the impedance of an electrode influences the recorded voltage is the question of whether the size of the recording electrode has an impact on the recorded voltages. Indeed, an electrode impedance is of course highly dependent on the size of its uninsulated surface area. Historically, impedance, which is more easily measured, was often used as a proxy to describe the surface area of an electrode (Camuñas-Mesa & Quiroga, 2013; Lempka et al., 2006, 2011; Moffitt & McIntyre, 2005; Scholvin et al., 2016). Extracellular microelectrode sizes range from 5 to 50 μm diameter (Musa, 2011).

An electrode detects the average voltage present at the uninsulated metal surface (Nunez & Srinivasan, 2009; Robinson, 1968). In Equation 2.1, a point-source equation was given for the potential in the extracellular medium. The recorded voltage from electrodes larger than an ideal point electrode is an average of multiple locations from the surface area of the microelectrode. The larger the electrode area, the larger the averaging effect, and spike amplitudes may be reduced due to the averaging with nearby regions with smaller signals (Obien et al., 2015). Nonetheless, larger electrodes have a higher probability of being physically near an active neuron, and therefore picking up spikes (Camuñas-Mesa & Quiroga, 2013). Moreover, larger electrodes generally have lower impedance, reducing thermal noise and the probability of attenuation due to large $Z_{e'}/Z_{a\_e'}$ ratios (larger area, lower $Z_{e'}$) (Obien et al., 2015).

Nevertheless, with large and high-density arrays of small electrodes, there is no need to enlarge the electrode to be close to the location with the largest neural signal, as there will always be another electrode "at the right spot". Moreover, the averaging of the extracellular potentials is diminished with small electrodes. As a result, small electrodes closely-packed are much preferable for recording extracellular potentials, with only the electrode noise as a limiting factor. How small can one produce recording electrodes? Decreasing electrode size is associated with increasing impedance, which increases thermal noise. Thermal noise also so-called Johnson-Nyquist is the electronic noise generated by the thermal agitation of the charge carriers (usually electrons) inside an electrical conductor at equilibrium, which happens regardless of any applied voltage, and is inversely proportional to the electrode size. In the case of a microelectrode in equilibrium, we are looking at the uncertainty of the voltage at the double layer interface. It can easily be shown that the fluctuation of the voltage on a capacitor is inversely proportional to the capacitance. This implies that by scaling down the electrode, the uncertainty of the voltage appearing on the sensor increases (Hassibi, Navid, Dutton, & Lee, 2004). Thermal noise is commonly believed to be one of the main contributors to the background noise in extracellular recordings (Desai, Rolston, Guo, & Potter, 2010; Hassibi et al., 2004; Heuschkel, Fejtl, Raggenbass, Bertrand, & Renaud, 2002). The thermal noise is given by Equation 2.5.

$$\sigma_{RMS}^{th} = \sqrt{4\,k\,T \int_{f1}^{f2} Z_{real}\,df}$$

Equation 2.5

Where k is Boltzmann's constant, T is the temperature in degrees Kelvin, f_1 and f_2 are the lower

and upper limits of the recording bandwidth in Hz, and Z_{real} is the real part of the impedance in the respective frequency bandwidth (f_1 to f_2).

2.8 Effects of electrode density on spike sorting algorithms

A single microelectrode can detect the activity of multiple neurons in the vicinity (< 200 μm). The only way to identify a given neuron is either to move the electrode closer to its soma than to any other neuron, or to use a spike sorting algorithm that assumes that different neurons will exhibit action potentials with unique amplitudes and waveform shapes.

The first step in the analysis is the identification of spikes (Hazan, Zugaro, & Buzsáki, 2006). The amplitude of the action potential decreases with the distance from the neuron to the recording electrode, and for neurons located closer than 50-100 μm from the electrode, the spikes are often large enough to be detected over background activity and it may then be possible to separate them according to their shapes. For neurons further away, up to 150 – 200 μm from the electrode, spikes can be detected, but the difference in their shapes is masked by the noise and they are grouped together as 'multiunit activity' (Harris et al., 2016). After the detection, assigning these extracellular events to clusters belonging to distinct neurons is one of the biggest challenges for analysis. The problem starts when cell bodies are closely packed together and/or the action potential from a single neuron varies in amplitude (e.g., within a burst or due to electrode 'drift').

The use of two (McNaughton et al., 1983) or four spaced wires (tetrodes) (Gray et al., 1995; Harris, Henze, Csicsvari, Hirase, & Buzsaki, 2000; Jog et al., 2002; Wilson & McNaughton, 1993) enables the separation of more neurons, since the amplitude of the recorded spike on each electrode is a function of the distance between the neuron and each electrode (i.e., tetrodes make possible unequivocal triangulation in a volume).

It has become clear recently that dense electrode configurations, in which the neuron is detected by multiple electrodes, generally improves sorting (Buzsáki, 2004; Dimitriadis, Neto, & Kampff, 2016; Harris et al., 2016). Why? These devices densely sample the extracellular electric field of nearby neurons, and thus provide a detailed description of the spatiotemporal profile of a neuron's extracellular action potential. It is expected that this additional detail will significantly aid automated analysis methods for the detection and isolation, and possibly type identification, of individual neurons in the vicinity of the probe. Yet, methods capable of utilizing such a dense sampling are just now being developed (Dimitriadis et al., 2016; Lewicki, 1998; Pachitariu,

Steinmetz, Kadir, Carandini, & Harris, 2016; Rey, Pedreira, & Quiroga, 2015; Rossant et al., 2016; Yger, Spampinato, & Esposito, 2016).

2.9 Large-scale recording of neuronal activity

From the very first recordings of a single axon by Lord Adrian in the 1920s, generations of neuroscientists until the 1980s were focused on identifying single neurons that could be driven to fire maximally in response to a stimulus and then average their response over several repetitions of the same stimulus or behaviour (Quiroga & Panzeri, 2009). Understanding what makes a neuron fire, or not fire, was a central question in neuroscience. Single microwires were the first tool and have been widely used to study the brain for nearly 60 years (Figure 2.9a, left panel). With the advent of multi-electrode recordings, the focus shifted from the single neuron to the study of neuronal populations. Nonetheless, 'listening' simultaneously to the electric signals produced by many individual neurons, distributed across multiple brain areas, in a behaving animal, represents a tremendous experimental challenge.

Neuroscientists started using microwire bundles and arrays that consist of a large number of single-contact electrodes that are further apart (more than 100 μm) where the number of neurons recorded increases linearly with site count (Harris et al., 2016). The microwires evolved into tetrodes (i.e., four microwires closely spaced together). They have been one of the most commonly used tool in electrophysiology due to their low cost and stability *in vivo*. Over the years, technological progress has contributed to a move from microwires to microfabricated silicon probes. Silicon-based probes have been developed with semiconductor processes and have been used for several decades (Najafi et al., 1985) The batch processes of semiconductor manufacturing enabled the fabrication of dozens of electrodes on a single shaft (Berényi et al., 2014; Blanche, 2005; Buzsáki et al., 2015; Du, Blanche, Harrison, Lester, & Masmanidis, 2011; Shobe, Claar, Parhami, Bakhurin, & Masmanidis, 2015b). The probe illustrated in the right panel of Figure 2.9a is an example of a commercially available silicon probe with 32 electrodes, spanning an area of around 10,000 μm^2. However, the widespread adoption of silicon probes by the neuroscience community has generally been slow. As shown in Figure 2.9b, and in more detail in Appendix A, Table A.1 the increase in the number of neurons was possible mostly due to the increase on the number of single-contact electrodes (e.g., microwire bundles, microwire arrays and Utah arrays, as shown in Figure 2.9c).

Extracellular recording is an invasive technique and this approach is not viable in rodents, whose

tiny brains are roughly a centimetre deep, if one wants to record hundreds to thousands neurons in different brain areas. Therefore, the desire for large-scale monitoring of neuronal activity and the need to minimize tissue damage, inflicted by electrode insertion, compete with each other (Buzsáki et al., 2015).

Researchers, companies, and funding agencies across the globe have recognized that further understanding of brain function, will possibly require simultaneously monitoring the activity of large numbers of individual neurons with sub-millisecond precision in multiple brain areas (Buzsáki, 2004; Chapin, 2004), and recent developments towards this goal have occurred. First, affordable recording systems compatible with a few hundred electrodes with direct streaming of the data to a standard computer are currently available (http://www.intantech.com and http://www.open-ephys.org/). Secondly, open-source software is available to enable data analysis of large datasets (Jun et al., 2017; Pachitariu et al., 2016; Rossant et al., 2016; Yger et al., 2016). Moreover, the potential to generate breakthroughs in brain research has prompted investment in new tools (e.g., Neuropixels and NeuroSeeker projects). This surge in investment has resulted in probes with 1,356 electrodes in a single 8 mm shank, which can span several structures in the brain. By employing CMOS technology, these probes have been designed to overcome the geometric restrictions on the number and density of electrodes. They employ a 'scanning' concept that is common in camera image sensors, which enables the highest density and number of parallel readout electrodes in a silicon probe ever achieved in the history of neuroscience for *in vivo* recordings. This tool brings not just a change in the amount of data, but also new challenges for the analysis, and possibly new theoretical frameworks (Dyson, 2012; Focus on the neuroscience toolbox, 2016).

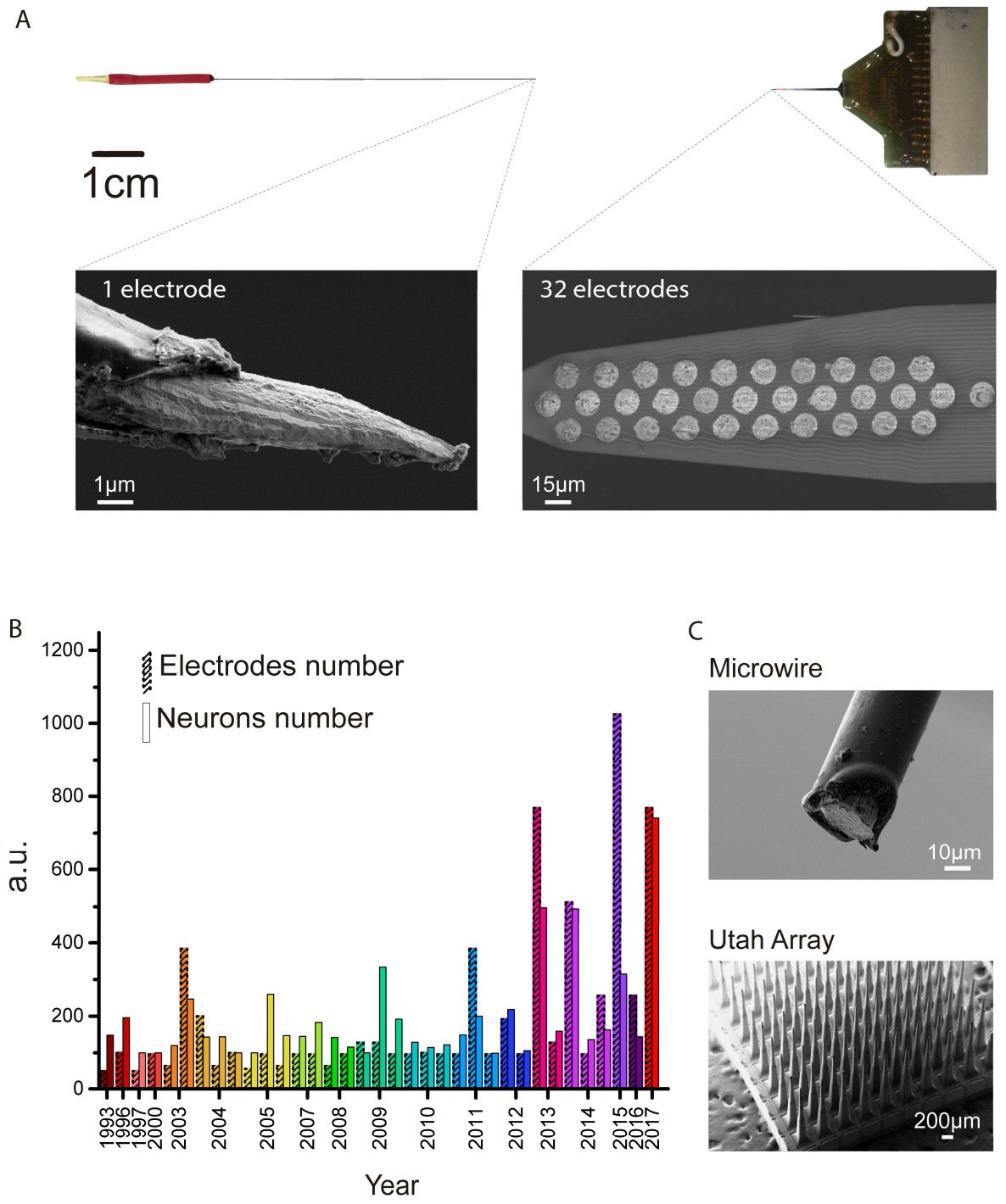

Figure 2.9 Extracellular neural probes are fabricated with increasing number of electrodes to capture the activity of increasing number of neurons. (a) Pictures from a tungsten microelectrode (left) and a commercially available silicon-based probe with high-density microelectrode array (right). Inserts show SEM images of the metal microelectrodes; (b) The number of electrodes and neurons simultaneously recorded found in the literature. Literature review based on Stevenson, 2017 and Stevenson & Kording, 2011. (c) SEM images from a microwire, usually used to build tetrodes, microwire bundles, or microwire arrays, and a Utah array with multiple single contacts.

Chapter 3. Does impedance matter (for recording spikes with polytrodes)?

Summary

Extracellular microelectrodes have been widely used to measure brain activity, yet there are still basic questions about the requirements for a good extracellular microelectrode. One common confusion is how an electrode impedance affects the amplitude of measured extracellular spikes and background noise.

Here we discuss how a commercial electrode impedance affects data quality in extracellular recordings, which is crucial for the detection of spikes and their subsequent assignment to the correct neurons. This study employs commercial polytrodes containing 32 electrodes (177 μm^2) arranged in a dense array. This allow us to directly compare, side-by-side, the same extracellular signals measured by modified low impedance (~ 100 kΩ) microelectrodes with unmodified high impedance (~ 1 MΩ) microelectrodes. We first evaluate existing protocols to lower the impedance of the electrodes. The poly(3,4-ethylenedioxythiophene)-polystyrene sulfonate (PEDOT-PSS) electrodeposition protocol is a simple, stable, and reliable method for decreasing the impedance of a microelectrode up to tenfold. We next record *in vivo* using polytrodes that are modified in a 'chess board' pattern such that the signal of one neuron is detected by both coated and non-coated electrodes. The performance of the coated and non-coated electrodes is then compared using metrics of the background noise and peak-to-peak amplitude of the detected action potentials.

If the proper recording system is used, then the impedance of a microelectrode, within the range typical of standard polytrodes (~ 0.1 to 2 MΩ), does not significantly affect data quality and spike sorting. This study provides a good reason for neuroscientists to stop worrying about one more unknown.

This chapter has been prepared for submission and is currently stored as the following preprint: Neto, J. P., Baião, P., Lopes, G., Frazão, J., Nogueira, J., Fortunato, E., ... Kampff, A. R. (2018). Does impedance matter when recording spikes with polytrodes? *bioRxiv*, 270058.

3.1 Introduction

Throughout the electrophysiology literature, an electrode impedance magnitude at 1 kHz is regularly used as a proxy for its ability to detect the activity of individual neurons (Alivisatos et al., 2013; Kotov et al., 2009; Nam, 2012). Are high impedance electrodes necessary to isolate extracellular spikes? Won't high impedance electrodes reduce the amplitude of the signal and/or increase the background noise? Clearly, lowering the signal-to-noise ratio (SNR) will make spike sorting more difficult. How exactly does electrode impedance affect SNR?

Several studies have shown an impact of an electrode impedance on data quality (Ansaldo, Castagnola, Maggiolini, Fadiga, & Ricci, 2011; Baranauskas et al., 2011; Chung et al., 2015; Du, Blanche, Harrison, Lester, & Masmanidis, 2011; Ferguson, Boldt, & Redish, 2009; Keefer, Botterman, Romero, Rossi, & Gross, 2008; Kozai et al., 2015; Ludwig et al., 2011; Ludwig, Uram, Yang, Martin, & Kipke, 2006; Scott, Du, Lester, & Masmanidis, 2012; Zhao, Gong, Zheng, & Wang, 2016). However, there is also literature showing that electrode impedance does not affect the extracellular spikes recorded (Cui et al., 2001; Desai et al., 2010; Suner, Fellows, Vargas-Irwin, Nakata, & Donoghue, 2005). Commercially available silicon probes, also called polytrodes, have relatively high impedance electrodes (~ 0.5-2 MΩ), due to their low surface area and small diameters (< 50 μm), which are suitable for recording single unit activity. Materials such as Au, Pt, and Ir are often used as the electrode material in polytrodes. Lowering the electrode impedance prior to recording is a 'standard' step in various laboratories (Desai et al., 2010). How does one lower the impedance of commercial polytrodes?

Electrodeposition is a simple and reproducible technique, and yet has great flexibility to create a variety of coatings (Ferguson et al., 2009). For more details about electrodeposition techniques, see Santos et al., 2015. By electroplating Au or Pt, the surface roughness increases and the electrode impedance decreases (Cui & Martin, 2003; Desai et al., 2010; Ferguson et al., 2009; Márton, Bakos, Fekete, Ulbert, & Pongrácz, 2014). Over the last decade, conductive polymers, particularly poly(3,4-ethylenedioxythiophene) (PEDOT), have been electrodeposited onto electrodes due to their chemical stability and mechanical integrity when implanted in brain tissue (Kozai et al., 2016; Ludwig et al., 2011; Ludwig et al., 2006). Moreover, when compared to metals, these polymers are typically softer materials offering a more intimate contact between the electrode surface and brain tissue (Green et al., 2008). Prior to the electrodeposition, a dopant is added to the synthesis solution to improve conductivity; the most common dopant molecule is polystyrene sulfonate (PSS) (Aregueta-Robles, Woolley, Poole-Warren, Lovell, & Green,

2014).

Our goal was simply to answer the question: 'should I reduce the impedance of my electrodes and why'? Despite the prevalence of this question in the field, a definitive answer is still lacking. It is important to understand the impact of a particular electrode impedance and electrodeposition technique to determine if the effort to reduce individual electrode impedances is worthwhile.

3.2 Methods

Polytrodes

All experiments were performed with a commercially available 32-channel probe (A1x32-Poly3-5mm-25s-177-CM32, NeuroNexus), with 177 μm^2 area electrodes (iridium) and an inter-site pitch of 22-25 μm. Following each surgery, cleaning was performed by immersing the probe in a trypsin solution (Trypsin-EDTA (0.25 %), phenol red, TermoFisher Scientific) for 30-120 minutes and rinsing with distilled water (Neto et al., 2016).

Coatings

NanoZ hardware and software (Neuralynx) was used to perform gold and PEDOT-PSS coating depositions. Moreover, both coatings were galvanostatically deposited in a two electrode cell configuration consisting of the probe electrodes individually selected as the working electrode and a platinum wire as the reference electrode. The reference wire was placed around the deposition cup while the probe was maintained at a fixed and equal distance to all points of the reference wire. By selecting the 'Manual Control' from the software it is possible to select individual probe electrodes (Baião, 2014).

For the gold coatings a commercial non-cyanide gold solution was obtained from Neuralynx. The deposition solution for PEDOT-PSS consisted of 0.01 M of EDOT (Sigma-Aldrich, 97 %, M_w = 142.18) and 0.1 M of PSS (Sigma-Aldrich, M_w = 1000000) dissolved in deionized water. The optimal deposition parameters were -30 nA during 120 seconds and +30 nA during 5 seconds, respectively for gold and PEDOT-PSS (Baião, 2014). Before and after the deposition, electrodes impedance magnitude at 1 kHz, in sterile phosphate buffer saline solution (PBS, 1 mM, pH 7.4),

was measured with NanoZ. Post-deposition assessment of coating morphology was performed by scanning electron microscopy (SEM-FIB, Zeiss Auriga).

Electrochemical characterization

The electrochemical behavior of the microelectrodes was studied in PBS (1 mM, pH 7.4) by electrochemical impedance spectroscopy (EIS). For the electrochemical characterization, a potentiostat (Reference 600, Gamry Instruments) was used with a three electrode cell configuration where the probe electrodes were connected individually as the working electrode, a platinum wire served as the counter electrode, and an Ag-AgCl (3 M KCl, Gamry Instruments) as the reference electrode. The impedance was measured for frequencies from 1 Hz to 100 kHz by applying a sinusoidal signal with an amplitude of 10 mV.

In vivo recordings

Before and after each surgery, the impedance magnitude of each electrode was measured using a protocol implemented by the RHD2000 series chip (InTan Technologies) with the probe electrodes placed in a dish with sterile PBS (1 mM, pH 7.4) and a reference electrode, Ag-AgCl wire (Science Products GmbH, E-255).

For the surgeries under ketamine, Long Evans rats (400 to 700 g, both sexes) were anesthetized with a mixture of ketamine (60 mg/kg) and medetomidine (0.5 mg/kg) and placed in a stereotaxic frame. At the initial stage of each ketamine surgery, atropine was given to suppress mucus secretion (0.1 mg/kg, atropine methyl nitrate, Sigma-Aldrich). For the surgeries under urethane, rats (400 to 700 g, both sexes) of the Lister Hooded strain were anesthetized with urethane (1.6 g/kg) and placed in a stereotaxic frame. At the initial stage of each urethane surgery, the animal was injected with atropine (0.05 mg/kg), temgesic (20 µg/kg) and rimadyl (5 mg/kg). Ketamine, medetomidine and urethane were administered by intraperitoneal (IP) injection, while temgesic and rimadyl were administered by subcutaneous (SC) injection. Atropine was administered by intramuscular (IM) injection

Anesthetized rodents then underwent a surgical procedure to remove the skin and expose the skull above the targeted brain region. Small craniotomies (2 mm medial-lateral and 2 mm anterior-posterior) were performed above the target area. The reference electrode Ag-AgCl wire (Science Products GmbH, E-255) was inserted at the posterior part of the skin incision.

Equipment for monitoring body temperature as well as a live video system for performing probe insertion was integrated into the setup. For the extracellular recordings we used the Open Ephys (http://www.open-ephys.org) acquisition board along with the RHD2000 series interface chip that amplifies and digitally multiplexes the signal from the 32 extracellular electrodes (Intan Technologies). Extracellular signals in a frequency band of 0.1-7,500 Hz were sampled at 20 or 30 kHz with 16-bit resolution and were saved in a raw binary format for subsequent offline analysis using Bonsai interface (Bonsai, 2017; Lopes et al., 2015).

Animal experiments under urethane were approved by the local ethical review committee and conducted in accordance with Home Office personal and project (I67952617; 70/8116) licenses under the UK Animals (Scientific Procedures) 1986 Act. Animal experiments under ketamine were approved by the Champalimaud Foundation Bioethics Committee and the Portuguese National Authority for Animal Health, Direcção-Geral de Alimentação e Veterinária.

Analysis

For the analyses described in the following, a third order Butterworth filter with a band-pass of 250-9,500 or14,250 Hz (95 % of the Nyquist frequency) was used in the forward-backward mode. The magnitude of background noise can be estimated from the median absolute signal, assuming a normal noise distribution, σ_{Median} = median(|signal(t)|/0.6745) to avoid contamination by spike waveforms (Quiroga, Nadasdy, & Ben-Shaul, 2004) or simply the noise can be defined as the standard deviation (root-mean-square noise, σ_{RMS}) of the signal (Scott et al., 2012). Some results were represented as mean ± standard deviation.

We ran Kilosort on all the datasets with a maximum number of templates set to 128 (four times the number of electrodes on our probe). This algorithm iteratively generates templates and then uses these templates to detect and classify the individual spikes. Each spike is assigned to the template that matches it the best. Afterwards, we used Phy to check the automatically generated units/clusters. Phy is a graphical user interface for refining the results of spike sorting. After the manual sorting we used functions to assess cluster quality (https://github.com/cortex-lab/sortingQuality). The "well isolated" units considered for the analysis have simultaneously low ISI violations and contamination rates, and high isolation distances values. Units with more than 50 spikes were considered for posterior analyses. Additionally, the average peak-to-peak (P2P) amplitude of all spikes from each unit on a given recording site was computed.

3.3 Results

Electrode coating

Figure 3.1a-c show the morphological differences between a pristine iridium electrode, PEDOT-PSS coated and gold coated electrode (Figure 3.1a, b and c, respectively). Pristine electrodes typically display a smooth surface with almost no irregularities (some might occur due to microfabrication process). Gold coating yields a rough structure on the electrodes which leads to an increase in surface area, one of the key aspects in lowering the impedance modulus at 1 kHz. PEDOT-PSS coated electrodes have a 'fuzzy' coating. For gold coated electrodes (Figure 3.1c and d), we observe that even though the mean impedance after coating is relatively low when compared to the pristine counter-part, these values tend to increase following brain insertion. This reflects the poor adhesion of the gold coatings to iridium electrodes (Figure 3.1d). The gold instability and delamination was also observed in some previous studies (Scott et al., 2012). In the case of PEDOT-PSS (Figure 3.1b and e), the impedance values tend to remain stable for a long period of time, allowing for repeated surgeries and penetrations. Therefore, taking into account the impedance value after PEDOT-PSS coating (values under 100 kΩ) and the stability and resilience over time, this coating was considered ideal for reducing the extracellular microelectrode impedance.

Figure 3.2a illustrates the microelectrode array design employed to assess the impact of impedance on data quality. Electrodes were coated in a 'chess board' pattern such that the signal of one neuron is detected by several coated and non-coated electrodes.

The mean impedance at 1 kHz for three polytrodes was 1.1 ± 0.4 MΩ and 0.084 ± 0.015 MΩ pre- and post-deposition, respectively. The deposition protocol is stable across probes and electrodes ($n_{PEDOT} = 46$ and $n_{pristine} = 48$) (Figure 3.2b).

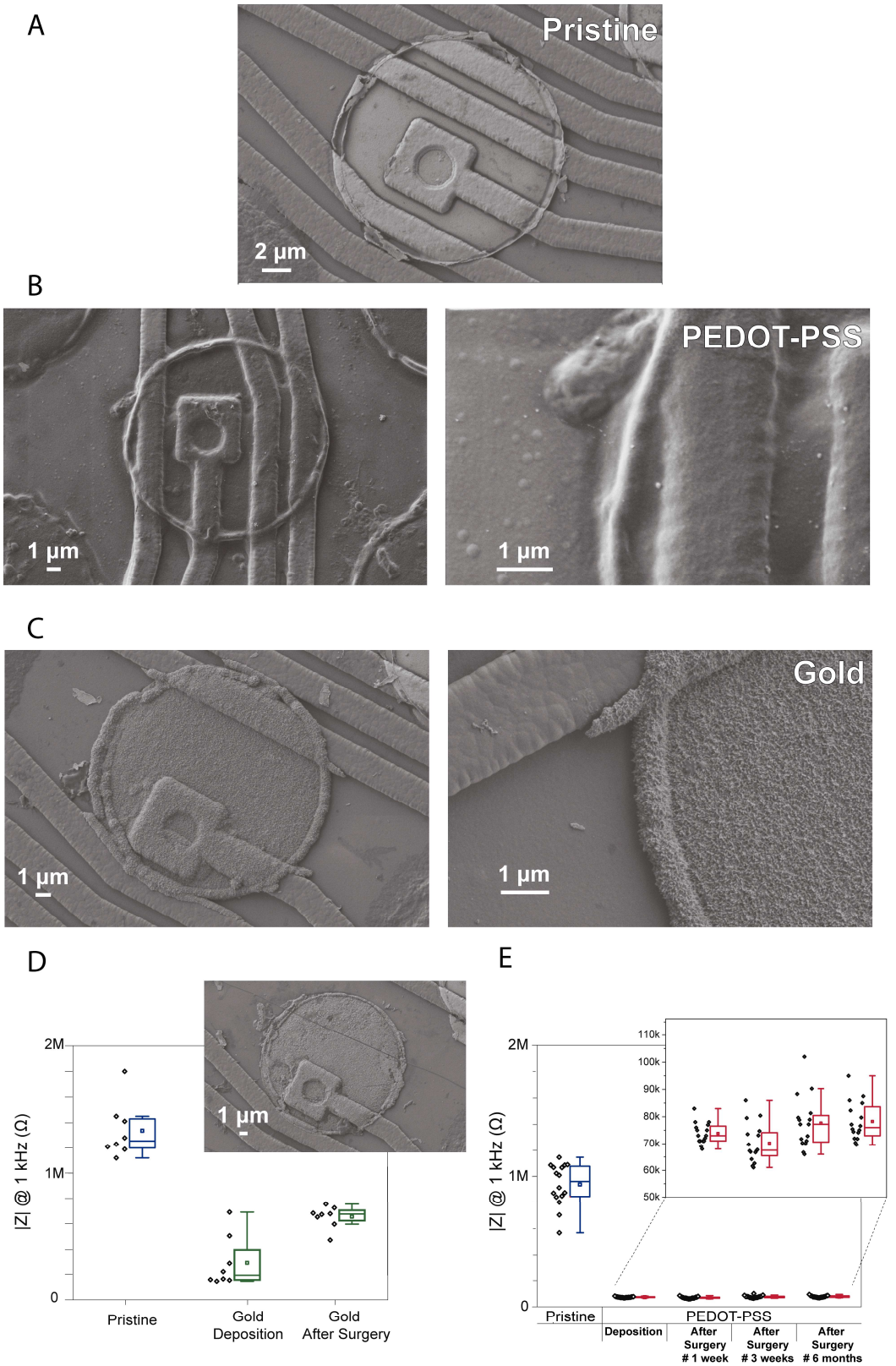

Figure 3.1 SEM images showing the surface morphology of electrodes from a commercial polytrode in their original state, and after the coatings. (a) Pristine electrode, (b) PEDOT-PSS coated electrode and (c) gold coated electrode; (d) Stability of gold coating for 8 electrodes from one polytrode (impedance variation of electrodes) after the deposition and after an acute surgery. SEM image insert of the gold coating from one electrode after the surgery; (e) Stability of PEDOT-PSS coating for 16 electrodes from one polytrode (impedance variation of electrodes) for a period of approximately 6 months with surgeries being performed during that period. In the boxplots, line: median, square: mean, box: 1st quartile–3rd quartile, and whiskers: 1.5 x interquartile range above and below the box.

Noise characterization: In saline

First, the performance of PEDOT coated electrodes was compared to pristine electrodes in terms of noise, both in saline solution and during *in vivo* recordings.

The contribution of all non-biological noise sources was measured by recording signals from single microelectrodes immersed in a saline solution. The non-biological sources include the electronic noise due to the amplifier, thermal noise and noise associated with the double layer interface (Baranauskas et al., 2011; Hassibi et al., 2004) At room temperature, the actual noise measured in saline solution for pristine and coated microelectrodes is shown in Figure 3.2c. The σ_{RMS} and σ_{Median} values are similar in saline solution. The noise in saline taking into consideration the σ_{Median} value, for the pristine electrodes was 5.6 ± 0.4 μV, and for the coated electrodes was 3.9 ± 0.4 μV, which represents a reduction of about 30 %. The thermal noise depends on the real part of the measured impedance as shown in Equation 2.5. The thermal noise computed in the 200-8,000 Hz frequency band for pristine (n = 3) and coated (n = 3) microelectrodes was 5.0 μV and 2.8 μV, respectively (Figure 3.2d). Additionally, the electronic noise due to the amplifier in our system, measured by shorting the headstage inputs, was 2.0 ± 0.1 μV. We can predict the non-biological noise value as the square root of the sum of the squared thermal noise (~ 5.0 μV and 2.8 μV for pristine and coated microelectrodes, respectively) and squared electronic noise (~ 2.0 μV). We found similar values for the total noise measured in saline (5.6 μV in non-coated and 3.9 μV in coated) and the predicted ones (5.4 μV in non-coated and 3.4 μV in coated).

Noise characterization: *In vivo*

We next recorded *in vivo* using polytrodes with the 'chess board' pattern described in Figure 3.2a. These recordings were conducted in different brain regions and at different depths. Also, ketamine or urethane anaesthesia was used to compare signal and noise levels recorded during different brain states (Figure 3.2e and f). Under ketamine, the cortex switches between periods of high neuronal activity and periods of much lower activity (up and down states)(Ruiz-Mejias, Ciria-Suarez, Mattia, & Sanchez-Vives, 2011). Under urethane anaesthesia, the activity is similar to natural sleep brain activity (Clement et al., 2008; Pagliardini, Gosgnach, & Dickson, 2013).

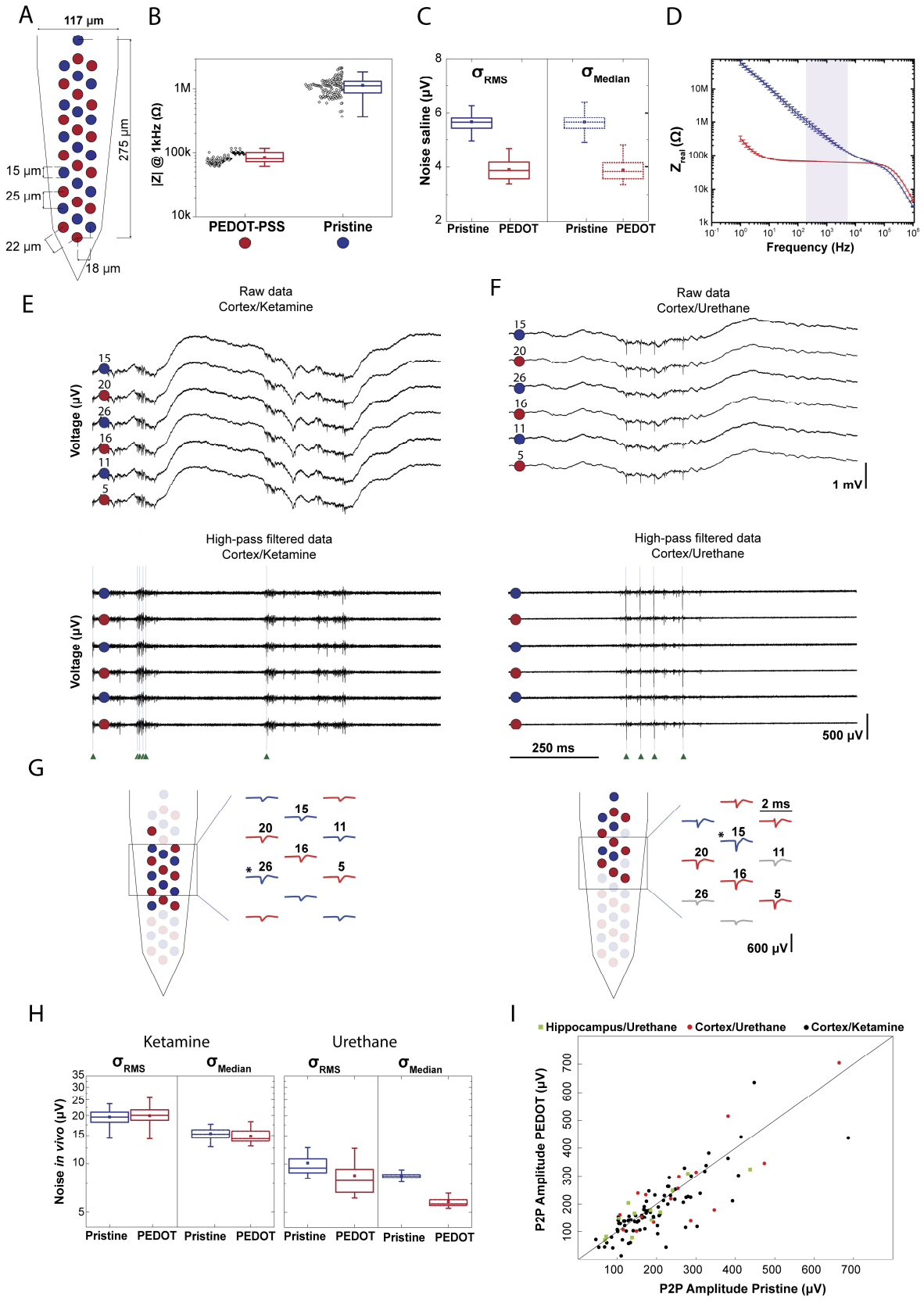
A
117 µm
275 µm
15 µm
25 µm
22 µm
18 µm
B
|Z| @ 1kHz (Ω)
1M
100k
10k
PEDOT-PSS
Pristine
C
σ RMS
σ Median
Noise saline (µV)
Pristine PEDOT
Pristine PEDOT
D
Z real (Ω)
Frequency (Hz)
E
Raw data
Cortex/Ketamine
Voltage (µV)
15
20
26
16
11
5
High-pass filtered data
Cortex/Ketamine
F
Raw data
Cortex/Urethane
1 mV
High-pass filtered data
Cortex/Urethane
500 µV
250 ms
G
2 ms
600 µV
H
Ketamine
Urethane
σ RMS
σ Median
Noise in vivo (µV)
Pristine PEDOT Pristine PEDOT Pristine PEDOT Pristine PEDOT
I
Hippocampus/Urethane
Cortex/Urethane
Cortex/Ketamine
P2P Amplitude PEDOT (µV)
P2P Amplitude Pristine (µV)

Figure 3.2 Impact of impedance on data quality. (a) Schematic of a polytrode where electrodes were modified in a 'chess board' pattern. Red circles represent PEDOT-PSS electrodes and blue circles represent pristine electrodes; (b) Stability of PEDOT-PSS deposition protocol. Impedance measured for 3 polytrodes (n_{PEDOT} = 46 and $n_{pristine}$ = 48). Black points denote individual measurement for each electrode (3 measurements for each electrode); (c) Root-mean-square noise (σ_{RMS}) and noise estimate (σ_{Median}) of recordings performed in PBS (n_{PEDOT} = 46 and $n_{pristine}$ = 48). (d) Impedance spectroscopy of PEDOT-PSS coated (n=3) and pristine (n=3) electrodes shows a significant decrease in the impedance real value. The light purple shaded area corresponds to the frequency range in which the thermal noise was computed; (e) 1 s-long raw data traces from 6 electrodes, 3 coated and 3 non-coated, from the recording *amplifier2014_11_25T23_00_08.bin*. This recording was carried out in cortex under ketamine anaesthesia. Top: signals correspond to the 0.1–7.5 kHz frequency band. Bottom: high-pass filtered traces to highlight spontaneous spiking activity. Green arrows indicate the time of spikes identified for a putative neuron; (f) The same representation as in (e) for the recording *amplifier2017_02_02T15_49_35.bin*. This recording was carried out in cortex under urethane anaesthesia; (g) Representative putative neurons from each of the recordings shown above. Left panel corresponds to the cortex/ketamine recording and right panel to the cortex/urethane recording. Schematic of two polytrodes with red and blue colored waveforms and circles denoting the electrodes with higher peak-to-peak amplitudes from each unit, respectively. The asterisks indicates the electrode with the highest amplitude P2P; (h) σ_{RMS} and σ_{Median} of 9 recordings performed in rat cortex, 6 of wich under ketamine, and 3 under urethane (n_{PEDOT_ket} = 96, $n_{Pristine\_ket}$ = 96, n_{PEDOT_ure} = 48 and $n_{Pristine\_ure}$ = 48); (i) The maximum P2P amplitude per unit for coated electrodes and for non-coated is plotted. The P2P amplitude averages from 109 clusters are plotted. In the boxplots, line: median, square: mean, box: 1st quartile–3rd quartile, and whiskers: 1.5 x interquartile range above and below the box.

Figure 3.2e, f and h highlight the variations of noise *in vivo* due to variations in neural firing rate (i.e., biological noise level is highly variable). Note that, in general, the levels of noise under ketamine are higher compared to urethane, due to the increase in background neuronal activity. Moreover, the values of noise vary with the method used to compute the noise magnitude. Higher values for the noise *in vivo* were found when taking into consideration σ_{RMS} values, probably due to a contribution of spikes. The σ_{RMS} value is based on the standard deviation of the signal, which increases with the firing rate(Quiroga et al., 2004). Therefore, the σ_{Median} noise values were used to compare the noise between experiments, and within an experiment. Under urethane the σ_{Median} values from coated electrodes are smaller compared to the non-coated electrodes. On average, the σ_{Median} value was reduced from 8.4 ± 0.4 µV in non-coated to 5.8 ± 0.5 µV in PEDOT coated microelectrodes, a ~ 30 % reduction. Under ketamine the σ_{Median} noise was 15.4 ± 1.2 µV in non-coated and 14.8 ± 1.3 µV in PEDOT coated microelectrodes. The noise values found *in vivo* recordings are highly variable (Figure 3.2h) and the noise reduction observed in saline is likely preserved *in vivo*, yet masked by the much larger background spiking activity noise. Does this difference in noise observed between coated and no-coated electrodes matter for detecting spikes? Usually, the negative voltage deflection of a well isolated unit exceeds 40-70 µV. Therefore, the benefits resulting from the ~ 2 µV noise reduction achieved by coating electrodes would likely be irrelevant for detecting spikes.

Signal characterization: Amplitude of action potentials

Although not producing a major reduction in noise at relevant frequencies, it is still possible that coating electrodes might increase the magnitude of each spike's signal. Figure 3.2g shows two examples of putative neurons where each waveform corresponds to the average of all the spikes from each unit on a given recording electrode. Additionally, red and blue coloured waveforms and circles denote electrodes where the peak-to-peak average amplitude is larger than half of the maximum peak-to-peak average amplitude of the respective unit. Therefore, they represent the electrodes with the highest peak-to-peak amplitude from each unit, respectively.

For each of the 109 putative neurons sorted from 11 recordings, the largest average peak-to-peak amplitudes from the pristine and PEDOT electrode groups were plotted (Figure 3.2 i). Therefore, for each unit, two values are plotted in Figure 3.2i, corresponding to the pristine and PEDOT channel with the largest average peak-to-peak amplitude. If the largest peak-to-peak amplitude spikes are detected by the PEDOT coated electrodes (low impedance electrodes), then the scatter points would fall above the unity line. However, if the largest peak-to-peak amplitude spikes are detected in the pristine electrodes (high impedance electrodes) the scatter points would fall below the line. Our results show that the probability of recording spikes exceeding an amplitude peak-to-peak of 40 μV is similar for coated and non-coated electrodes. Therefore, there is no obvious relationship between impedance and the peak-to-peak amplitude of sorted units in this impedance range (100 kΩ to 1 MΩ).

3.4 Discussion

Internal comparison

The ability to record from closely-spaced sites permitted accurate comparisons between electrodes with two different impedances. The PEDOT-PSS deposition protocol made it possible to decrease impedance up to tenfold on average, from 1.1 ± 0.4 MΩ to 0.084 ± 0.015 MΩ. We divided our noise analysis in non-biological noise (noise measured in saline solution) and biological noise where the level of noise was assessed during recordings *in vivo*. As expected with the impedance reduction, we found a reduction in noise magnitude in saline after coating, since the thermal noise is proportional to the square root of the real part of the impedance (Baranauskas et al., 2011).The reduction in impedance resulted in an average ~ 30 % decrease in the non-biological noise. Nevertheless, when using electrodes *in vivo*, this reduction in the

thermal noise is likely to be obscured by the much larger biological noise, or be insignificant for the detection of spikes with commercial microelectrodes. Moreover, we found no significant effect of impedance on spike amplitude peak-to-peak and detection probability on both coated and non-coated electrodes. In summary, the impedance values found at 1 kHz in commercial silicon polytrode microelectrodes don't seem to affect data quality in terms of spike recording. Moreover, the dataset used to quantify the effect of electrodes impedance on data quality is available online (http://www.kampff-lab.org) and summarized in Appendix B, Table B.1.

But why so many different views about the role of impedance?

Electrophysiological studies have suggested two different views on the impedance impact on data quality. On one hand, studies where decreasing the impedance improves the signal-to-noise ratio, and on the other hand, works where the impedance didn't affect the data quality and subsequent analysis. If we carefully analyse the works where researchers use tetrodes and single microwires, lowering the impedance is beneficial because these low-impedance electrodes minimize signal loss through shunt pathways resulting in larger signals for local field potential and spikes (Ferguson et al., 2009). However, with silicon polytrodes, this shunt capacitance is significantly smaller and does not appear to cause signal attenuation. Furthermore, if polytrodes with higher impedance values (> 2 MΩ) are used for recording action potentials, a voltage divider will be created when using a differential amplifier system as the one from Intan Technologies, which has an input impedance of 13 MΩ.

Should we stop coating our probe electrodes? We believe that microelectrode coatings, in chronic applications, can do more than reduce the impedance. Some coatings can help to promote cell growth at the electrode surface and to minimize the immune responses of brain tissue. Strong neural attachment to implanted electrodes is desirable as it increases interface stability and improves electrical transfer across the tissue-electrode interface (Green et al., 2008; Jorfi, Skousen, Weder, & Capadona, 2015; Kook, Lee, Lee, Cho, & Lee, 2016; Nam, 2012). We thus propose that we stop worrying about impedance (as long as it stays well below the input impedance of your amplifier) and start focusing on bio-compatible materials (Chen & Allen, 2012; Jorfi et al., 2015; Bellamkonda, Pai, & Renaud, 2012).

Chapter 4. CMOS scanning neural probes

Summary

Neural recording devices have traditionally required one output connection for each electrode. This requirement places severe constraints on the number of electrodes that can be accommodated by the thin shaft of an implantable neural probe. Sharing a single output connection between multiple electrodes, as is done in most modern electronic systems, would relax this constraint and permit new designs for ultra-high channel count neural recording devices.

Here we report the design and *in vivo* validation of such a device, a CMOS-based scanning probe with 1344 electrodes and 12 reference electrodes arranged along 8.1 mm of a thin (100 μm) shaft. This neural probe is the outcome of the European research project NeuroSeeker, a consortium of engineers and neuroscientists tasked with building and testing the first implantable CMOS neural probe with every electrode simultaneously accessible via a small number of multiplexed output connections. This new recording technology inevitably presents new challenges for data management, visualization and analysis (i.e., recording of 15 minutes with a CMOS scanning probe consumes around 50 Gigabytes). Therefore, we also present new methods developed within NeuroSeeker for assessing data quality online (i.e., during a recording) and an offline data visualization tool for accelerating manual spike sorting of individual neurons. Having demonstrated the feasibility of an implantable CMOS scanning neural probe, we next consider the future for these new devices. Given the ever-shrinking dimensions of CMOS technology, there is a drive to fabricate smaller, even sub-cellular, electrodes (< 10 μm). Therefore, to explore electrode configurations for future probes, several recordings, from many different brain regions, were performed with an ultra-dense probe containing 255 electrodes, each with a geometric area of 5 x 5 μm and a pitch of 6 μm. This dataset is freely available online (http://www.kampff-lab.org) to help identify optimal electrode configurations specifically tailored to different brain regions and/or cell types.

The offline data visualization tool discussed in this chapter has been accepted for publication: Dimitriadis*, G., Neto*, J. P., & Kampff, A. R. (2018). T-SNE visualization of large-scale neural recordings. *Neural Computation*.

All the results concerning the validation of the CMOS scanning probe and the 256-channel probe

have been prepared for submission and are currently stored as the following preprint: Dimitriadis*, G., Neto*, J. P., Aarts, A., Alexandru, A., Ballini, M., Battaglia, F., ... Kampff, A. R. (2018). Why not record from every channel with a CMOS scanning probe? *bioRxiv*, 275818.

4.1 Introduction

The number of neurons that can be monitored simultaneously during an extracellular recording is largely dependent on the number of electrodes (Stevenson, 2017; Stevenson & Kording, 2011). Therefore, the desire for large-scale monitoring of neuronal activity and the need to minimize tissue damage inflicted when inserting electrodes compete with one another (Buzsáki et al., 2015). Over the years, technical progress has contributed to move from microwires to microfabricated silicon probes. The batch processes of semiconductor fabrication (i.e., photolithographic patterning of thin film conductors and insulators on a silicon substrate) enabled dozens of microelectrodes packed with high-density along needle-like probes, also called polytrodes (Berényi et al., 2014; Blanche, 2005; Buzsáki et al., 2015; Du et al., 2011; Shobe et al., 2015b). In the standard "passive" silicon probe, electrodes distributed along the probe shaft must each be connected to an external contact pad on the probe base by metal lanes deposited along the probe shaft. Advances in lithography techniques (i.e., e-beam lithography (Rios, Lubenov, Chi, Roukes, & Siapas, 2016; Scholten & Meng, 2016)), metal deposition procedures and quality control have made it possible to fabricate a five shank, 1000-channel probe, where each shank (width of ~50 μm) has 200 electrodes of 9 × 9 μm and a pitch of 11 μm (Scholvin et al., 2016). Despite these impressive designs, the bottleneck remains at the bonding interface between the probe and the extracranial connector, which with 1000s of electrodes, has large dimensions and weight when compared with the animal (Scholvin et al., 2016). Therefore, to include thousands of electrodes per square millimetre along a thin shaft and still be able to record from a freely behaving animal, the area taken up by the bonding interface must be reduced. Recently, the fabrication of silicon probes has evolved to include integrated circuits (ICs) in the same substrate used to build the recording electrodes. The fabrication of ICs using CMOS manufacturing processes is the dominant technology in the semiconductor industry due to their large-scale production and optimized workflows. The ubiquitous nature of computers and smartphones has been made possible by the production of ICs with CMOS processes (Theuwissen, 2007). As an example, mobile phones with on board cameras use CMOS image sensors (CIS) that are lightweight and low power, but that can convert an optical image into an

electronic signal (photon-to-voltage conversion) enabling stunning imagery (Figure 4.1a). A CIS is composed of an array of identical pixels, each having at least a photodiode (sensor), an addressing transistor that acts as a switch and an amplifier. Each pixel is sampled once within each frame, being the image output generated by rapidly scanning the full sensor matrix of millions of pixels. The active switching is crucial for achieving the small size of a CIS device, as it multiplexes in time the signals from many pixels onto only a few output wires, that then carry the signal to subsequent amplifiers and digitizer circuits (Figure 4.1b). CMOS circuits are formed by patterning different materials in multiple layers atop a silicon wafer. The fabrication of ICs using CMOS technology is based on four basic microfabrication techniques: deposition, patterning, doping and etching (Brand, 2005). Figure 4.1c illustrates how these techniques are combined to build up an IC layer-by-layer.

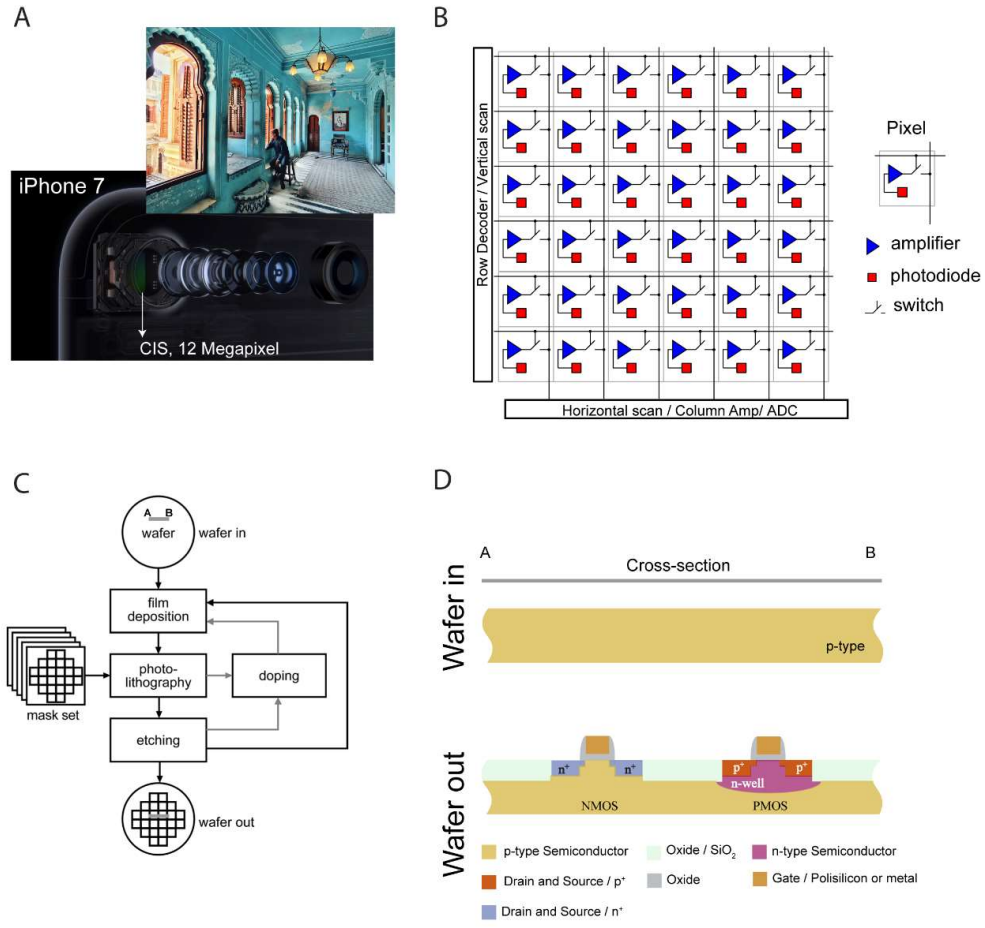

Figure 4.1 Circuits manufactured with CMOS technology. (a) CMOS technology in a smartphone's image sensor. Top: photography using an iPhone7 from https://www.ippawards.com/. Bottom: scheme of camera components from https://www.apple.com; (b) The basic architecture of a CIS (Obien et al., 2015; Theuwissen, 2007) (c) Flow diagram of IC fabrication process using the four basic microfabrication techniques: deposition, photolithography, etching, and doping (Brand, 2005; Fischer et al., 2015).; (d) Schematic of a cross-section of the wafer at the beginning and at the end of the process shown in (c). Two MOSFETs, an n-channel MOS and a p-channel MOS, fabricated with CMOS processes are shown.

In Figure 4.1d, we consider two generic metal-oxide-semiconductor-field-effect-transistors (MOSFETs) fabricated with the CMOS process sequence shown in Figure 4.1c. MOSFETs are important components for building the circuits responsible for multiplexing and amplifying. Generally, a FET can be described as a three electrode device where the current flow between the source and drain electrodes is modulated by varying the potential applied to the gate. The abbreviation MOS describes the device structure and the different layers of material used to build a FET: metal for the gate, oxide for the insulator interface between the gate and the semiconductor to prevent current flow between them, and finally, the semiconductor substrate. When an NMOS transistor is "on" electrons flow from one end, the source, to the other, the drain. Both the source and drain are islands of n-type silicon within a p-type substrate. Application of a positive voltage to the gate electrode, repels holes (missing bonding electrons in p-type semiconductor) and concentrates what few electrons there may be, thus forming an n-channel just under the gate and turning the transistor "on". A p-channel MOS (PMOS) transistor is the mirror image of an n-channel device, with a p-type source and drain within a n-type substrate, and a negative gate voltage which turns it "on" (Robinson, 1984). Therefore, the gate voltage modulates the channel conductance and the MOSFET can be rapidly switched with a small gate voltage from an "off" to "on" state (Veigas, Fortunato, & Baptista, 2015).

The concept of integrating electronic elements in the same substrate used to build the electrodes was first introduced in the 1980s (Najafi & Wise, 1986; Najafi et al., 1985; Wise & Ji, 1992). The most recent CMOS-based probe designs for *in vivo* applications envisage both circuit integration into the probe base and within the probe shaft(s) and have been reviewed elsewhere (Lopez et al., 2013; Lopez et al., 2016; Obien et al., 2015; Raducanu et al., 2016; Ruther & Paul, 2015; Seymour, Wu, Wise, & Yoon, 2017; Steinmetz, 2016) The highest electrode densities and count have been achieved by including time multiplexing into the circuit in a manner similar to CMOS image sensors, where all the electrodes are sampled at fast speeds in a full-frame readout. If a single metal line can be shared by several electrodes, we are no longer restrained by the number of metal lines that can fit within the cross-section of a shank or by the size of the bonding interface in the probe base.

From a circuit perspective, the challenge is to design an architecture that includes a multiplexing circuit for the electrodes within the probe shaft, which requires that each electrode of the array has both its own low-noise amplifier and active switching circuit positioned directly under the electrode. Why? The electrode alone exhibits a high impedance and cannot drive the multiplexed readout lines at sufficient speed. Nonetheless, a low-noise amplifier requires both area and power (Obien et al., 2015), and the available area in a high-density electrode array is

limited, making it difficult to build very low noise amplifiers. Moreover, the amplifier should be of low power to prevent substrate heating, which could damage brain tissue. Nevertheless, integrating amplifiers close to the electrode is advantageous, because it decreases the influence of shunt capacitance and the signal becomes less susceptible to electromagnetic interference.

The European research project, NeuroSeeker aimed to produce CMOS-based silicon probes for extracellular electrophysiological recordings with 1356 electrodes densely packed on a 50 μm thick, 100 μm wide and 8 mm long shank (Figure 4.2a). A detailed description of the technical design of this probe is available elsewhere (Raducanu et al., 2016, 2017). Figure 4.2b shows how the basic principle of the time division multiplexing within the shank allows 8 electrode outputs on a single shank wire. Moreover, additional CMOS circuitry is integrated into the probe base for further processing and transmission. The output from an array of 8 multiplexed electrodes is sent to the base through a shared wire. The signal is fed to an integrator, in the base, whose output is demultiplexed (DMUX block). Each reference electrode is made from a bin of 8 electrodes, therefore the circuit handles, in total, 1440 channels. A total of 180 Integrator-DMUX blocks drive the 1440 channels, which are further amplified and filtered on the base, keeping only the band of interest. These signals are then multiplexed and digitized in groups of 20 channels (10-bit successive approximation analog-to-digital converter) by 72 ADCs. Finally, a digital control block is responsible for generating the clocks for the ADCs and the MUX/DMUX blocks. It also serializes the parallel data from all the ADCs to only 6 data lines (Raducanu et al., 2016). This innovative solution (Figure 4.2c) has allowed the neuroscientists within the NeuroSeeker consortium to record brain activity with unprecedented combination of resolution and scale.

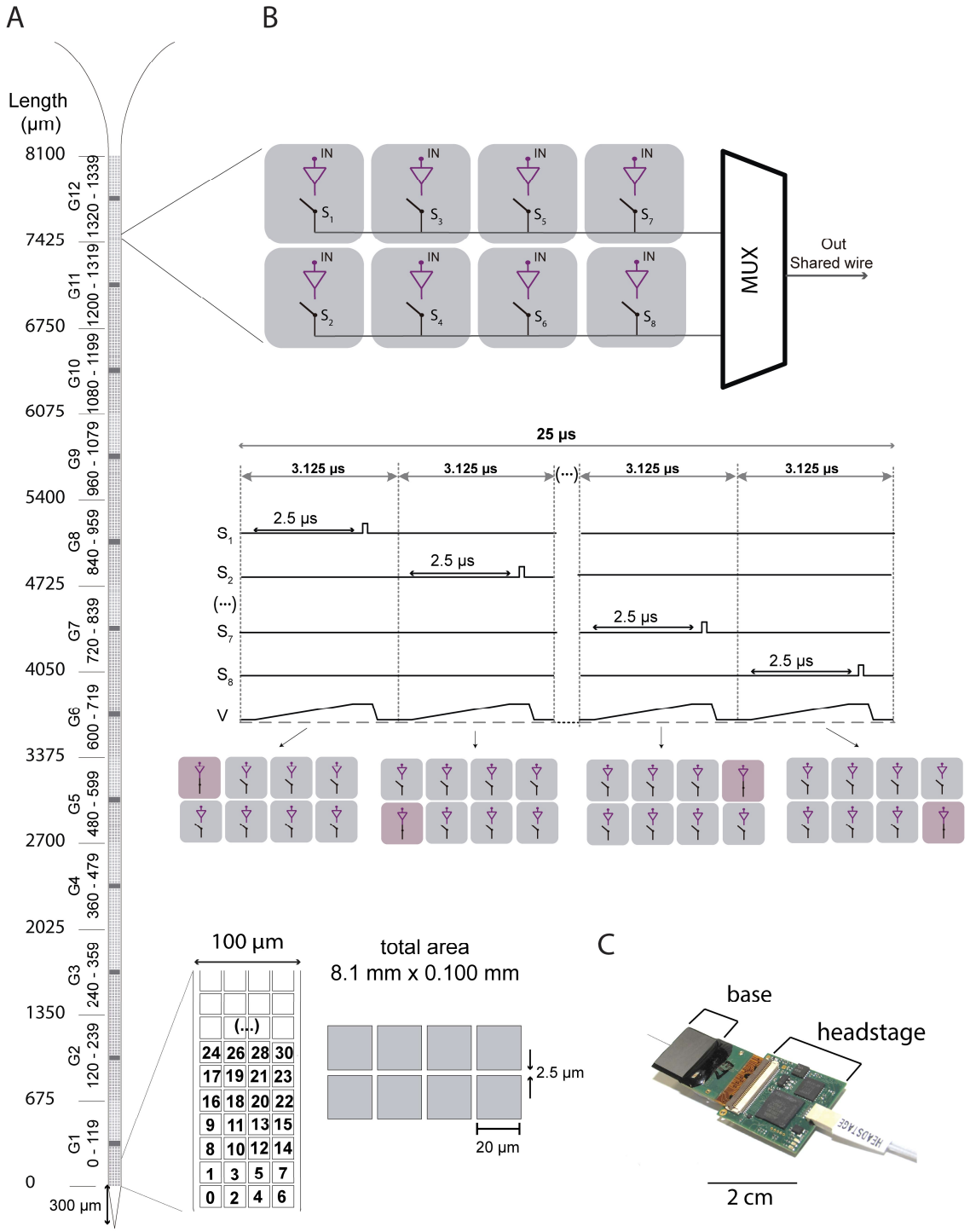

Figure 4.2 NeuroSeeker CMOS-based probe. (a) This probe contains 1344 small electrodes (20×20 µm) with 2.5 µm spacing and 12 larger reference electrodes (40 × 80 µm). The shank is divided into 12 groups (G1 to G12). Each group contains 120 channels: 112 recording electrodes and 1 local reference in the midle of the region made from a bin of 8 electrodes. At the bottom, electrode channel numbers are represented at each site for some electrodes of G1; (b) Top: multiplexing reduces the number of output lines. Switches (S_1 to S_8) and amplifiers are fabricated with CMOS processes. Bottom: the current is integrated for a fixed period of time (T_i= 2.5 µs) over a capacitor (C_i = 15 pF) shared among 8 channels in the probe base. After T_i, the voltage on C_i is sampled and then it is discharged for the next cycle. The integration reduces out-of-band noise acting as anti-aliasing filter. Each channel is oversampled at fs = 40 kHz (neural signal band is limited to ~ 7.5 kHz, therefore fs > 15 kHz), producing a total multiplexing frequency of 320 kHz (Raducanu et al., 2016); (c) Substantially fewer external wires are required than the number of channels.

4.2 Methods

Acute surgery

Rats (400 to 700 g, both sexes) of the Lister Hooded strain were anesthetized with urethane (1.6 g/kg, IP) and placed in a stereotaxic frame. At the initial stage of each urethane surgery, the animal was injected with atropine (0.05 mg/kg, IM), temgesic (20 µg/kg, SC) and rimadyl (5 mg/kg, SC). Anesthetized rodents underwent a surgical procedure to remove the skin and expose the skull above the targeted brain region. Small craniotomies (2 mm medial-lateral and 2 mm anterior-posterior) were performed above the target area. The reference electrode Ag-AgCl wire (Science Products GmbH, E-255) was inserted at the posterior part of the skin incision. Equipment for monitoring body temperature as well as a live video system for guiding probe insertion was integrated into the setup (Neto et al., 2016). The targeted insertion coordinates were scaled according to the size of each rat skull dimensions. We measured the distance between bregma (B) and interaural line (IA), for each animal, to find the ratio between the animal skull and the reference skull (B – IA = 9mm) from Paxinos G, Watson C. *The Rat Brain In Stereotaxic Coordinates* (6th ed.), Elsevier, 2007. After, we adapted the insertion coordinates for targeting specific brain regions with the help of a 3D model rat brain, described elsewhere (Dimitriadis, Fransen, & Maris, 2014). In Figure 4.3 we present an example of the adjustment made for one such recording.

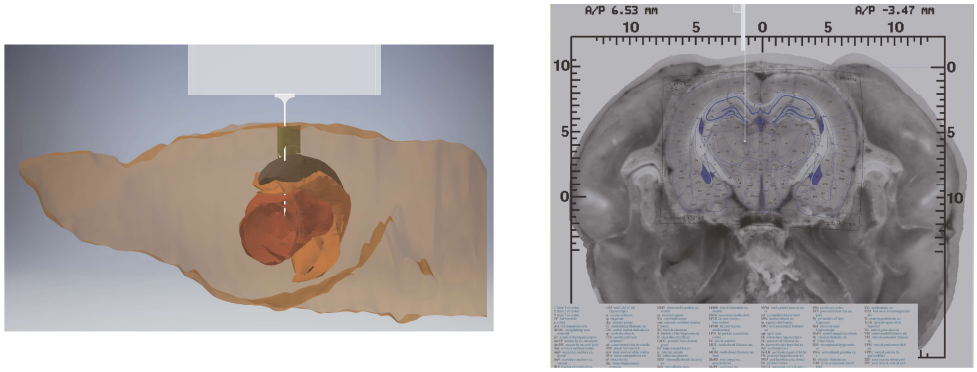

Figure 4.3 Example of insertion coordinates adjustment for an animal larger than the dimensions presented by the brain atlas (B-IA$_{rat}$ = 12.4 mm and B-IA$_{Atlas}$= 9 mm). Left panel: a lateral view of the 3D model with the probe in place. The 3D-model was used to adapt the size of the scalp and brain, taking into account the ratio found (scalp ratio 1.38), and adjust the insertion coordinates. The colour green represents cortex, brown and orange denote hippocampus and red represents thalamus. Right panel: for targeting the brain regions under the stereotaxic coordinates, anterior-posterior -3.4 mm and medial-lateral 1.3 mm, the probe was inserted anterior-posterior -4.7 mm and medial-lateral 1.8 mm. Due to inconsistencies in size between the animal scalp and the Paxinos and Watson Rat Brain Atlas, the functional information from the atlas must be warped to fit the anatomical landmarks of the coronal slices photographs (Dimitriadis et al., 2014).

Recordings *in vivo*

The CMOS-based probes are assembled on a PCB, where the reference (REF) and ground (GND) wires were connected. The recording system consists of the headstage, which configures and calibrates the probe and serializes probe data, a microcoax cable and the base station board with a deserializer chip, that connects to a commercial FPGA development board (Xilinx KC705). The computer used for controlling the NeuroSeeker system is connected to the FPGA board via a 1000base-T Ethernet card. This recording system was also developed by IMEC. The protocol for the acquisition, visualization and saving was implemented in Bonsai, an open-source visual programming framework, which can be freely downloaded (Bonsai, 2017; Lopes et al., 2015). CMOS scanning extracellular signals were sampled at 20 kHz with 10-bit resolution.
For the 256-channel probe recordings we used the Open Ephys (http://www.open-ephys.org) acquisition board along with two RHD2000 128-channel amplifier boards that amplify and digitally multiplex the extracellular electrodes (Intan Technologies). Extracellular signals in a frequency band of 0.1–7,500 Hz were sampled at 20 kHz with 16-bit resolution and were saved in a raw binary format for subsequent offline analysis using a Bonsai interface.

Impedance measurements

For the 256-channel probe, impedance tests (at 1 kHz) were performed using a protocol implemented by the RHD2000 series chip (InTan Technologies) with the electrodes placed in a dish with sterile PBS, 1 mM, pH 7.4 and a reference electrode, Ag-AgCl wire (Science Products GmbH, E-255).

Analysis

For the analysis, the CMOS-based probe recordings were filtered with a band-pass of 500-3,500 Hz and they were saved in binary format using a Bonsai interface. When the external reference was selected, to diminish the effect of artefacts shared across all channels, we subtracted the median signal within each group across the recording electrodes from the respective group. For the 256-channel probes, a third order Butterworth filter with a band-pass of 250-9,500 Hz (95 % of the Nyquist frequency) was used in the forward-backward mode. The noise magnitude was computed as an estimate of the background noise, σ_{Median} = median(|signal(t)|/0.6745), of each

filtered voltage-time trace. Some results were represented as mean ± standard deviation.

4.3 Results

Proof-of-concept: recording *in vivo*

Several recordings were performed with the CMOS-based scanning probes *in vivo* to evaluate the viability of these probes. There are 12 groups on the probe, which can be individually powered, labelled from G1 to G12, in Figure 4.2a. Inside each group, the user can select the reference type (external or internal), gain and frequency bandwidth (high-pass cut-off frequency in AP mode or low-pass cut-off frequency in LFP mode), for each channel individually. Figure 4.4a shows a representative epoch of a recording performed simultaneously within cortex, hippocampus and thalamus from an anesthetized rat. In this recording, 10 of the 12 regions are inside the brain: 1060 electrodes where set in AP (0.5–7.5 kHz) mode and 60 electrodes widely spread along the shaft were set to LFP (1-500Hz) mode. A subset of traces from channels set in AP and LFP mode are plotted in Figure 4.4a. In Figure 4.4a and b, cortex is represented in blue, hippocampus in purple and thalamus in red. The traces in AP mode are displayed in groups (c1, c2, c3, cg, h1, h2, h3, h4, t1, t2, t3 and t4) that correspond to a location on the probe shaft displayed on the left (each black box indicates the position of the group). Moreover, traces of 11 out of 60 LFP mode electrodes are plotted between the group traces. The presence of fast voltage deflections in several traces reveals that the activity of multiple neurons has been detected. Furthermore, the NeuroSeeker probe densely samples the local electric field, providing a detailed description of the spatiotemporal profile of a neuron's extracellular action potential as shown in Figure 4.4c.

To evaluate if the data quality deteriorates with increasing number of groups being powered, we computed the noise of 212 electrodes (from groups G1 and G2) set in AP mode while enabling (powering on) more groups along the shank. The noise level with 2 groups and 12 groups powered is 10.2 ± 0.1 μV and 12.0 ± 0.1 μV, respectively. Additionally, the noise magnitude was computed for 1012 channels (half of group 10's electrodes are outside of the brain) using the external or the internal reference configuration while recording. The measured noise using the external and internal reference is 11.7 ± 0.1 μV and 12.5 ± 0.1 μV, respectively. The noise magnitude computed across datasets revealed no significant variability. Several recordings were

performed at different depths, with different reference configurations, and number of active regions. This data is available online (http://www.kampff-lab.org/) and summarized in Appendix C, Table C.1. Figure 4.4 illustrates one of those recordings, *18_26_30.bin*.

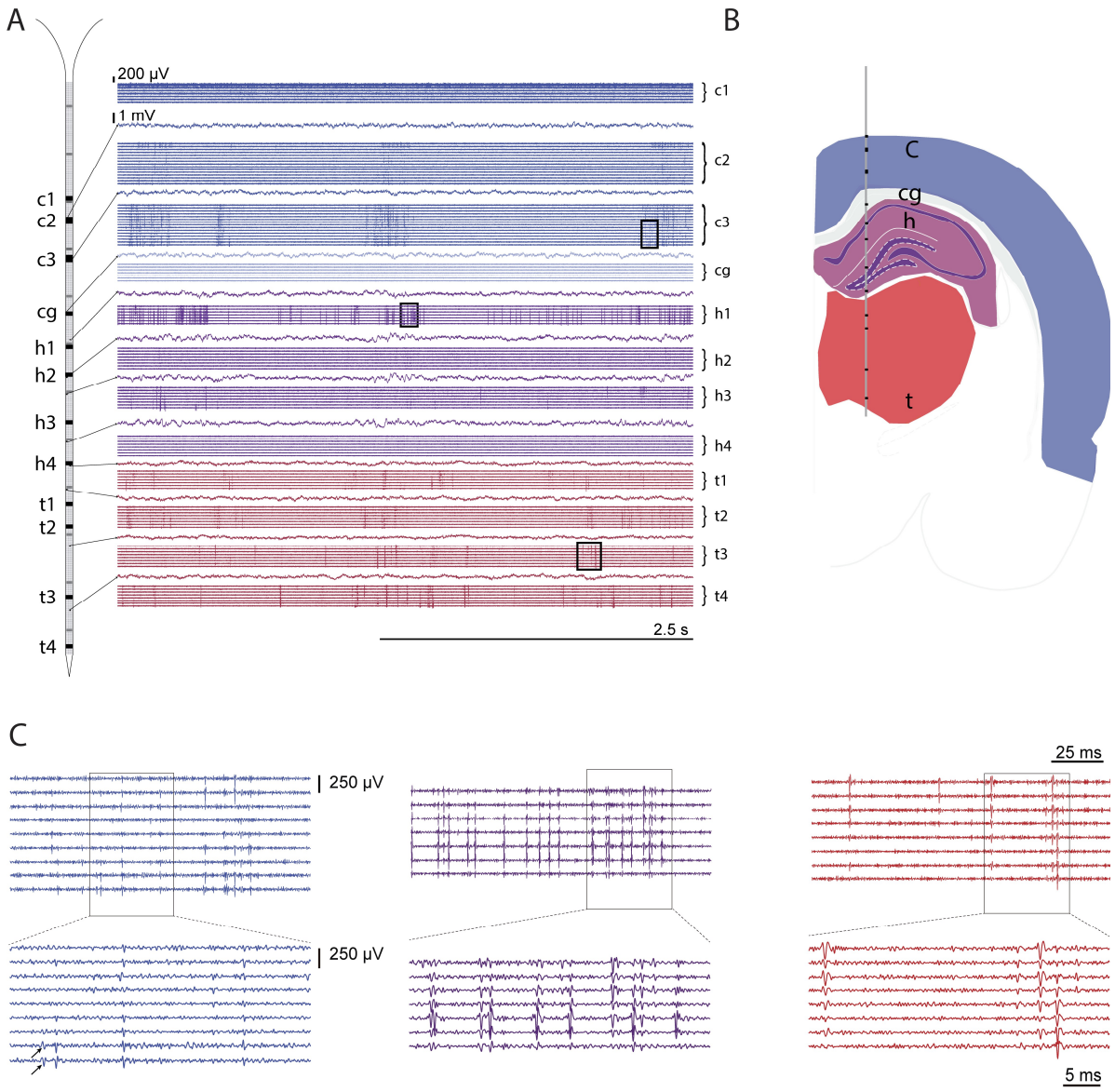

Figure 4.4 Example of a recording performed with 1120 electrodes simultaneously within cortex, hippocampus and thalamus from an anesthetized rat. (a) 5-s-long LFP and AP traces of a probe spanning multiple brain regions; (b) Schematic of coronal slice signaling the groups position shown in (a) as black blocks. 'c, 'cg', 'h' and 't' denote the anatomic locations of cortex, cingulum, hippocampus and thalamus, respectively. The estimated probe position was based on the insertion coordinates and physiological signatures.From the point of insertion to the tip, the recording length was 6.7 mm; (c) Short epochs of AP band traces from groups c3, h1 and t3 (color-coded), illustrating the presence of diverse spike waveforms on several electrodes. These sections are highlighted in (a) by boxed areas on top of traces.

Data visualization (online analysis)

Note that the signal traces presented in Figure 4.4 are just a small fraction of the total number of electrodes (105 of 1060 electrodes) recorded (see all voltage traces in Figure C.1 in Appendix C). These new CMOS scanning probes clearly raise new challenges for the presentation and analysis of the acquired data due to their large number of electrodes. This challenge first appears when the user wants to monitor a live recording, either to assess the signal quality appearing on each electrode or to better position the probe within the desired brain structure(s). Visualizing 1356-time series is difficult, even on an HD monitor with 1080 rows of pixels. Furthermore, rendering voltage by time traces, the conventional representation for live physiology signals, is computationally expensive. However, modern graphic processors (GPUs) were specifically designed to parallelize these visualization tasks. We therefore developed a custom visualization pipeline using Bonsai by transferring each buffer of acquired probe data directly to the GPU and then using fragment shaders to render all probe data to the monitor in real-time. The visualization shown in Figure 4.5 is a screen capture of one such online visualization in which the voltage signal of each channel is rendered from red to blue. A neuron's extracellular field is detected on many adjacent electrodes, and thus spikes in this visualization appear as a coloured block of red and blue stripes.

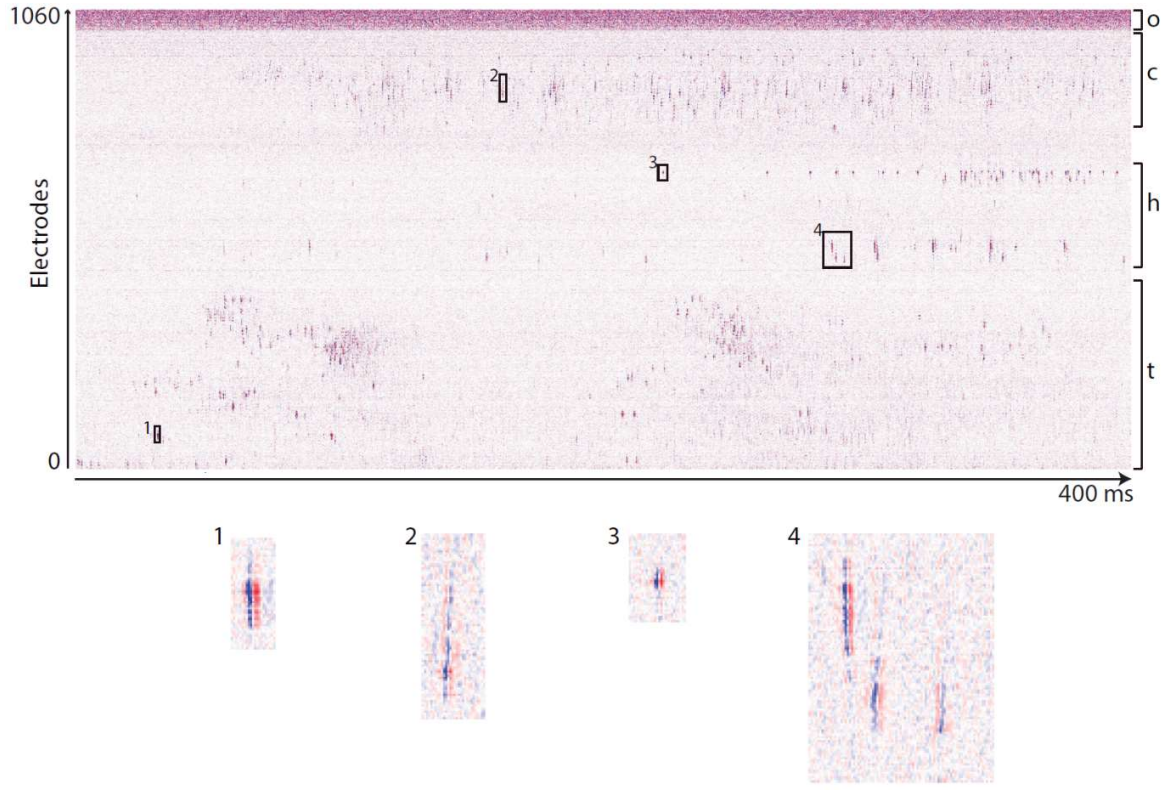

Figure 4.5 GPU visualization of the voltage traces from all (1060) electrodes in AP mode. The voltage traces recorded by each electrode (row) are displayed as a color saturation for each 100 microsecond bin (column). Red represents positive voltages, blue negative voltages and white represents voltages around zero. This image shows 400 milliseconds of data recorded simultaneously in cortex, hippocampus and thalamus. 'o': out of the brain, 'c': cortex, 'h': hippocampus and 't': thalamus.

Data processing (offline analysis)

Spike sorting algorithms are used to extract and classify the activity of individual neurons from the recorded voltage traces. The basic steps in the spike sorting pipeline are as follows: the (high-passed filtered) data first goes through a process of spike detection; dimensionality reduction is then used to transform the space-time spike signal into a smaller set of features computed for each spike (e.g., waveform features evaluated by principal component analysis); finally, automated clustering or classification methods are applied, where spikes from an isolated single-unit are grouped together in the reduced dimensional space of these features. After these automated stages, an operator then manually checks the output of the automatic cluster analysis algorithm, drawing boundaries around the resulting clusters and correcting mistakes the algorithm has made (Dimitriadis et al., 2016). The manual intervention in the data-processing pipeline raises the potential for subjectivity and bias to occur, but it is still heavily used in the majority of the laboratories (Chung et al., 2017; Harris et al., 2016). Although a fully automatic spike sorting algorithm is clearly desirable (even more so for large-scale extracellular recordings) it has not yet proven possible to implement a fully automated algorithm that works robustly (Harris et al., 2016).

Embedding techniques, such as t-sne, transform the position of points in a high-dimensional space to positions in a lower (usually two) dimensional space to aid visualization. Points that are close in the original space are attracted to each other until they get roughly equally close in the 2D space, while points that are far away in the original space are repelled by each other in the 2D space (Figure 4.6). T-sne's 2D embedding makes visualizing and curating the high dimensional output of automated spike clustering algorithms a much simpler procedure and also provides an "overview" of the otherwise overwhelmingly large, high-dimensional datasets (Dimitriadis et al., 2016).

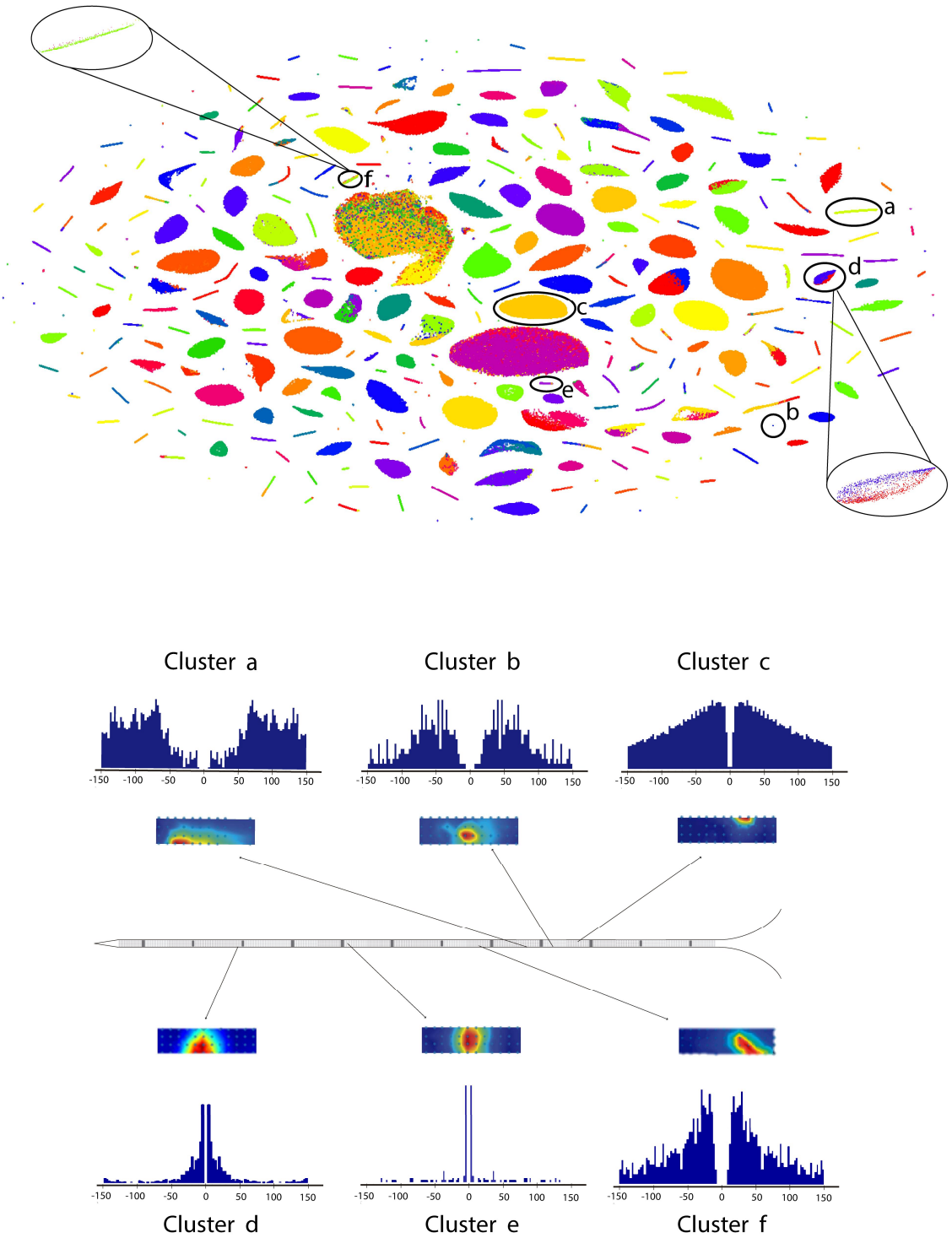

Figure 4.6 T-sne embedding of the kilosort algorithm (distances to templates) result for the recording *18_26_30.bin*. Top: we ran the kilosort algorithm on a recording with the maximum number of templates set to 2240. It generated 588 templates and detected 513,722 spikes. The colors represent spikes assigned to different templates. Bottom: a schematic of the probe where clusters from 'a' to 'f' were manually selected on the t-sne plot with the corresponding lettered eclipse. These clusters are from different parts of the probe as shown in the scheme. Heatmaps show the peak-to-peak value of the averaged spike for each cluster. The number of electrodes represented in the heatmaps is 48. The histogram insert shows the autocorrelogram (±150 ms, 1-ms bin width) of the spikes for each cluster. Spike groups 'd' (a thalamic unit) and 'f' (a hippocampus unit) are two examples of merging within the t-sne plot of 2 and 3 kilosort templates, respectively.

4.4 Discussion

Researchers, companies and funding agencies across the globe have invested their time and money to build neural probes with large and dense arrays of microelectrodes. Widely used technology for constructing modern devices, the CMOS process, was used to fabricate a probe with integrated circuits on the same substrate as the electrodes, allowing the highest density and number of parallel readout electrodes in a silicon probe ever achieved in the history of neuroscience for *in vivo* recordings. Ultimately, all the voltage traces should be translated into spikes from single neurons. Due to the increase in the amount of data, new approaches for analysing the datasets were also developed during this work, such that the data could be 'digested' in a short period of time. This is a powerful new tool that brings not just a change in the amount of data but also the opportunity to ask new questions (Dyson, 2012; Focus on the neuroscience toolbox, 2016).

Future directions

What must be done to achieve the full potential of massively parallel neuronal recordings?
The CMOS-based probe has 20 x 20 µm with 2.5 µm spacing between electrodes, but because of the ever-shrinking dimensions in CMOS technology, it is now possible to fabricate much smaller electrodes. For instance, the CIS from an iPhone 7 comprises 12 megapixels arranged in a square of roughly 6 x 6 mm, where the pixel is less than 2 µm.
Many studies have now shown that more densely spaced electrodes will increase spike sorting quality, as the spikes from two neurons can appear similar when detected with a small number of electrodes (Dimitriadis et al., 2016; Moore-Kochlacs, 2016; Rossant et al., 2015). How small and closely-packed can one make extracellular microelectrodes? A probe containing 255 electrodes with a geometric area of 5 µm x 5 µm and spacing of 1 µm was fabricated by IMEC (Figure 4.7a). We gathered a dataset of recordings using this probe in different brain regions, with the goal of understanding at what spatial scale the signals from neighbouring electrodes became redundant (i.e., the extracellular signal was spatial over sampled). As shown in Figure 4.7b, the probe electrodes have a low value for the impedance at 1 kHz, 790 ± 100 kΩ. Note that, 16 of the 255 electrodes are non-functional because their impedance value at 1kHz is higher than 2 MΩ. The noise magnitude computed in saline for the functional electrodes is 5.09 ± 0.03 µV (Figure 4.7b).

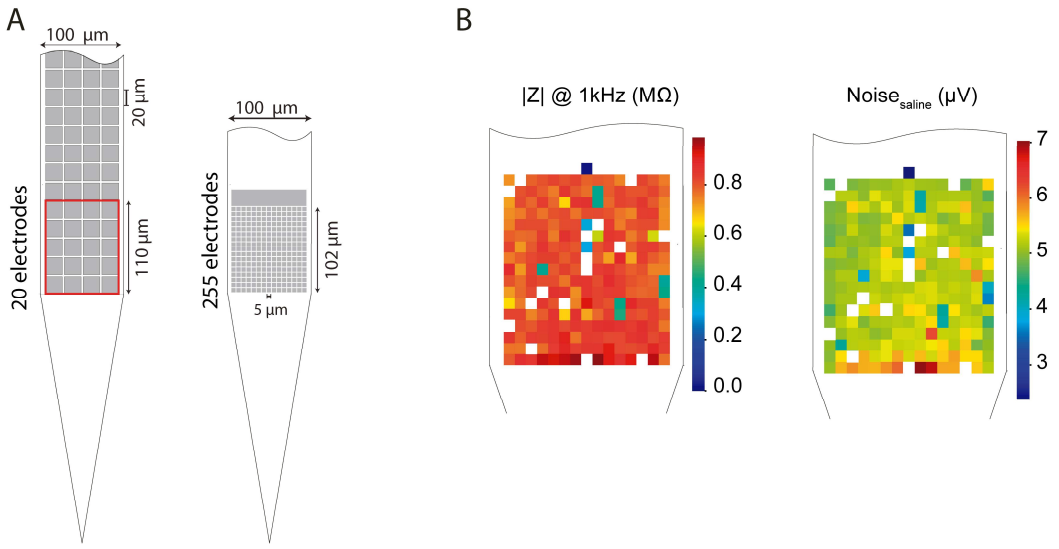

Figure 4.7 The 256-channel probe: dimensions, impedance and noise. (a) Schematic of the dimensions of the 256-channel probe compared with the CMOS-based probe. The probe contains a large reference electrode on the top of the array; (b) Electrical properties of 5 x 5 µm electrodes. Left: the majority of electrodes report an impedance magnitude at 1 kHz lower than 1 MΩ, but 16 of the 255 sites are non-functional because the impedance is higher than 2 MΩ (electrodes represented by white squares). Right: noise magnitude in saline solution. The noise measurements were performed with the probe in a dish with saline solution and a reference electrode, Ag-AgCl wire (Science Products GmbH, E-255). The white squares denote the non-functional electrodes.

Several recordings were performed with this probe within different brain regions (Figure 4.8a). The data shown in Figure 4.8b illustrate the ability of this ultra-high-density array of electrodes to detect activity from the same neuron on several adjacent electrodes. With the present dataset it is possible to explore the optimal electrode configuration (i.e., electrode size and density) required to record and isolate spikes, which may be specific to different brain regions, with different neuron types (i.e., different cell sizes and dendritic configurations) and different neuron densities, and thus require "custom-fit" probes for effective neuron isolation (Buzsáki et al., 2015).

In addition to these physical design choices, progress in large-scale neuronal recording will depend on the development of new methods for spike sorting. For example, given the large datasets acquired with the CMOS-based probes, we practically require fully automatic spike sorting algorithms.

Ultimately, "ground truth" data, for which one knows exactly when a neuron in the vicinity of an extracellular probe generates an action potential, is necessary to validate and quantify the performance of new algorithms to automatically detect/sort single-units and new electrode configurations (Chung et al., 2017; Jun et al., 2017; Neto et al., 2016; Yger et al., 2016).

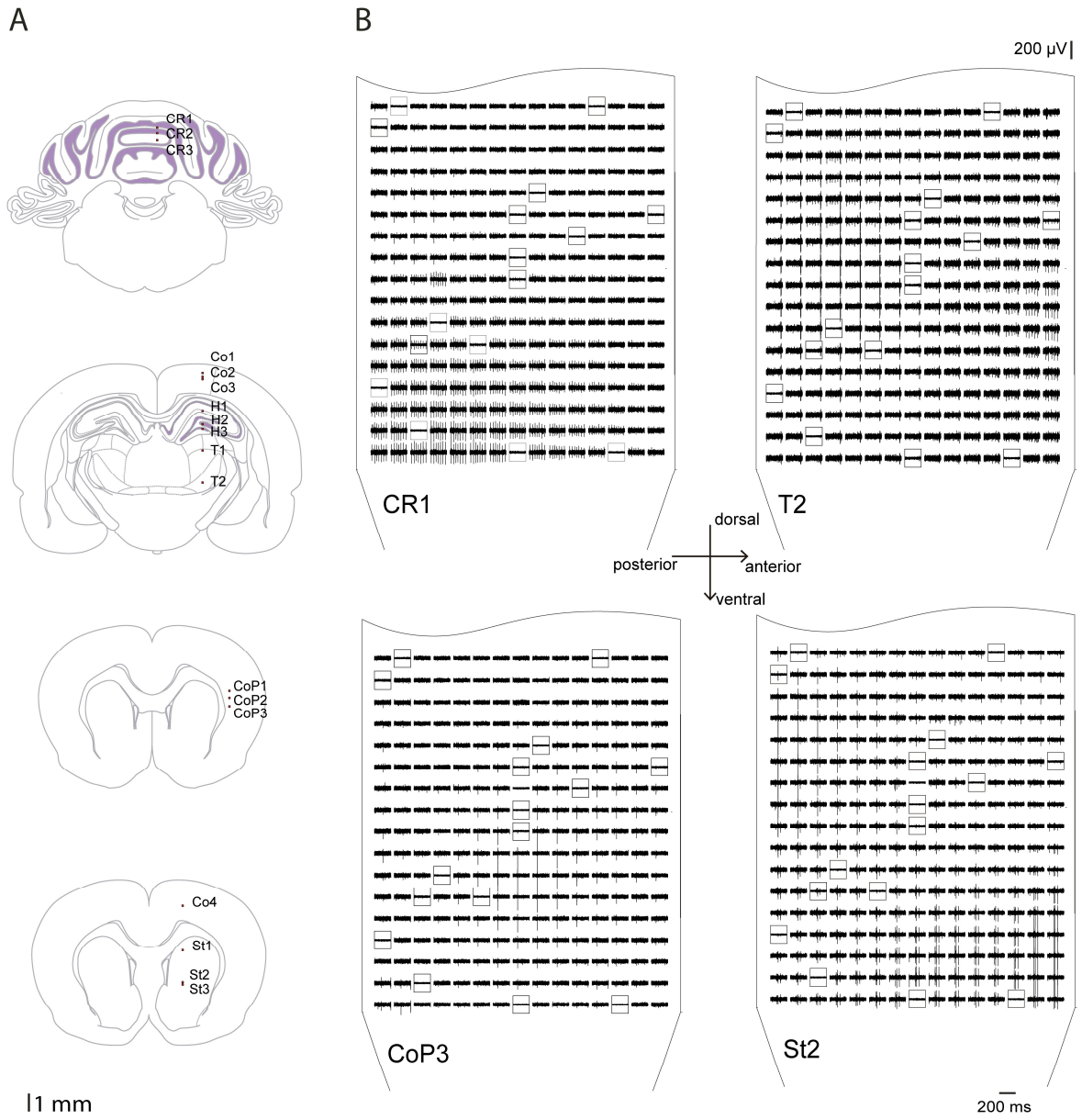

Figure 4.8 Acute recordings performed with a dense array of small electrodes in different brain regions. (a) Schematics of coronal slices (Paxinos & Watson, 2007) signaling the recording positions (red dot represents the position of the tip). See dataset summary in Appendix C, Table C.2; (b) Different patterns of voltage deflection within the electrodes array introduced by neuronal activity across different brain regions. The black rectangles denote the non-functional electrodes.

Chapter 5. Validating silicon polytrodes with paired juxtacellular recordings: method and dataset

Summary

Cross-validating new methods for recording neuronal activity is necessary to accurately interpret and compare the signals they measure. Here we describe a procedure for precisely aligning two probes for *in vivo* "paired-recordings" such that the spiking activity of a single neuron is monitored with both a dense extracellular silicon polytrode and a juxtacellular micro-pipette. Our new method allows for efficient, reliable, and automated guidance of both probes to the same neural structure with micron resolution. We also describe a new dataset of paired-recordings, which is available online. We propose that our novel targeting system, and ever expanding cross-validation dataset, will be vital to the development of new algorithms for automatically detecting/sorting single-units, characterizing new electrode materials/designs, and resolving nagging questions regarding the origin and nature of extracellular neural signals.

All the results concerning the cross-validation method and paired-recordings have been published as: Neto, J. P., Lopes, G., Frazão, J., Nogueira, J., Lacerda, P., Baião, P., ... Kampff, A. R. (2016). Validating silicon polytrodes with paired juxtacellular recordings: method and dataset. *Journal of Neurophysiology*, 116(2), 892–903. http://doi.org/10.1152/jn.00103.2016.

5.1 Introduction

Understanding how the brain works will require tools capable of measuring neuronal activity at a network scale, i.e., recording from thousands of individual neurons (Buzsáki, 2004). Technical advances have driven progress in large-scale neural recordings, and the development of microfabricated silicon polytrodes enables a potential increase in the number of neurons that can be simultaneously monitored (Berényi et al., 2014; Michon, Aarts, Borghs, Bruce, & Fabian, 2014; Shobe, Claar, Parhami, Bakhurin, & Masmanidis, 2015; Stevenson & Kording, 2011). However, each improvement in recording technology inevitably raises new questions about the nature of the signal and demands new analysis methods to interpret these growing datasets.

Extracellular recording is unique in its ability to record populations of neurons deep in the brain with sub-millisecond resolution; it also poses particularly daunting challenges for analysis. Each electrode is sensitive to the spiking activity of hundreds of neurons in its vicinity, and sorting this cacophony into individual sources is a challenge (Marblestone et al., 2013). Furthermore, fundamental questions regarding how each neuron participates in the bulk extracellular signal remain unresolved: how many neurons contribute to the signal detected by an electrode? How does a neuron's contribution decay with distance from the probe? Do different types of neurons have different extracellular signatures? Are extracellular recordings biased for particular types of neurons? How does the presence of the probe interfere with the activity of the surrounding brain tissue? Answers to these questions will require experiments to validate existing and future extracellular electrode technology as well as new analysis methods to interpret their data.

Employing modern methods for integrated circuit design and fabrication, probes with thousands of discrete sites are now being developed (Dombovári et al., 2014; Ruther & Paul, 2015; Shobe et al., 2015a). These devices will densely sample the extracellular electric field, such that one nearby neuron will be detected by many individual electrodes, and will thus provide a detailed description of the spatiotemporal profile of a neuron's extracellular action potential. It is expected that this additional detail will significantly aid analysis methods for the detection and isolation, and possibly type identification, of individual neurons in the vicinity of the probe, yet methods capable of utilizing such a dense sampling are just now being developed (Dimitriadis et al., 2016; Lewicki, 1998; Pachitariu et al., 2016; Rey et al., 2015; Rossant et al., 2016; Yger et al., 2016).

"Ground truth" data, for which one knows exactly when a neuron in the vicinity of an extracellular probe generates an action potential, is necessary to validate the performance of these new

recording devices and analysis procedures. However, the validation datasets currently available for extracellular recordings only exist for tetrodes and single-wire electrodes (Chorev & Brecht, 2012; Henze et al., 2000; Henze & Buzsáki, 2007; Wehr, Pezaris, & Sahani, 1999) or are from in vitro preparations (e.g., slices (Anastassiou, Perin, Buzsáki, Markram, & Koch, 2015) and cultured neurons (Jäckel et al., 2017)) in which the majority of background neuronal activity has been surgically removed. Evaluating the existing silicon polytrodes *in vivo*, as well as forthcoming ultra-high density CMOS probes, will require new datasets, and, ideally, new methods for efficiently gathering this vital cross-validation data.

Targeting a single neuron close to an extracellular probe with another electrode requires accurately positioning both devices deep in neural tissue. When performed blindly, the efficiency of achieving paired-recordings in which one neuron is detected by both probes is rather low, making such validation experiments much more difficult than just haphazardly recording extracellular neural signals. For this reason, such datasets are very rare, however, the ones that do exist (for tetrodes in the hippocampus) have been invaluable (Gold, Henze, & Koch, 2007; Harris et al., 2000). We anticipate that a large amount of such validation data will be required to characterize the large-scale neural recording devices currently being developed, and we thus set out to make paired-recordings easier.

In the following we report a new method for efficiently and reliably targeting, blindly, two different recording devices to the same region in the brain. This method was then used to acquire a "ground truth" dataset from rat cortex with 32 and 128-channel silicon polytrodes, which can now be used to validate methods for interpreting dense extracellular recordings and help resolve persistent debates about the nature and origin of the extracellular signal. This dataset, which will grow as new devices are fabricated, is available online (http://www.kampff-lab.org/validating-electrodes).

5.2 Methods

Setup design and calibration

The dual-recording setup requires two aligned, multi-axis micromanipulators (Scientifica) and a long working distance optical microscope (Figure 5.1a). A PatchStar (PS) and an In-Vivo Manipulator (IVM) are mounted on opposite sides of a rodent stereotaxic frame. The stereotaxic

frame also defined the common X, Y and Z axes to which the manipulators were aligned: X axis is parallel to the medio-lateral axis; Y axis is parallel to the anterior-posterior axis and Z axis is parallel to the dorso-ventral axis.

The probes were held at an angle: the PS allows the combination of two motion axes (XZ axis in approach mode) and this approach angle was set at 61° from the horizontal, whereas the IVM, a rigid 3-axis linear actuator, was tilted 48.2° from the horizontal around the Y axis. The use of two different models of manipulator was a practical constraint in this study, as the IVM permitted a greater range of travel for initial prototyping. However, future dual-probe setups will utilize two PS systems and the calibration and operation procedures will remain identical.

Microscope alignment

A custom microscope was assembled from optomechanic components (Thorlabs), a long-working distance objective (Infinity-Corrected Long Working Distance Objective, 10x, Mitutoyo), and a high-resolution CMOS camera (PointGrey). The numerical aperture of the objective (0.28) had a theoretical resolution limit of ~ 1 μm in X and Y directions and ~ 10 μm in Z direction, which was oversampled by the camera sensor. Oblique illumination was necessary to acquire an image of both the extracellular probe and juxtacellular pipette, directly above the craniotomy, with sufficient contrast to accurately "zero" the position of each probe (Figure 5.1a, upper left panel). The repeatability of visually aligning each probe to the center of the image ("zeroing") was evaluated by manually moving the tip of the pipette several times (n = 11) from outside the field-of-view to the focal plane and image center and recording the manipulator coordinates. The optical alignment procedure had 0.5 ± 0.5 μm repeatability in XY and 2.6 ± 1.7 μm in Z.

Mechanical alignment

Ensuring that the axes from both manipulators are parallel began with a mechanical alignment procedure. The PS was "squared" with the stereotactic frame using a digital machinist's dial (Fine reading Indicator, RS Pro) mounted in the electrode holder, using exactly the same procedure that a machinist uses to align a milling machine XY table and column. The dial was placed in contact with a planar surface of the stereotactic frame and moved along this surface (see Movie 1 in http://www.physiology.org/doi/suppl/10.1152/jn.00103.2016/suppl_file/Movie_1.mp4).

Any change in the micron-sensitive dial's readings during movement indicated a misalignment, and the manipulator was repeatedly "realigned" (i.e., tapped with a soft surface hammer) until this differential was minimized. The IVM manipulator was then aligned using the same procedure in the Y axis using both the vertical and horizontal planes of the stereotactic frame.

Estimating misalignment

Each probe tip was positioned, sequentially, at the center of the microscope image (indicated by an overlay crosshair) and the respective motorized manipulator coordinates were set to zero (X = 0, Y = 0, Z = 0) (Figure 5.1a). The pipette was then moved to a different position in space while the microscope was moved and refocused to re-center the tip of the pipette in the crosshair. Next, without moving the microscope, we moved the extracellular probe to the same coordinates as the pipette. If there were no misalignment between the two manipulators, then the probe should arrive at the center of the image crosshair. If the probe is not centered, then the amount of re-positioning required (in X, Y and Z) to venter the probe provides an accurate measure of residual axis misalignment. These "errors" were recorded for each position as the probes were sequentially moved to several different locations (n = 15) spanning a large volume (5000 x 5000 x 5000 μm, in 1000 μm steps). Following mechanical alignment, the average distance error recorded in this volume was 75.6 ± 36.2 μm (n = 15). Note that our manipulators were mounted with different approach angles (θ_{IVM} = 48.2°) and converting the coordinates of the IVM into the PS frame requires the following transformation and assumes perfect Y-axis alignment.

$$X_{PATCH} = \cos(\theta_{IVM})\, Z_{IVM} + \sin(\theta_{IVM})\, X_{IVM}$$
$$Y_{PATCH} = Y_{IVM}$$
$$Z_{PATCH} = -\sin(\theta_{IVM})\, Z_{IVM} + \cos(\theta_{IVM})\, X_{IVM}$$

Equation 5.1

Software correction

By using one manipulator as the reference, we can use the position errors measured at many different locations to estimate the coordinate transformation that best compensates for the misalignment of the second manipulator. We adopted the PS coordinate system as the reference

frame and transformed the recorded IVM coordinates into the PS frame, in an affine manner, as follows for the X axis: $X_{PATCH} = A \cdot X_{IVM}$, where A represents a transformation matrix that best matches these pairs of coordinates. The distance error estimated after the software alignment was reduced to 10.5 ± 5.2 μm (n = 15).

The protocol for the acquisition and transformation of axis position was implemented in Bonsai, an open-source visual programming framework, which can be freely downloaded at (Bonsai, 2017; Lopes et al., 2015).

Surgery

Rats (400 to 700 g, both sexes) of the Long-Evans strain were anesthetized with a mixture of ketamine (60 mg/kg IP) and medetomidine (0.5 mg/kg IP) and placed in a stereotaxic frame that was atop a vibration isolation table (Newport). Equipment for monitoring body temperature as well as a live video system for performing craniotomies and durotomies was integrated into the setup. At the initial stage of each surgery atropine was given to suppress mucus secretion (atropine methyl nitrate, Sigma-Aldrich). Anesthetized rodents underwent a surgical procedure to remove the skin and expose the skull above the targeted brain region. Small craniotomies (4 mm medial-lateral and 2 mm anterior-posterior) were performed above dorsal cortex. The craniotomy centers were 2.5 mm lateral to the midline and ranged from +4 to -4 anterior-posterior, thus exposing either motor, sensory or parietal cortex. Two reference electrodes Ag-AgCl wires (Science Products GmbH, E-255) were inserted at the posterior part of the skin incision on opposite sides of the skull.

Dense silicon polytrodes

All experiments were performed with two different high-density silicon polytrodes. A commercially available 32-channel probe (A1x32-Poly3-5mm-25s-177-CM32, NeuroNexus), with 177 μm^2 area electrodes (iridium) and an inter-site pitch of 22-25 μm, was used in the first experiments. The impedance magnitude for these electrodes at 1 kHz was ~ 1 MΩ, but for some experiments, a PEDOT-PSS coating was applied to lower this impedance to ~ 50-100 kΩ. In later experiments, we used a 128-channel probe produced by the collaborative NeuroSeeker project (http://www.neuroseeker.eu/) and developed by IMEC using CMOS-compatible process technology. The probe's titanium nitride electrodes were 400 μm^2 (20 x 20 μm^2) in size, arranged

at a pitch of 22.5 μm, and had an impedance magnitude of 50 kΩ at 1 kHz.
Before each surgery, the impedance magnitude of each electrode site was measured for diagnostic purposes using a protocol implemented by the amplifier/DAC chip (InTan Technologies). Following each surgery, cleaning was performed by immersing the probe in a trypsin solution (trypsin-EDTA (0.25 %), phenol red, TermoFisher Scientific) for 30-120 minutes and rinsing with distilled water.

Probe insertion and simultaneous juxtacellular-extracellular recordings

After both the extracellular probe and juxtacellular pipette positions were sequentially "zeroed" to the center of the microscope image, the microscope was replaced by a macro-zoom lens (Edmund Optics) for visually guided insertion. The extracellular probe was inserted first, at a constant velocity of 1 μm/s, automatically controlled by the manipulator software. When the extracellular probe was in place the juxtacellular pipette filled with 1x PBS was then lowered through a second durotomy under visual guidance using the overhead surgery camera. We used capillary borosilicate glass tubing with flame polished ends, an outer diameter of 1.50 mm, inner diameter of 0.86 mm, and a length of 10 cm (Warner Instruments). The tubing was pulled into micropipettes using a laser-based micropipette puller (P-2000, Sutter Instrument). The resulting juxtacellular pipettes had resistances between 3 and 7 MΩ and tip diameter about 1-4 μm. As the pipette approached the extracellular electrodes, we followed a protocol for performing loose-patch recordings from neurons as previously described (Herfst et al., 2012). Positive pressure (25-30 mmHg) was reduced on the pipette to 1-10 mmHg (DPM1B Pneumatic Transducer Tester, Fluke Biomedical) and the amplifier for juxtacellular recordings (ELC-01X, NPI) was set to voltage-clamp mode (25 mV steps at 20Hz). As the electrode was advanced towards a cell membrane, we observed an increase in the pipette resistance. If spikes were observed, the pressure was then released (0 mmHg) and a slight suction applied to obtain a stable attachment to the cell membrane. A data acquisition board (National Instruments) was used to control amplifier voltage commands. After a stable recording was achieved, simultaneous recording of both extracellular and juxtacellular electrodes used exclusively the Open Ephys (http://www.open-ephys.org) acquisition board, where ADCs (used for the juxtacellular signal) along with the RHD2000 series digital electrophysiology interface chip that amplifies and digitally multiplexes the extracellular electrodes (Intan Technologies). Extracellular signals in a frequency band of 0.1-7,500 Hz and juxtacellular signals in a frequency band of 300-8,000 Hz were sampled

at 30 kHz with 16-bit resolution and were saved in a raw binary format for subsequent offline analysis using a Bonsai interface. For the analyses described in the following, a third order Butterworth filter with a band-pass of 100-14,250 Hz (95 % of the Nyquist frequency) was used in the forward-backward mode. For some recordings we noticed a high-frequency noise contribution and we thus used a band-pass of 100-5,000 Hz.
All experiments were approved by the Champalimaud Foundation Bioethics Committee and the Portuguese National Authority for Animal Health, Direcção-Geral de Alimentação e Veterinária.

5.3 Results

Setup design

The "dual-probe" positioning and recording setup presented in Figure 5.1a was designed to reliably target neural cell bodies located within ~ 100 μm of the polytrode electrode sites without optical guidance. In this setup, the motorized manipulators, video capture, online visualization, and extra- and juxtacellular voltage recordings were integrated by custom open-source software developed within the Bonsai framework (Lopes et al., 2015).
Following a mechanical alignment and software calibration of both manipulators' axes, each paired-recording experiment began with the optical "zeroing" of both probes. Each probe was positioned, sequentially, at the center of the microscope image (indicated by a crosshair) and the motorized manipulator coordinates set to zero (Figure 5.1a). As shown in Figure 5.1b, this alignment was performed directly above the desired *rendez-vous* point inside the brain, as close as possible above dura, usually between 1 and 4 mm, but far enough to reduce background light reflected from the brain surface into the microscope image. During optical calibration it is possible to select any point on the polytrode to be the origin (X = 0, Y = 0, Z = 0) by aligning that point of the probe in the reticule. However, the distance reported in the subsequent data is always the Euclidean distance between the tip of the pipette and the closest extracellular electrode.
With practice, multiple cells in the vicinity (less than 200 μm) of the polytrode could be recorded through multiple insertions of the juxtacellular pipette (Figure 5.1c is a schematized example of one paired-recording). Before the surgeries, we validated the alignment of the motors by moving both probes independently from the calibration point (0, 0, 0) towards a different point in space and recording the position difference between them after travel. During our experiments, the

movement of the probes primarily occurred in the XZ plane. We found that when we moved both probes to a new Z position 3 mm below the calibration point (0, 0, -3), similar to an actual recording experiment (Figure 5.1b), the distance error observed was 10.5 µm after the software calibration (and 31.6 µm before software calibration), which was acceptable for targeting the same region in cortex.

During a recording, advancing the pipette very close to the extracellular probe surface (< 30 µm) allowed direct detection of the 25 mV test pulse delivered by the juxtacellular amplifier on the extracellular array. The peak of this test pulse was largest on the targeted, and thus nearest, electrode site, providing further validation of our setup positioning accuracy (see Movie 2 in http://www.physiology.org/doi/suppl/10.1152/jn.00103.2016/suppl_file/Movie_2.mp4).

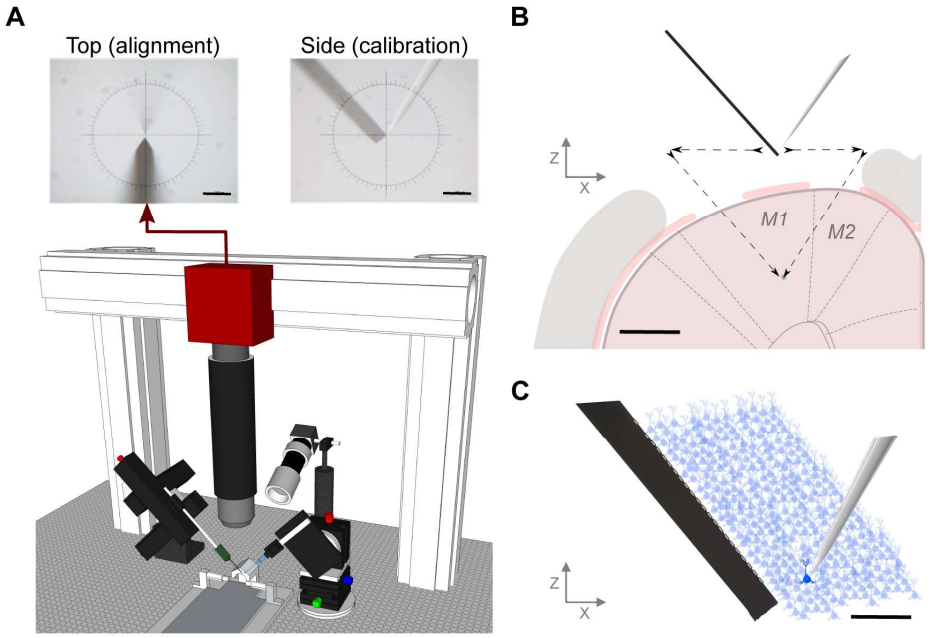

Figure 5.1 *In vivo* paired-recording setup: design and method. (a) Schematic of the dual-probe recording station. The PS micromanipulator drives the juxtacellular pipette and the IVM manipulator drives the extracellular polytrode. The setup includes a long working distance microscope assembled using optomechanical components mounted on a 3-axis motorized stage. The alignment image provides a high-resolution view from above the stereotactic frame, upper left, however a side-view can also be obtained for calibration purposes, upper right (scale bar = 100 µm); (b) Schematic of a coronal view [reproduced from Paxinos & Watson, 2007 with permission] of the craniotomy and durotomies with both probes positioned at the calibration point. The distance between durotomies, such that the probe tips meet at deep layers in cortex, was ~ 2 mm. The black arrows represent the motion path for both electrodes entering the brain (scale bar = 1 mm); (c) Diagram of simultaneous extracellular and juxtacellular paired-recording of the same neuron at a distance of 90 µm between the micropipette tip and the closest electrode on the extracellular polytrode (scale bar = 100 µm).

Paired juxtacellular-extracellular recording

Twenty-three neurons were recorded with a distance lower than 200 μm between the juxtacellular pipette tip and the closest extracellular electrode within the cortex of anesthetized rats. The precision aligned dual-probe setup could efficiently target neurons nearby the extracellular probe, and for each insertion of the pipette at least one paired-recording was obtained. Eleven animals were used to record all the pairs in this study (the full dataset is summarized in Table1 in http://www.physiology.org/doi/suppl/10.1152/jn.00103.2016/suppl_file/Table_1.xlsx).
However, with practice, it was possible to insert the juxtacellular pipette several times at different locations (max 4) and to record many neurons (max 6) along a single track.
The juxtacellular pipette had a long thin taper to minimize tissue displacement during penetration and promote longer stable recordings (Herfst et al., 2012) (Figure 5.2a). As the juxtacellular electrode was advanced through the brain, several neurons were encountered at different locations along the motion path and, consequently, at different distances from the extracellular polytrodes. Figure 5.2b illustrates the large juxtacellular (peak-to-peak ~4 mV) signal recorded from a neuron encountered at a distance of 51.0 ± 10.5 μm between the micropipette tip and the closest extracellular electrode. The positive-before-negative biphasic waveform shape (Figure 5.2c) is indicative of a capacitively coupled cell-attached recording from a somatic/perisomatic located recording pipette (Herfst et al., 2012). However, for two paired-recordings in the dataset, the pipette recording exhibited the waveform of well isolated extracellular spike (negative-before-positive), likely due to incomplete contact between the membrane and pipette presenting lower peak-to-peak amplitudes (*2015_09_04_Pair 5.0* and *2015_09_03_Pair 9.0*).
Simultaneously an extracellular recording was made with the 32-channel probe illustrated in Figure 5.2d, allowing us to specifically characterize the extracellular signature of an action potential generated by the juxtacellular recorded neuron. The band-pass filtered extracellular traces, ordered according to the electrode's geometry, are presented in Figure 5.2e and correspond to the same time window of the juxtacellular recording (Figure 5.2b). A short time window (4 ms) extracted from the extracellular trace around each detected juxtacellular event (occurrence of the action potential positive peak) for one extracellular channel is shown in Figure 5.2f. Despite the low amplitude, a clear extracellular signature of the juxtacellular recorded neuron's spike can be recovered by averaging windows across multiple events. This juxtacellular triggered average (JTA) can be computed for all channels, allowing a high signal-to-noise estimate of the spatiotemporal distribution of the extracellular action potential. The JTA peak-to-peak

amplitude for each channel interpolated within the electrode site geometry, sometimes called "the cell footprint" (Delgado Ruz & Schultz, 2014), is shown in Figure 5.2g. The JTA waveforms for each channel are shown, arranged using the relative probe spacing in Figure 5.2h and overlaid in Figure 5.2i.

The example presented in Figure 5.2 is from one paired juxtacellular and extracellular recording. Several recordings were made in a similar manner and we next examined the variety of extracellular signatures obtained from different neurons at different positions relative to 32 and 128-channel dense polytrodes.

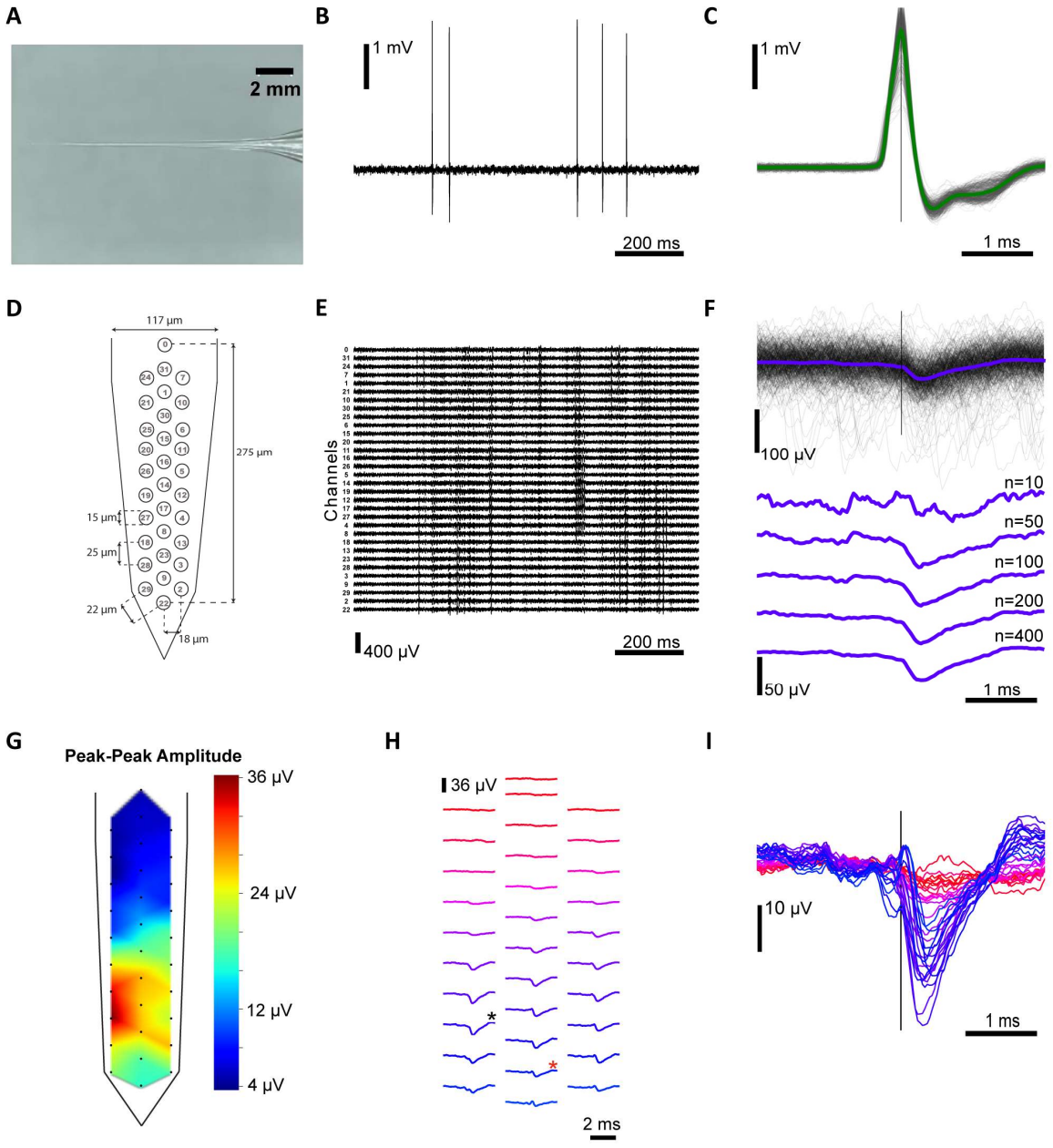

Figure 5.2 Paired extracellular and juxtacellular recordings from the same neuron. (a) Recording pipette with a long thin taper used for juxtacellular recordings with typical tip diameter of 1-4 μm and resistance of 3-7 MΩ; (b) Representative juxtacellular recording from a cell ~ 1256 μm in depth, 51 μm from the extracellular probe (*2014_10_17_Pair1.0),* with a firing rate of ~ 1 Hz; (c) The juxtacellular action potentials are overlaid, time-locked to the maximum positive peak, with the average spike waveform superimposed (n = 442 spikes); (d) Extracellular dense polytrode array with a span of 275 μm along the shank axis; the electrode channel number is represented at each site; (e) Representative extracellular recording that corresponds to the same time window as the above juxtacellular recording. Traces are ordered from upper to lower electrodes and channel numbers are indicated; (f) Extracellular waveforms, aligned on the juxtacellular spike peak, for a single channel (channel 18) and the juxtacellular triggered average (JTA) obtained by including an increasing number of juxtacellular events (n as indicated); (g) Spatial distribution of the amplitude for each channel's extracellular JTA waveform. The peak-to-peak amplitude within a time window (± 1 ms) surrounding the juxtacellular event was measured and the indicated color code was used to display and interpolate these amplitudes throughout the probe shaft; (h) The waveform averages for all the extracellular electrodes are spatially arranged. The channel with the highest peak-to-peak JTA amplitude (channel 18) is marked with a black asterisk and the closest channel (channel 9) is marked with a red asterisk; (i) Extracellular JTA time courses for each channel are overlaid and colored according to the scheme in (h).

Distance dependence of extracellular signal amplitude

Following a stable juxtacellular recording we were sometimes able to move the extracellular probe and obtain another recording configuration/distance for the same neuron. The relationship between extracellular signal amplitude and distance from the probe, for 35 such recording configurations, obtained from 23 neurons, is shown in Figure 5.3 (we also included in the dataset three paired-recordings with distances over 200 μm). Across all our paired-recordings, the distance between a neuron and the extracellular electrodes was the major factor determining the peak-to-peak extracellular signal amplitude.

Large peak-to-peak amplitudes were only observed for neurons within 50 μm from the nearest electrode, which is in accordance with previous measurements in hippocampus (Henze et al., 2000) and some theoretical models (Somogyvári, Cserpán, Ulbert, & Érdi, 2012). For neurons encountered within 50 to 150 μm of the probe surface, the magnitude of the neuron's extracellular signal ranged from 38 to 5 μV. All neurons encountered with a distance superior to 150 μm didn't show a canonical spike waveform, even after averaging, and we occasionally detected a small artefact (< 5 μV at 0 ms) that was similar for all channels and likely due to cross-talk between the extracellular and juxtacellular recording electronics. Nevertheless, we included these distant cells in the dataset since they could potentially be used to better understand the spike-LFP relationship (Berényi et al., 2014; Lewis, Bosman, & Fries, 2015).

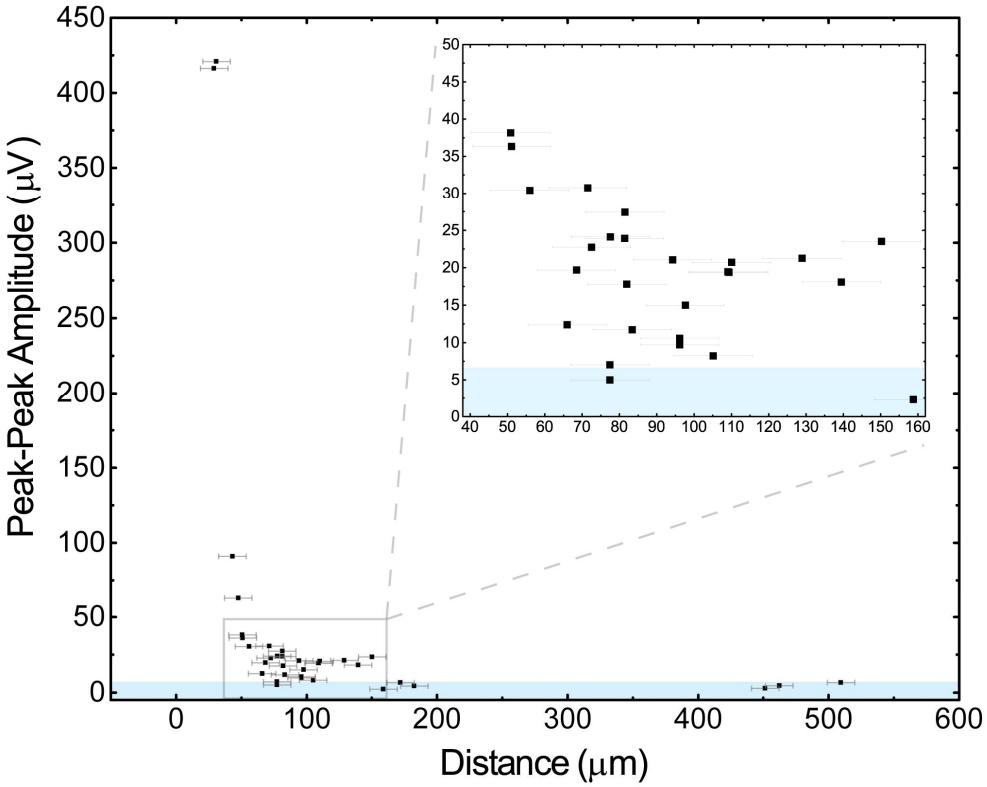

Figure 5.3 Distance dependence of extracellular signal amplitude. The maximum peak-to-peak amplitude of the JTAs (± 1 ms of the alignment time) across all extracellular channels for each paired-recording vs. the distance between the closest extracellular electrode and the juxtacellular pipette tip. Horizontal error bars report uncertainty in position estimate (± 10.5 μm). The light blue shaded region indicates a 5 μV threshold for excluding possible cross-talk electrical artifacts between the extra- and juxtacellular recording electronics.

Detection of the juxtacellular spikes on the extracellular probe

The first step in the analysis of extracellular data is the identification of discrete spike events (Hazan et al., 2006). Therefore, in order to use paired-recordings to evaluate algorithms for assigning these extracellular events to clusters belonging to distinct neurons (i.e., spike sorting), one must be able to detect the juxtacellular spike on the extracellular electrodes. We used a popular spike detection algorithm, SpikeDetekt, which extracts action potentials as spatiotemporally localized events (Rossant et al., 2016), to identify all spikes visible on our extracellular probe. SpikeDetekt uses a high threshold to detect spikes on a single channel and then a lower threshold to associate neighbouring channels (using a flood-fill algorithm) that sense the same spike. We used the same detection parameters for our entire dataset: third order Butterworth, forward-backward mode, band-pass filter (500-14,250 Hz) and strong and weak threshold levels of 4.5 and 2 times the standard deviation, respectively. The juxtacellular spike times were determined as the peaks of well-isolated threshold crossings (see Table 1 in

http://www.physiology.org/doi/suppl/10.1152/jn.00103.2016/suppl_file/Table_1.xlsx for the threshold values used for each individual paired-recording).

This spike detection process is illustrated in Figure 5.4a-c for a data segment containing the contribution of a neuron that was simultaneously recorded with the juxtacellular pipette (*2014_11_25_Pair3.0*). To compare the extracellularly detected event times with the spike times observed in the juxtacellular recording, we generated a peri-event time histogram (PETH) using all spike events found by SpikeDetekt on the extracellular channels aligned relative to each juxtacellular spike (Figure 5.4d and e). In some paired-recordings, these PETHs reveal a high probability of spike co-occurrence at 0 ms, indicating that the juxtacellular neuron's spike is being found by SpikeDetekt. The count value in the PETH 0 ms bin for the recorded pair in Figure 5.4d (*2014_11_25_Pair3.0*, channel 18) suggests that all the juxtacellular spikes were found, but that this bin also includes detections of coincident spiking events occurring in the background neuronal activity (386 detected, 348 actual found in the juxtacellular recording). These false positives could potentially be distinguished through manual sorting. In contrast, the PETH 0 ms bin for the pair in Figure 5.4e (*2014_ 03_26_Pair2.0*, channel 9) indicates that only 23% of the total number of juxtacellular spikes were detected (35 detected, 150 actual found in the juxtacellular recording), some of which are likely to also reflect coincident background events. We note that a larger number of putative juxta spikes could be recovered in this recording by reducing the high threshold level used by SpikeDetekt, but this would also include more background events and likely complicate subsequent sorting. The two examples in Figure 5.4 thus highlight both an "easy" and "hard" case for spike sorting algorithms.

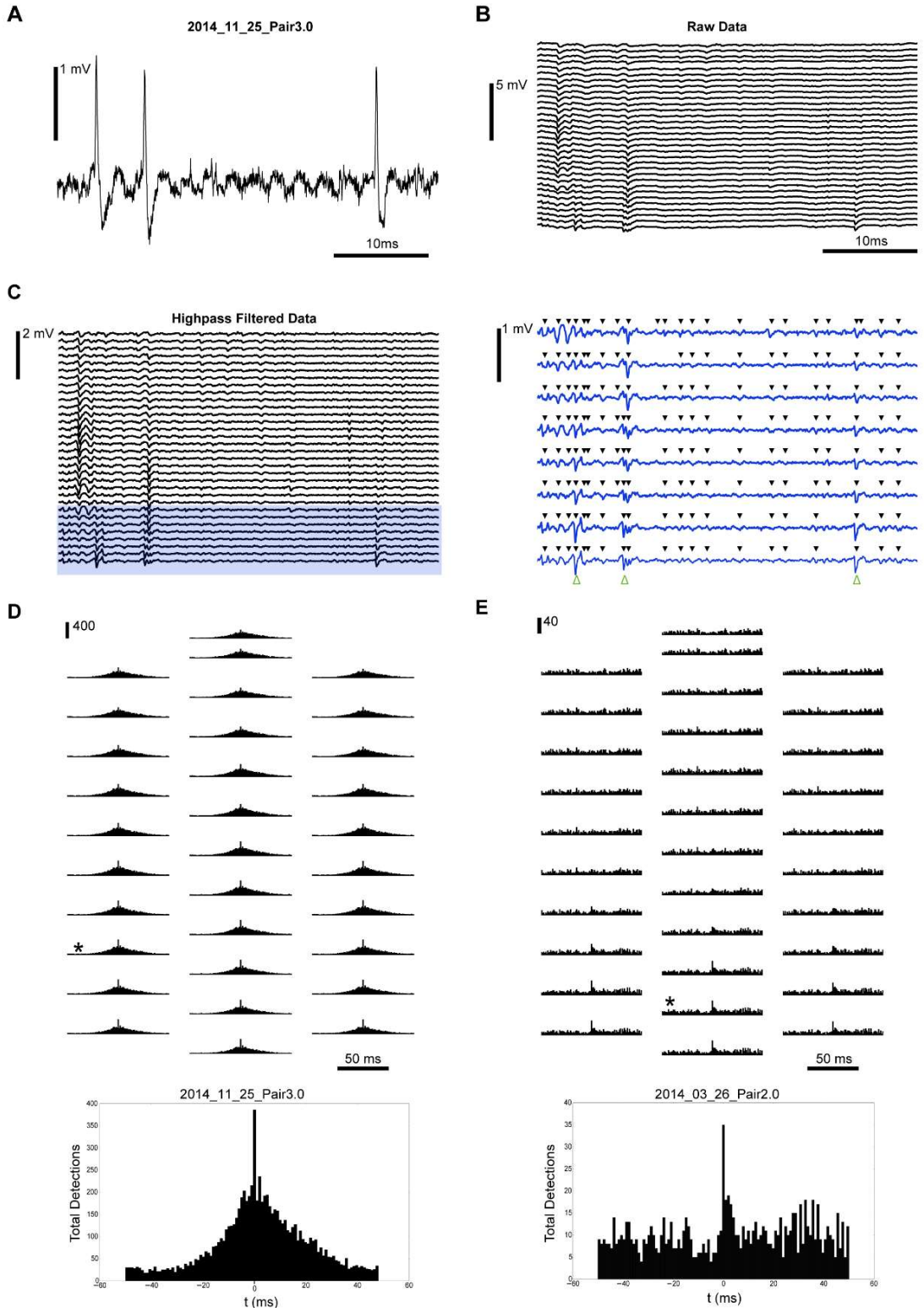

Figure 5.4 Extracellular detection of the juxtacellular neuron's action potentials. (a) Representative juxtacellular recording and (b) wide-band (0.1-7,500 kHz) signal recorded simultaneously with a 32-channel silicon polytrode; (c) On the highpass filtered extracellular data is visible the occurrence of temporally overlapping spikes on separated electrodes. The highlighted traces are expanded in the right panel and include black arrows to indicate all spikes identified by SpikeDetekt using standard thresholds and green arrows to indicate the time of juxtacellular spikes; (d) Peri-event time histograms of the extracellular spike events found by SpikeDetekt, relative to the juxtacellular spike times in 1 ms bins centered at 0 ms, are shown for each electrode channel at their relative position on the extracellular probe. The channel with the largest peak in the bin at 0 (± 0.5 ms from the juxtacellular event) is indicated by asterisk and expanded at bottom; (e) The same presentation as in (d), but for a neuron with a smaller extracellular action potential.

Spatiotemporal structure of extracellular signatures

Neurons near the polytrode surface exhibited a rich diversity of action potential waveforms (amplitude and dynamics) spread across multiple electrode sites (Figure 5.6 and Movie 3 and 4 in http://www.physiology.org/doi/suppl/10.1152/jn.00103.2016). This spatiotemporal structure will not only provide additional information for improving spike detection and sorting procedures, but may also reveal specific contributions from different parts of the neural membrane to this extracellular signature. For example, in Figure 5.5c, the first negative peak (blue trace) in the extracellular potential is hypothesized to arise from currents in the distal axon initial segment (Hu et al., 2009; Shu, Duque, Yu, Haider, & McCormick, 2007) and the later peaks (purple and red traces) might then be due to the backpropagation to soma and dendrites (Buzsáki et al., 1998).

The propagation velocity, estimated from the distance of the recording sites and the delay between the negative peaks (blue and red traces in Figure 5.5c) was ~ 0.55 m/s, which is in agreement with the value found in the literature for backpropagation of action potentials in cortical pyramidal cells, 0.67 ± 0.11 m/s (Buzsáki et al., 1998). Another example of complex structure in the extracellular signature is seen in Figure 5.5e, in this case the primary signal is localized to a small region of electrodes and varies greatly between neighbouring sites, which are separated by only 2.5 μm. These examples, and others in our dataset, clearly suggest that the amount of useful spatiotemporal information captured by dense large-scale neural recording devices is promising (Buzsáki, 2004), not only for improving algorithms that detect and sort events, but also to identify cell types based on the morphology suggested by their extracellular signature.

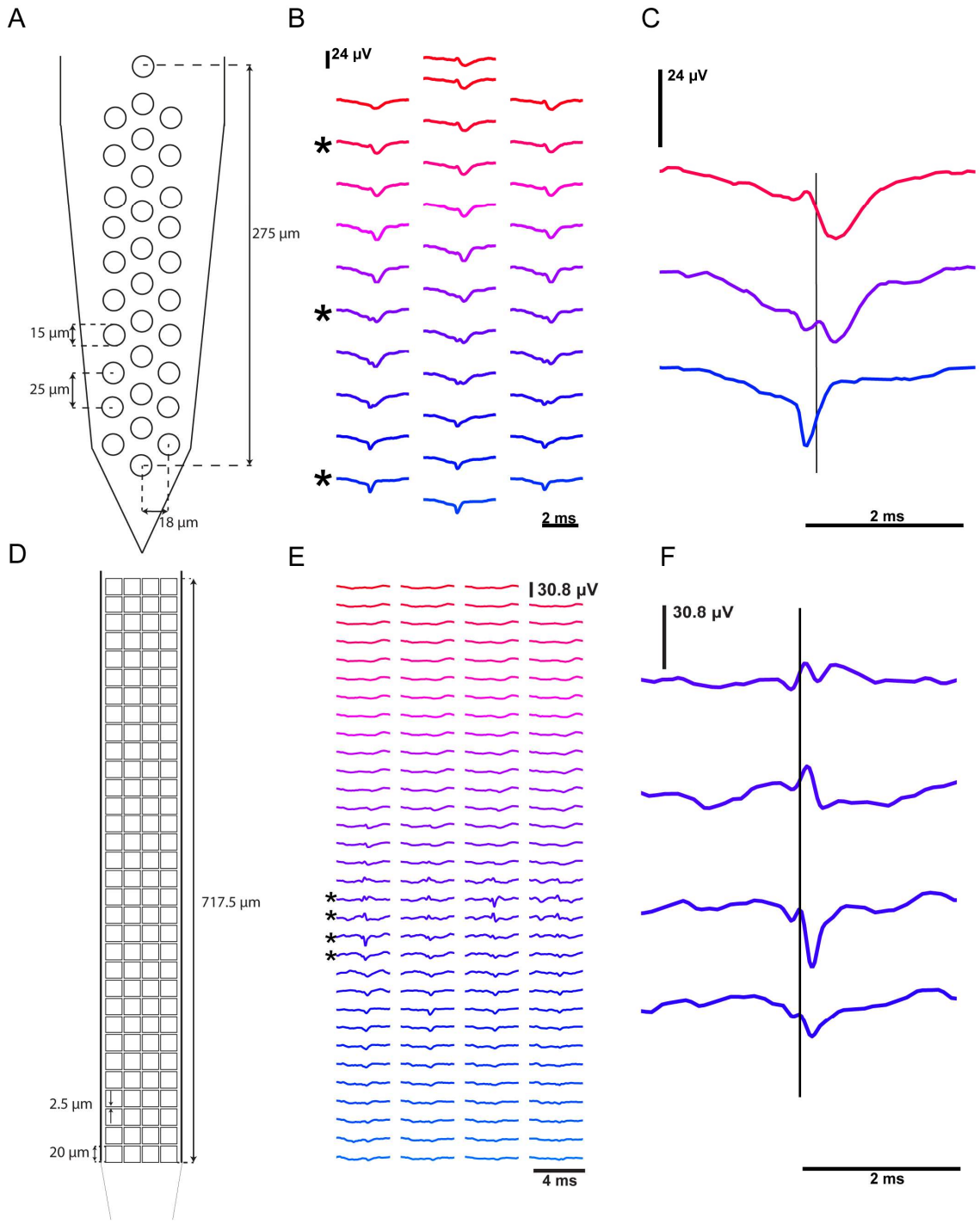

Figure *5.5* Spatiotemporal structure of extracellular signatures. (a) The geometry and dimensions of the 32-channel electrode array; (b) The JTA waveforms (*2014_11_25_Pair1.1*) for all the extracellular electrodes are spatially arranged according to the probe geometry; (c) Expanded comparison of the JTA waveforms for the indicated electrodes with a line denoting the peak time of the juxtacellular spike; (d-f) Similar presentation as (a-c) for one 128-channel polytrode pair example (*2015_09_04_Pair5.0*).

5.4 Discussion

In the present study, our dual-recording setup allowed precise targeting of both an extracellular probe and a juxtacellular pipette to the same position in cortex. The setup is low-cost and easily implemented by any electrophysiology laboratory with two motorized (servo/stepper) micromanipulators. We hope that our description will instigate the collection of such critical cross-validation data from the forthcoming deluge of novel neural recording devices.

Dataset for cross-validating polytrodes and spike detection/sorting algorithms

A summary of the current cross-validation dataset is presented in Figure 5.6. It includes twenty juxta-extracellular pairs recorded with both 32 and 128-channel polytrodes, at a range of inter-probe distances and depths in cortex (800 to 1800 μm from the pial surface). Future experiments, which use cell-attached labelling to anatomically reconstruct the juxtacellular neuron following a paired-recording, are now being pursued to extend this validation dataset. However, the existing dataset already includes a useful number of cross-validation examples: nearby cells with large extracellular action potentials, which will provide "ground truth" data for evaluating current spike detection and sorting algorithms, as well as more challenging intermediate cells, for which new algorithms, specifically optimized to use the additional information available to dense silicon polytrodes, may be able to recover. The full dataset, as well as probe maps and analysis code, is available online (http://www.kampff-lab.org/validating-electrodes/) and summarized in Table1, http://www.physiology.org/doi/suppl/10.1152/jn.00103.2016/suppl_file/Table_1.xlsx.

Are we missing neurons with extracellular recording?

An apparent discrepancy in the number of neurons that are reported to be active with optical (~50 %) versus electrical (< 10 %) recording techniques has prompted a number of researches to ask whether extracellular recording is "missing something" (Buzsáki, 2004; Shoham et al., 2006). Many explanations have been proposed (e.g., extracellular recording and sorting methods are biased to highly active neurons, some neuron types have weak or more localized extracellular signatures, etc.) yet estimating how many neurons an electrode should detect depends critically on knowing the volume of neural tissue to which an electrode is sensitive (i.e., from how far away can a neuron's spike be detected?).

The literature is rather inconsistent, but there are reports of recording neurons extracellularly (> 50 µV) from more than 100 µm away (Du et al., 2011; Henze & Buzsáki, 2007), while others suggest, based on modeling (Delgado Ruz & Schultz, 2014; Gray et al., 1995; Shoham et al., 2006; Somogyvári et al., 2012) and "ground truth" measurements (Anastassiou et al., 2015; Henze et al., 2000), that the limit is in fact closer to ~ 50 µm. Our data is consistent with the latter estimates (the maximum distance at which we observed a large peak-to-peak amplitude spike was only 48 µm) but also suggests a possible explanation for these discrepant views.

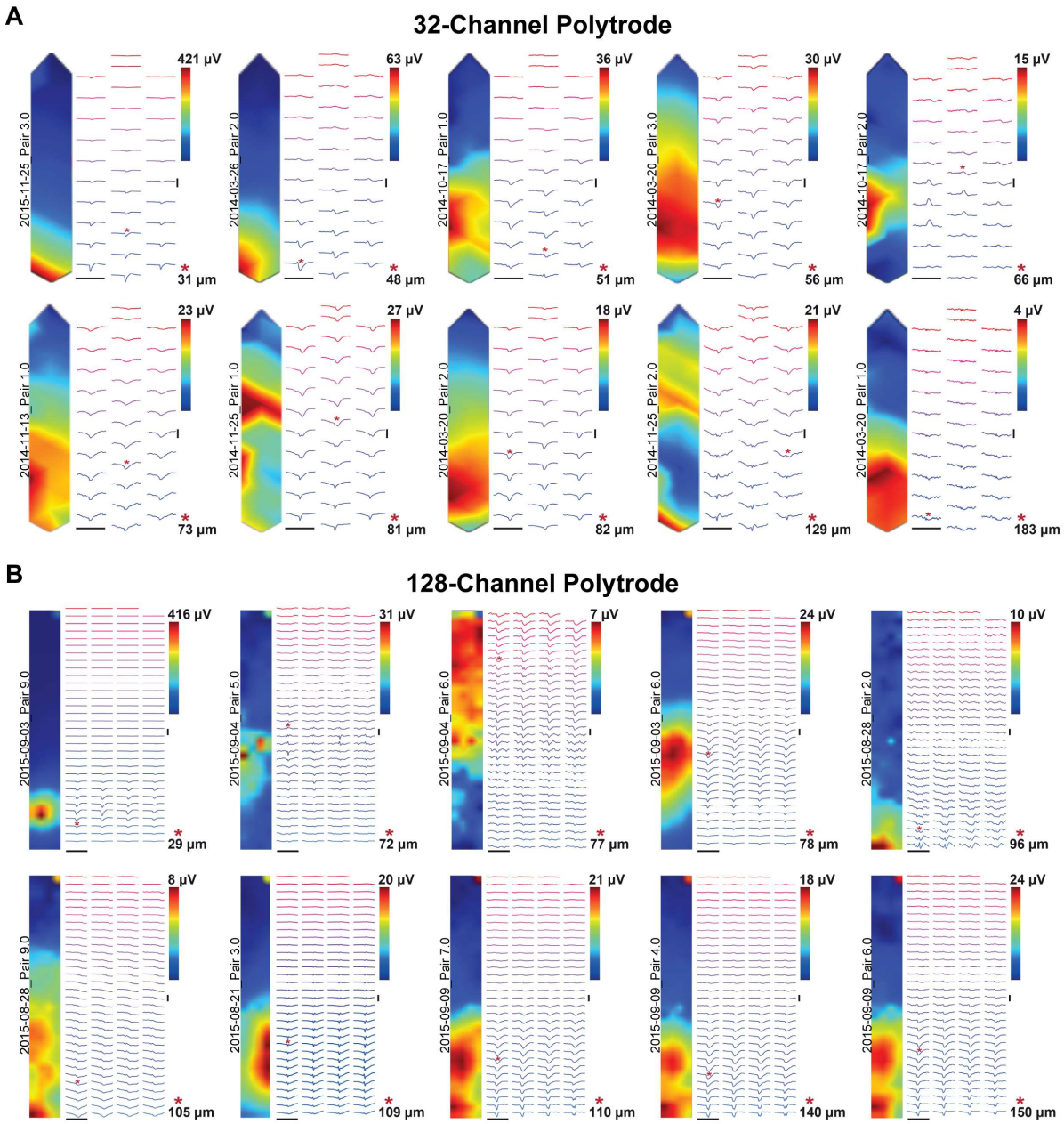

Figure 5.6 Dataset for validating spike detection and sorting algorithms for dense polytrodes. (a) Spatial distribution of the peak-to-peak amplitude within a time window (± 1 ms) surrounding the juxtacellular event and the indicated color code was used to display and interpolate these amplitudes throughout the 32-channel probe shaft. In addition, the extracellular JTA waveforms for all the extracellular electrodes are spatially arranged; (b) The same presentation as in (a) for paired-recordings with the 128-channel probe.

We propose that when an extracellular probe insertion is aligned with the axis of a pyramidal neuron's apical dendrite (or any neuron with an elongated morphology), then its EAP will be visible over a large distance, roughly matching the extent that the cell's dendritic arbor passes nearby the probe (Buzsáki et al., 1998). However, as the probe is positioned further away laterally from the neuron soma (perpendicular to the major axis of the neuron) then the EAP amplitude falls off steeply. All our recordings used an extracellular array that was inserted parallel to the apical dendrites of cortical pyramidal neurons (Figure 5.1b) and perpendicular to the cortical *laminae*. Therefore, if we were juxtacellularly recording from a pyramidal neuron whose soma was nearby the electrode surface and whose apical dendrite was aligned with the probe surface, then we would expect to detect a strong EAP across a large portion of the electrode surface, albeit with varying temporal waveforms (Figure 5.5b and Figure 5.6). However, if we juxtacellularly record from neurons whose soma are further from the probe surface, the size of the EAP on the probe surface will decrease rapidly (Figure 5.3). This interpretation can explain why one neuron might occasionally be detected over hundreds of microns (i.e., that neuron's morphology happened to be aligned with the probe/insertion track), but still supports the conclusion that an extracellular electrode is primarily sensitive to neurons (and their processes) within a 50 μm radius. Given this limited sensitivity range, are we still missing neurons? Based on cellular density estimates for cortex (40,000 to 60,000 neurons per mm^3 (DeFelipe et al., 2003)), and the half-spherical volume in front of a polytrode electrode, we would expect each site to be sensitive to approximately 10-15 neurons. These estimates are consistent with reported results for dense silicon polytrodes in cortex (Blanche, 2005). Our data thus suggests that there may not be a "dark neuron" problem, but rather that extracellular electrodes are sensitive to a much smaller volume than is sometimes proposed. However, much more data, from different brain regions containing diverse cell types, will be required to resolve this critical issue. We propose that our new dual-recording method will make gathering such important validation data much, much easier.

Chapter 6. General Conclusion

Extracellular microelectrodes have been widely used to measure neuronal activity *in vivo*, yet many questions about the limitations and the capabilities of this technique remain unanswered. This work was an attempt to answer some of the major questions surrounding extracellular recording and help researchers take full advantage of this seminal technique.

In Chapter 2 we synthesised our current understanding of extracellular recording. Through this chapter, the factors that govern the efficiency of signal transfer from the neuronal activity into digital recorded voltages were presented. Extracellular recordings are an imperfect representation of the underlying neuronal activity. What does a microelectrode detect when it is inside the brain? A microelectrode in the extracellular space, where the neuronal density is high, detects signals from multiple neurons at a millisecond time scale together with noise. The activity of a neuron generates a stereotypical temporal deflection of the potential, known as an action potential or spike. What contributes to the amplitude of the action potential observed as well as the background noise?

In Chapter 3, the effect of the electrode impedance on spike amplitude and background noise was discussed. Currently, there are conflicting views about the impact of impedance on the spikes recording. We have quantified the effect of impedance and we found that if the proper recording system is used, the impedance of a microelectrode, within the range typical of standard polytrodes (~ 0.1-2 MΩ), does not significantly affect spike amplitude and background noise, and therefore spike sorting. We believe that historically, impedance, which is more easily measured, was often used as a proxy to describe the surface area of an electrode. When researchers say that one may need an electrode with high-impedance to isolate neurons, this statement is possibly correlated with the electrode size (i.e., smaller electrodes record fewer neurons). Moreover, the thermal noise, described in several works as the main contributor to the background noise, is also highly correlated with the electrode impedance. Using electrodes from commercial polytrodes (15 µm diameter), the average noise levels measured *in vivo* for non-coated (~ 1 MΩ) and coated electrodes (~ 100 kΩ) ranged from 8.4 to 15.4 µV and from 5.8 to 14.8 µV, respectively. We verified that the thermal noise was obscured by the much larger biological noise or it was insignificant for the detection of spikes. Additionally, our results revealed that the average peak-to-peak amplitude from 109 well-isolated single cells from 11 recordings were relatively independent of the microelectrode impedance (coated and non-coated

electrodes).

Our study enabled a systematic investigation of the effects of impedance on the spikes recording, by comparing the voltage signal measured from closely-spaced electrodes with 10-fold impedance difference, under multiple conditions (i.e., different cortical depths and firing rates). The dataset is available online for further dissemination by the community (http://www.kampff-lab.org). We thus propose that we stop worrying about impedance (as long as it stays well below the input impedance of your amplifier), and start focusing on materials for electrode-brain interface to reduce the foreign body reaction (Coelho, 2016). Usually, silicon probes have poor long-term recording performance due to the formation of a dense layer of inflammatory cells, astrocytes, and a distancing of neurons from the recording electrode (Bellamkonda, Pai, & Renaud, 2012b; Rivnay et al., 2017). Furthermore, coatings for neural probes can be 'smarter'. They can be enhanced to deliver drugs or to sense chemicals to study the biochemistry involved in neuronal function (Obien et al., 2015; Rivnay et al., 2017; Santos et al., 2014, 2016)

Besides improving the electrode-brain interface in chronic implants, increasing the number of electrodes in a single neural probe is advantageous for neuroscientists who want simultaneously monitor the activity of large numbers of well-isolated neurons.

In Chapter 4 we reported an ultra-high density CMOS-based scanning probe with 1344 electrodes and 12 reference channels arranged along 8.1 mm of a thin (100 μm) shaft, developed in collaboration with the NeuroSeeker consortium. The advantage of this technology is its capability of recording simultaneously from all the channels, which avoids selecting a subset of electrodes prior to the experiment (Jun et al., 2017). The transmission of data from 1356 electrodes occurs through a flexible and lightweight cable, since time division multiplexing is embedded within the shank, and filters, amplifiers and digitizers are integrated at the probe base. We demonstrated the possibility of simultaneous recording from all of the electrodes on the shank (1356 electrodes), such as when all the electrodes were active, the background noise value *in vivo* was less than 20 μV. Moreover, the size of the data obtained from these probes inevitably presents new challenges for data management, visualization and analysis. We presented new methods developed within NeuroSeeker for assessing data quality online and an offline data visualization tool for accelerating the manual spike sorting of individual neurons.

Certainly, CMOS scanning probes, an emerging technology unfortunately not commercially available, have high potential for future research. In our laboratory, preliminary experiments have shown the possibility of recording in behaving animals with this probe. The key advantages of these probes include the resolution of signal in space (i.e., capability to record a neuron at multiple electrodes simultaneously). Spatiotemporal information enables researchers to localize

and classify neurons (Delgado Ruz & Schultz, 2014; Fiscella et al., 2012; Frey, Egert, Heer, Hafizovic, & Hierlemann, 2009). Furthermore, the development of fully automatic spike sorting becomes easier because 'electrode drift' (i.e., the physical movement of the electrode relative to the brain (Harris et al., 2016)) can be more easily tracked and corrected with software. Moreover, another advantage of using these probes is the capacity of recording neurons from several brain regions what can facilitate the understanding of the neural communication dynamics (Chen, Li, Daie, & Svoboda, 2017; Fiscella et al., 2012; Petreanu et al., 2012). Additionally, since we can read the activity of a very large number of neurons at once, we can characterize the brain in more naturalistic behavioural paradigms, capturing situations that arise only once or very few times, instead of relying on averaging over many trials, and also use less animals (Battaglia & Schnitzer, 2015).

What is next for this seminal technique? What must be done to achieve the full potential of large-scale neuronal recordings? One path is to continuously improve the physical design of neural probes (e.g., higher electrode spatial resolution and more parallel readouts). Increasing recording electrode density can potentially facilitate spike sorting. How small and closely-packed can we fabricated recording electrodes? A probe containing electrodes with a sub-cellular dimensions was used to collect a dataset suitable for exploring optimal electrode configurations specifically tailored to different brain regions and/or cell types.

Another approach, in addition to the physical design choices, is to enhance the processing methods to easily extract meaningful information from recordings in a short period of time. Currently, spike sorting algorithms require manual processing that limits their scalability. How can we validate probes with different electrode materials/configurations and different sorting algorithms?

In Chapter 5 we described a procedure for precisely aligning two probes for *in vivo* paired-recordings such that the spiking activity of a single neuron is monitored with both a dense extracellular silicon polytrode and a juxtacellular micro-pipette. We gathered a dataset of paired-recordings, which is available online. The "ground truth" data, for which one knows exactly when a neuron in the vicinity of an extracellular probe generates an action potential, has been used for several groups to validate and quantify the performance of new algorithms to automatically detect/sort single-units. Furthermore, our novel targeting system is now being used in the laboratory to expand the cross/validation dataset.

To conclude, this work has shown that extracellular recording, the oldest technique to measure the neuronal activity, has made a big step towards the large-scale microelectrode recordings. And

now, probes with thousands of microelectrodes can be used to answer the question: 'How populations of neurons distributed across the brain coordinate their activity in relation to behavior? Additionally, the large datasets gathered across different brain regions trigger the debate about the analysis, interpretation of results and theoretical frameworks (Dotson, Goodell, Salazar, Hoffman, & Gray, 2015; Harris et al., 2016; Obien et al., 2015). Finally, we believe that engineers and neuroscientists, can take full advantage of this important technique by understanding the limitations of extracellular recordings and how these affect signal and, consequently analysis.

Bibliography

Adrian, E. D. (1928). *The Basis of Sensation The action of the sense organs*. New York: W.W. Norton and Company, Inc.

Aggarwal, V., Mollazadeh, M., Davidson, A. G., Schieber, M. H., & Thakor, N. V. (2013). State-based decoding of hand and finger kinematics using neuronal ensemble and LFP activity during dexterous reach-to-grasp movements. *Journal of Neurophysiology*, *109*(12), 3067–3081. http://doi.org/10.1152/jn.01038.2011

Alivisatos, A. P., Andrews, A. M., Boyden, E. S., Chun, M., Church, G. M., Deisseroth, K., ... Zhuang, X. (2013). Nanotools for neuroscience and brain activity mapping. *ACS Nano*, *7*(3), 1850–66. http://doi.org/10.1021/nn4012847

Anastassiou, C. A., Perin, R., Buzsáki, G., Markram, H., & Koch, C. (2015). Cell type- and activity-dependent extracellular correlates of intracellular spiking. *Journal of Neurophysiology*, *114*(1), 608–23. http://doi.org/10.1152/jn.00628.2014

Ansaldo, A., Castagnola, E., Maggiolini, E., Fadiga, L., & Ricci, D. (2011). Superior electrochemical performance of carbon nanotubes directly grown on sharp microelectrodes. *ACS Nano*, *5*(3), 2206–14. http://doi.org/10.1021/nn103445d

Aregueta-Robles, U. A., Woolley, A. J., Poole-Warren, L. A., Lovell, N. H., & Green, R. A. (2014). Organic electrode coatings for next-generation neural interfaces. *Frontiers in Neuroengineering*, *7*(May), 15. http://doi.org/10.3389/fneng.2014.00015

Azevedo, F. A. C., Carvalho, L. R. B., Grinberg, L. T., Farfel, J. M., Ferretti, R. E. L., Leite, R. E. P., ... Herculano-Houzel, S. (2009). Equal numbers of neuronal and nonneuronal cells make the human brain an isometrically scaled-up primate brain. *The Journal of Comparative Neurology*, *513*(5), 532–541. http://doi.org/10.1002/cne.21974

Baião, P. (2014). Nanostructuring silicon probes via electrodeposition : Characterization of electrode coatings for acute in vivo. Retrieved from https://run.unl.pt/handle/10362/14666

Baranauskas, G., Maggiolini, E., Castagnola, E., Ansaldo, A., Mazzoni, A., Angotzi, G. N., ... Fadiga, L. (2011). Carbon nanotube composite coating of neural microelectrodes preferentially improves the multiunit signal-to-noise ratio. *Journal of Neural Engineering*, *8*(6), 66013. http://doi.org/10.1088/1741-2560/8/6/066013

Bard, A. J., & Faulkner, L. R. (2001). *Electrochemical methods Fundamentals and Applications*. *Molecular Biology* (Second, Vol. 8). John Wiley & Sons, Inc. http://doi.org/10.1016/B978-0-08-098353-0.00003-8

Barthó, P., Hirase, H., Monconduit, L., Zugaro, M., Harris, K. D., & Buzsáki, G. (2004). Characterization of neocortical principal cells and interneurons by network interactions and extracellular features. *Journal of Neurophysiology*, *92*(1), 600–608. http://doi.org/10.1152/jn.01170.2003

Battaglia, F. P., & Schnitzer, M. J. (2015). Editorial overview: Large-scale recording technology: Scaling up neuroscience. *Current Opinion in Neurobiology*, *32*, iv–vi. http://doi.org/10.1016/j.conb.2015.03.002

Bellamkonda, R. V., Pai, S. B., & Renaud, P. (2012a). Materials for neural interfaces. *MRS Bulletin*, *37*(6), 557–561. http://doi.org/10.1557/mrs.2012.122

Bellamkonda, R. V., Pai, S. B., & Renaud, P. (2012b). Materials for neural interfaces. *MRS Bulletin*, *37*(6), 557–561. http://doi.org/10.1557/mrs.2012.122

Berényi, A., Somogyvári, Z., Nagy, A. J., Roux, L., Long, J. D., Fujisawa, S., … Buzsáki, G. (2014). Large-scale, high-density (up to 512 channels) recording of local circuits in behaving animals. *Journal of Neurophysiology*, *111*(5), 1132–49. http://doi.org/10.1152/jn.00785.2013

Blanche, T. J. (2005). Polytrodes: High-Density Silicon Electrode Arrays for Large-Scale Multiunit Recording. *Journal of Neurophysiology*, *93*(5), 2987–3000. http://doi.org/10.1152/jn.01023.2004

Bonsai. (2017). Bonsai. Retrieved October 31, 2017, from http://bonsai-rx.org/

Brand, O. (2005). *Fabrication Technology. Advanced Micro and Nanosystems. Vol. 2. CMOS – MEMS* (Vol. 2). Retrieved from https://application.wiley-vch.de/books/sample/3527310800_c01.pdf

Buzsáki, G. (2004). Large-scale recording of neuronal ensembles. *Nature Neuroscience*, *7*(5), 446–451. http://doi.org/10.1038/nn1233

Buzsáki, G., Anastassiou, C. a, & Koch, C. (2012). The origin of extracellular fields and currents--EEG, ECoG, LFP and spikes. *Nature Reviews. Neuroscience*, *13*(6), 407–20. http://doi.org/10.1038/nrn3241

Buzsáki, G., Kandel, A., Kipke, D. R., Shain, W., Fetz, E., Henderson, J. M., … Panzeri, S. (1998). Somadendritic Backpropagation of Action Potentials in Cortical Pyramidal Cells of the Awake Rat. *Journal of Neurophysiology*, (79), 1587–1591.

Buzsáki, G., Stark, E., Berényi, A., Khodagholy, D., Kipke, D. R., Yoon, E., & Wise, K. D. (2015). Tools for Probing Local Circuits: High-Density Silicon Probes Combined with Optogenetics. *Neuron*, *86*(1), 92–105. http://doi.org/10.1016/j.neuron.2015.01.028

Camuñas-Mesa, L. A., & Quiroga, R. Q. (2013). A Detailed and Fast Model of Extracellular

Recordings. *Neural Computation*, *25*(5), 1191–1212. http://doi.org/10.1162/NECO_a_00433

Chapin, J. K. (2004). Using multi-neuron population recordings for neural prosthetics. *Nature Neuroscience*, *7*(5), 452–455. http://doi.org/10.1038/nn1234

Chen, S., & Allen, M. G. (2012). Extracellular matrix-based materials for neural interfacing. *MRS Bulletin*, *37*(6), 606–613. http://doi.org/10.1557/mrs.2012.120

Chen, T.-W., Li, N., Daie, K., & Svoboda, K. (2017). A Map of Anticipatory Activity in Mouse Motor Cortex. *Neuron*, *94*(4), 866–879.e4. http://doi.org/10.1016/j.neuron.2017.05.005

Chorev, E., & Brecht, M. (2012). In vivo dual intra- and extracellular recordings suggest bidirectional coupling between CA1 pyramidal neurons. *Journal of Neurophysiology*, *108*(6), 1584–93. http://doi.org/10.1152/jn.01115.2011

Chung, J. E., Magland, J. F., Barnett, A. H., Tolosa, V. M., Tooker, A. C., Lee, K. Y., … Greengard, L. F. (2017). A Fully Automated Approach to Spike Sorting. *Neuron*, *95*(6), 1381–1394.e6. http://doi.org/10.1016/j.neuron.2017.08.030

Chung, T., Wang, J. Q., Wang, J., Cao, B., Li, Y., & Pang, S. W. (2015). Electrode modifications to lower electrode impedance and improve neural signal recording sensitivity. *Journal of Neural Engineering*, *12*(5), 56018. http://doi.org/10.1088/1741-2560/12/5/056018

Churchland, M. M., Cunningham, J. P., Kaufman, M. T., Foster, J. D., Nuyujukian, P., Ryu, S. I., & Shenoy, K. V. (2012). Neural population dynamics during reaching. *Nature*, *487*. http://doi.org/10.1038/nature11129

Clement, E. A., Richard, A., Thwaites, M., Ailon, J., Peters, S., & Dickson, C. T. (2008). Cyclic and Sleep-Like Spontaneous Alternations of Brain State Under Urethane Anaesthesia. *PLoS ONE*, *3*(4), e2004. http://doi.org/10.1371/journal.pone.0002004

Coelho, N. M. T. (2016). *Improving silicon probe performance through layer-by-layer coating*. Retrieved from https://run.unl.pt/handle/10362/16388

Cogan, S. F. (2008). Neural Stimulation and Recording Electrodes. *Annual Review of Biomedical Engineering*, *10*(1), 275–309. http://doi.org/10.1146/annurev.bioeng.10.061807.160518

Csicsvari, J., Henze, D. a, Jamieson, B., Harris, K. D., Sirota, A., Barthó, P., … Buzsáki, G. (2003). Massively parallel recording of unit and local field potentials with silicon-based electrodes. *Journal of Neurophysiology*, *90*(2), 1314–23. http://doi.org/10.1152/jn.00116.2003

Cui, X., Lee, V. A., Raphael, Y., Wiler, J. A., Hetke, J. F., Anderson, D. J., & Martin, D. C. (2001). Surface modification of neural recording electrodes with conducting

polymer/biomolecule blends. *Journal of Biomedical Materials Research*, *56*(2), 261–72. Retrieved from http://www.ncbi.nlm.nih.gov/pubmed/11340598

Cui, X., & Martin, D. C. (2003). Fuzzy gold electrodes for lowering impedance and improving adhesion with electrodeposited conducting polymer. *Most*, *103*, 384–394.

DeFelipe, J., Alonso-Nanclares, L., & Arellano, J. I. (2003). Microstructure of the neocortex: comparative aspects. *Journal of Neurocytology*, *31*(3–5), 299–316. Retrieved from http://www.ncbi.nlm.nih.gov/pubmed/12815249

Delgado Ruz, I., & Schultz, S. R. (2014). Localising and classifying neurons from high density MEA recordings. *Journal of Neuroscience Methods*, *233*, 115–128. http://doi.org/10.1016/j.jneumeth.2014.05.037

Desai, S. A., Rolston, J. D., Guo, L., & Potter, S. M. (2010). Improving impedance of implantable microwire multi-electrode arrays by ultrasonic electroplating of durable platinum black. *Frontiers in Neuroengineering*, *3*(May), 5. http://doi.org/10.3389/fneng.2010.00005

Dimitriadis, G., Fransen, A. M. M., & Maris, E. (2014). Sensory and cognitive neurophysiology in rats, Part 1: Controlled tactile stimulation and micro-ECoG recordings in freely moving animals. *Journal of Neuroscience Methods*, *232*, 63–73. http://doi.org/10.1016/j.jneumeth.2014.05.001

Dimitriadis, G., Neto, J. P., & Kampff, A. R. (2016). T-SNE visualization of large-scale neural recordings. *bioRxiv*, 1–22. http://doi.org/10.1101/087395

Dombovári, B., Fiáth, R., Kerekes, B. P., Tóth, E., Wittner, L., Horváth, D., ... Ulbert, I. (2014). In vivo validation of the electronic depth control probes. *Biomedizinische Technik. Biomedical Engineering*, *59*(4), 283–9. http://doi.org/10.1515/bmt-2012-0102

Dotson, N. M., Goodell, B., Salazar, R. F., Hoffman, S. J., & Gray, C. M. (2015). Methods, caveats and the future of large-scale microelectrode recordings in the non-human primate. *Frontiers in Systems Neuroscience*, *9*, 149. http://doi.org/10.3389/fnsys.2015.00149

Drake, K. L., Wise, K. D., Farraye, J., Anderson, D. J., & BeMent, S. L. (1988). Performance of planar multisite microprobes in recording extracellular single-unit intracortical activity. *IEEE Transactions on Biomedical Engineering*, *35*(9), 719–732. http://doi.org/10.1109/10.7273

Du, J., Blanche, T. J., Harrison, R. R., Lester, H. A., & Masmanidis, S. C. (2011). Multiplexed, High Density Electrophysiology with Nanofabricated Neural Probes. *PLoS ONE*, *6*(10), e26204. http://doi.org/10.1371/journal.pone.0026204

Dyson, F. J. (2012). Is Science Mostly Driven by Ideas or by Tools? *Science*, *338*(6113), 1426–

1427. http://doi.org/10.1126/science.1232773

Eccles, J. C. (1973). *Understanding of the Brain*.

Einevoll, G. T., Kayser, C., Logothetis, N. K., & Panzeri, S. (2013). Modelling and analysis of local field potentials for studying the function of cortical circuits. *Nature Reviews. Neuroscience*, *14*(11), 770–85. http://doi.org/10.1038/nrn3599

Ferguson, J. E., Boldt, C., & Redish, A. D. (2009). Creating low-impedance tetrodes by electroplating with additives. *Sensors and Actuators A: Physical*, *156*(2), 388–393. http://doi.org/10.1016/j.sna.2009.10.001

Ferree, T. C., Luu, P., Russell, G. S., & Tucker, D. M. (2001). Scalp electrode impedance, infection risk, and EEG data quality. *Clinical Neurophysiology*, *112*(3), 536–544. http://doi.org/10.1016/S1388-2457(00)00533-2

Fiscella, M., Farrow, K., Jones, I. L., Jäckel, D., Müller, J., Frey, U., ... Hierlemann, A. (2012). Recording from defined populations of retinal ganglion cells using a high-density CMOS-integrated microelectrode array with real-time switchable electrode selection. *Journal of Neuroscience Methods*, *211*(1), 103–113. http://doi.org/10.1016/j.jneumeth.2012.08.017

Fischer, A. C., Forsberg, F., Lapisa, M., Bleiker, S. J., Stemme, G., Roxhed, N., & Niklaus, F. (2015). Integrating MEMS and ICs. *Microsystems & Nanoengineering*, *1*(April), 15005. http://doi.org/10.1038/micronano.2015.5

Fitzsimmons, N. A. (2009). Extracting kinematic parameters for monkey bipedal walking from cortical neuronal ensemble activity. *Frontiers in Integrative Neuroscience*, *3*, 3. http://doi.org/10.3389/neuro.07.003.2009

Focus on the neuroscience toolbox. (2016). *Nature Neuroscience*, *19*(9), 1117–1117. http://doi.org/10.1038/nn.4379

Franke, F., Jäckel, D., Dragas, J., Müller, J., Radivojevic, M., Bakkum, D., & Hierlemann, A. (2012). High-density microelectrode array recordings and real-time spike sorting for closed-loop experiments: an emerging technology to study neural plasticity. *Frontiers in Neural Circuits*, *6*(December), 105. http://doi.org/10.3389/fncir.2012.00105

Fraser, G. W., & Schwartz, A. B. (2012). Recording from the same neurons chronically in motor cortex. *Journal of Neurophysiology*, *107*(7), 1970–1978. http://doi.org/10.1152/jn.01012.2010

Frey, U., Egert, U., Heer, F., Hafizovic, S., & Hierlemann, A. (2009). Microelectronic system for high-resolution mapping of extracellular electric fields applied to brain slices. *Biosensors and Bioelectronics*, *24*(7), 2191–2198. http://doi.org/10.1016/j.bios.2008.11.028

Fujisawa, S., Amarasingham, A., Harrison, M. T., & Buzsáki, G. (2008). Behavior-dependent

short-term assembly dynamics in the medial prefrontal cortex. *Nature Neuroscience*, *11*(7), 823–833. http://doi.org/10.1038/nn.2134

Ganguly, K., & Carmena, J. M. (2009). Emergence of a Stable Cortical Map for Neuroprosthetic Control. *PLoS Biol*, *7*(7). Retrieved from http://journals.plos.org/plosbiology/article/file?id=10.1371/journal.pbio.1000153&type=printable

Gold, C., Henze, D. a, & Koch, C. (2007). Using extracellular action potential recordings to constrain compartmental models. *Journal of Computational Neuroscience*, *23*(1), 39–58. http://doi.org/10.1007/s10827-006-0018-2

Gold, C., Henze, D. a, Koch, C., & Buzsáki, G. (2006). On the origin of the extracellular action potential waveform: A modeling study. *Journal of Neurophysiology*, *95*(5), 3113–28. http://doi.org/10.1152/jn.00979.2005

Goris, R. L. T., Movshon, J. A., & Simoncelli, E. P. (2014). Partitioning neuronal variability. *Nature Neuroscience*, *17*(6), 858–865. http://doi.org/10.1038/nn.3711

Gray, C. M., Maldonado, P. E., Wilson, M., & McNaughton, B. (1995). Tetrodes markedly improve the reliability and yield of multiple single-unit isolation from multi-unit recordings in cat striate cortex. *Journal of Neuroscience Methods*, *63*(1–2), 43–54. http://doi.org/10.1016/0165-0270(95)00085-2

Green, R. A., Lovell, N. H., Wallace, G. G., & Poole-Warren, L. A. (2008). Conducting polymers for neural interfaces: Challenges in developing an effective long-term implant. *Biomaterials*, *29*(24–25), 3393–3399. http://doi.org/10.1016/j.biomaterials.2008.04.047

Hafting, T., Fyhn, M., Molden, S., Moser, M.-B., & Moser, E. I. (2005). Microstructure of a spatial map in the entorhinal cortex. *Nature*, *436*(7052), 801–806. http://doi.org/10.1038/nature03721

Harris, K. D., Henze, D. A., Csicsvari, J., Hirase, H., & Buzsaki, G. (2000). Accuracy of Tetrode Spike Separation as Determined by Simultaneous Intracellular and Extracellular Measurements. *J Neurophysiol*, *84*(1), 401–414. Retrieved from http://jn.physiology.org/content/84/1/401.long

Harris, K. D., Quiroga, R. Q., Freeman, J., & Smith, S. L. (2016). Improving data quality in neuronal population recordings. *Nature Neuroscience*, *19*(9), 1165–1174. http://doi.org/10.1038/nn.4365

Hassibi, A., Navid, R., Dutton, R. W., & Lee, T. H. (2004). Comprehensive study of noise processes in electrode electrolyte interfaces. *Journal of Applied Physics*, *96*(2), 1074–1082. http://doi.org/10.1063/1.1755429

Hatsopoulos, N. G., Xu, Q., & Amit, Y. (2007). Encoding of Movement Fragments in the Motor Cortex. *Journal of Neuroscience*, *27*(19).

Hatsopoulos, N., Joshi, J., & O'Leary, J. G. (2004). Decoding continuous and discrete motor behaviors using motor and premotor cortical ensembles. *Journal of Neurophysiology*, *92*(2), 1165–74. http://doi.org/10.1152/jn.01245.2003

Hazan, L., Zugaro, M., & Buzsáki, G. (2006). Klusters, NeuroScope, NDManager: a free software suite for neurophysiological data processing and visualization. *Journal of Neuroscience Methods*, *155*(2), 207–16. http://doi.org/10.1016/j.jneumeth.2006.01.017

Henze, D. A., Borhegyi, Z., Csicsvari, J., Mamiya, A., Harris, K. D., & Buzsáki, G. (2000). Intracellular features predicted by extracellular recordings in the hippocampus in vivo. *Journal of Neurophysiology*, *84*(1), 390–400. http://doi.org/84:390-400

Henze, D. A., & Buzsáki, G. (2007). Hilar mossy cells: functional identification and activity in vivo. *Progress in Brain Research*, *163*, 199–216. http://doi.org/10.1016/S0079-6123(07)63012-X

Herculano-Houzel, S. (2009). The human brain in numbers: a linearly scaled-up primate brain. *Frontiers in Human Neuroscience*, *3*(November), 31. http://doi.org/10.3389/neuro.09.031.2009

Herfst, L., Burgalossi, A., Haskic, K., Tukker, J. J., Schmidt, M., & Brecht, M. (2012). Friction-based stabilization of juxtacellular recordings in freely moving rats. *Journal of Neurophysiology*, *108*(2), 697–707. http://doi.org/10.1152/jn.00910.2011

Heuschkel, M. O., Fejtl, M., Raggenbass, M., Bertrand, D., & Renaud, P. (2002). A three-dimensional multi-electrode array for multi-site stimulation and recording in acute brain slices. *Journal of Neuroscience Methods*, *114*(2), 135–148. http://doi.org/10.1016/S0165-0270(01)00514-3

Hodgkin, A. L., & Huxley, A. F. (1939). Action Potentials Recorded from Inside a Nerve Fibre. *Nature*, *144*(3651), 710–711. http://doi.org/10.1038/144710a0

Hu, W., Tian, C., Li, T., Yang, M., Hou, H., & Shu, Y. (2009). Distinct contributions of Na(v)1.6 and Na(v)1.2 in action potential initiation and backpropagation. *Nature Neuroscience*, *12*(8), 996–1002. http://doi.org/10.1038/nn.2359

Hubel, D. H. (1957). Tungsten microelectrode for recording from single units. *Science*, *125*(3247), 549–550. http://doi.org/10.1126/science.125.3247.549

Hubel, D. H., & T. N. Wiesel. (1962). Receptive fields, binocular interaction and functional architecture in the cat's visual cortex. *Journal of Physiology*, 106–154. http://doi.org/10.1113/jphysiol.1962.sp006837

Ifft, P. J., Shokur, S., Li, Z., Lebedev, M. A., & Nicolelis, M. A. L. (2013). A Brain-Machine Interface Enables Bimanual Arm Movements in Monkeys. *Science Translational Medicine*, *5*(210), 210ra154-210ra154. http://doi.org/10.1126/scitranslmed.3006159

Intro to Intan Amplifier Chips | Intan Technologies. (2017). Retrieved June 21, 2017, from http://www.intantech.com/amplifier_intro.html

Jäckel, D., Bakkum, D. J., Russell, T. L., Müller, J., Radivojevic, M., Frey, U., ... Hierlemann, A. (2017). Combination of High-density Microelectrode Array and Patch Clamp Recordings to Enable Studies of Multisynaptic Integration. *Scientific Reports*, *7*(1), 978. http://doi.org/10.1038/s41598-017-00981-4

Jiang, X., Shen, S., Cadwell, C. R., Berens, P., Sinz, F., Ecker, A. S., ... Tolias, A. S. (2015). Principles of connectivity among morphologically defined cell types in adult neocortex. *Science*, *350*(6264), aac9462-aac9462. http://doi.org/10.1126/science.aac9462

Jog, M. S., Connolly, C. I., Kubota, Y., Iyengar, D. R., Garrido, L., Harlan, R., & Graybiel, a M. (2002). Tetrode technology: advances in implantable hardware, neuroimaging, and data analysis techniques. *Journal of Neuroscience Methods*, *117*(2), 141–52. Retrieved from http://www.ncbi.nlm.nih.gov/pubmed/12100979

Jorfi, M., Skousen, J. L., Weder, C., & Capadona, J. R. (2015). Progress towards biocompatible intracortical microelectrodes for neural interfacing applications. *Journal of Neural Engineering*, *12*(October), 11001. http://doi.org/10.1088/1741-2560/12/1/011001

Jun, J. J., Steinmetz, N. A., Siegle, J. H., Denman, D. J., Bauza, M., Barbarits, B., ... Harris, T. D. (2017). Fully integrated silicon probes for high-density recording of neural activity. *Nature*, *551*(7679), 232–236. http://doi.org/10.1038/nature24636

Jun, J., Mitelut, C., Lai, C., Gratiy, S. L., Anastassiou, C. A., & Harris, T. D. (2017). Real-time spike sorting platform for high-density extracellular probes with ground-truth validation and drift correction. *bioRxiv*, 1–29. http://doi.org/https://doi.org/10.1101/101030

Kandel, E. R., Schwartz, J. H., & Jessel, T. M. (2000). *Principles of Neural Science* (Fourth edi). McGraw-Hill.

Keefer, E. W., Botterman, B. R., Romero, M. I., Rossi, A. F., & Gross, G. W. (2008). Carbon nanotube coating improves neuronal recordings. *Nature Nanotechnology*, *3*(7), 434–9. http://doi.org/10.1038/nnano.2008.174

Kelly, R. C., Smith, M. A., Kass, R. E., & Lee, T. S. (2010). Local field potentials indicate network state and account for neuronal response variability. *Journal of Computational Neuroscience*, *29*(3), 567–579. http://doi.org/10.1007/s10827-009-0208-9

Kim, S., Bhandari, R., Klein, M., Negi, S., Rieth, L., Tathireddy, P., ... Solzbacher, F. (2009).

Integrated wireless neural interface based on the Utah electrode array. *Biomedical Microdevices*, *11*(2), 453–66. http://doi.org/10.1007/s10544-008-9251-y

Kim, S. Y., Kim, K.-M., Hoffman-Kim, D., Song, H.-K., & Palmore, G. T. R. (2011). Quantitative control of neuron adhesion at a neural interface using a conducting polymer composite with low electrical impedance. *ACS Applied Materials Interfaces*, *3*(1), 16–21. Retrieved from http://www.ncbi.nlm.nih.gov/pubmed/21142128

Kook, G., Lee, S., Lee, H., Cho, I.-J., & Lee, H. (2016). Neural Probes for Chronic Applications. *Micromachines*, *7*(10), 179. http://doi.org/10.3390/mi7100179

Kotov, N. A., Winter, J. O., Clements, I. P., Jan, E., Timko, B. P., Campidelli, S., ... Ballerini, L. (2009). Nanomaterials for Neural Interfaces. *Advanced Materials*, *21*(40), 3970–4004. http://doi.org/10.1002/adma.200801984

Kozai, T. D. Y., Catt, K., Du, Z., Na, K., Srivannavit, O., Haque, R. M., ... Cui, X. T. (2016). Chronic In Vivo Evaluation of PEDOT/CNT for Stable Neural Recordings. *IEEE Transactions on Bio-Medical Engineering*, *63*(1), 111–9. http://doi.org/10.1109/TBME.2015.2445713

Kozai, T. D. Y., Du, Z., Gugel, Z. V., Smith, M. A., Chase, S. M., Bodily, L. M., ... Cui, X. T. (2015). Comprehensive chronic laminar single-unit, multi-unit, and local field potential recording performance with planar single shank electrode arrays. *Journal of Neuroscience Methods*, *242*, 15–40. http://doi.org/10.1016/j.jneumeth.2014.12.010

Krioukov, D. (2014). Brain theory. *Frontiers in Computational Neuroscience*, *8*(October), 114. http://doi.org/10.3389/fncom.2014.00114

Lempka, S. F., Johnson, M. D., Barnett, D. W., Moffitt, M. A., Otto, K. J., Kipke, D. R., & McIntyre, C. C. (2006). Optimization of microelectrode design for cortical recording based on thermal noise considerations. *Conference Proceedings : ... Annual International Conference of the IEEE Engineering in Medicine and Biology Society. IEEE Engineering in Medicine and Biology Society. Annual Conference*, *1*, 3361–4. http://doi.org/10.1109/IEMBS.2006.259432

Lempka, S. F., Johnson, M. D., Moffitt, M. a, Otto, K. J., Kipke, D. R., & McIntyre, C. C. (2011). Theoretical analysis of intracortical microelectrode recordings. *Journal of Neural Engineering*, *8*(4), 45006. http://doi.org/10.1088/1741-2560/8/4/045006

Lempka, S. F., & McIntyre, C. C. (2013). Theoretical Analysis of the Local Field Potential in Deep Brain Stimulation Applications. *PLoS ONE*, *8*(3), e59839. http://doi.org/10.1371/journal.pone.0059839

Lewicki, M. (1998). A review of methods for spike sorting: the detection and classification of

neural action potentials. *Network: Computation in Neural Systems*, *9*(4), R53–R78. http://doi.org/10.1088/0954-898X/9/4/001

Lewis, C. M., Bosman, C. A., & Fries, P. (2015). Recording of brain activity across spatial scales. *Current Opinion in Neurobiology*, *32*, 68–77. http://doi.org/10.1016/j.conb.2014.12.007

Li, P. H., Gauthier, J. L., Schiff, M., Sher, A., Ahn, D., Field, G. D., ... Chichilnisky, E. J. (2015). Anatomical Identification of Extracellularly Recorded Cells in Large-Scale Multielectrode Recordings. *Journal of Neuroscience*, *35*(11), 4663–4675. http://doi.org/10.1523/JNEUROSCI.3675-14.2015

Lin, L., Osan, R., Shoham, S., Jin, W., Zuo, W., & Tsien, J. Z. (2005). Identification of network-level coding units for real-time representation of episodic experiences in the hippocampus. *Proceedings of the National Academy of Sciences of the United States of America*, *102*(17), 6125–30. http://doi.org/10.1073/pnas.0408233102

Lopes, G., Bonacchi, N., Frazão, J., Neto, J. P., Atallah, B. V, Soares, S., ... Kampff, A. R. (2015). Bonsai: an event-based framework for processing and controlling data streams. *Frontiers in Neuroinformatics*, *9*, 7. http://doi.org/10.3389/fninf.2015.00007

Lopez, C. M., Andrei, A., Mitra, S., Welkenhuysen, M., Eberle, W., Bartic, C., ... Gielen, G. (2013). An implantable 455-active-electrode 52-channel CMOS neural probe. In *2013 IEEE International Solid-State Circuits Conference Digest of Technical Papers* (pp. 288–289). IEEE. http://doi.org/10.1109/ISSCC.2013.6487738

Lopez, C. M., Mitra, S., Putzeys, J., Raducanu, B., Ballini, M., Andrei, A., ... Yazicioglu, R. F. (2016). A 966-electrode neural probe with 384 configurable channels in 0.13μm SOI CMOS. In *2016 IEEE International Solid-State Circuits Conference (ISSCC)* (Vol. 59, pp. 392–393). IEEE. http://doi.org/10.1109/ISSCC.2016.7418072

Ludwig, K. A., Langhals, N. B., Joseph, M. D., Richardson-Burns, S. M., Hendricks, J. L., & Kipke, D. R. (2011). Poly(3,4-ethylenedioxythiophene) (PEDOT) polymer coatings facilitate smaller neural recording electrodes. *Journal of Neural Engineering*, *8*(1), 14001. http://doi.org/10.1088/1741-2560/8/1/014001

Ludwig, K. A., Uram, J. D., Yang, J., Martin, D. C., & Kipke, D. R. (2006). Chronic neural recordings using silicon microelectrode arrays electrochemically deposited with a poly(3,4-ethylenedioxythiophene) (PEDOT) film. *Journal of Neural Engineering*, *3*(1), 59–70. http://doi.org/10.1088/1741-2560/3/1/007

Marblestone, A. H., Zamft, B. M., Maguire, Y. G., Shapiro, M. G., Cybulski, T. R., Glaser, J. I., ... Kording, K. P. (2013). Physical principles for scalable neural recording. *Frontiers in Computational Neuroscience*, *7*(October), 137. http://doi.org/10.3389/fncom.2013.00137

Markram, H., Muller, E., Ramaswamy, S., Reimann, M. W., Abdellah, M., Sanchez, C. A., ... Schürmann, F. (2015). Reconstruction and Simulation of Neocortical Microcircuitry. *Cell*, *163*(2), 456–492. http://doi.org/10.1016/j.cell.2015.09.029

Márton, G., Bakos, I., Fekete, Z., Ulbert, I., & Pongrácz, A. (2014). Durability of high surface area platinum deposits on microelectrode arrays for acute neural recordings. *Journal of Materials Science: Materials in Medicine*, *25*(3), 931–940. http://doi.org/10.1007/s10856-013-5114-z

McNaughton, B. L., O'Keefe, J., & Barnes, C. A. (1983). The stereotrode: A new technique for simultaneous isolation of several single units in the central nervous system from multiple unit records. *Journal of Neuroscience Methods*, *8*(4), 391–397. http://doi.org/10.1016/0165-0270(83)90097-3

Merrill, D. R., Bikson, M., & Jefferys, J. G. R. (2005). Electrical stimulation of excitable tissue: design of efficacious and safe protocols. *Journal of Neuroscience Methods*, *141*(2), 171–98. http://doi.org/10.1016/j.jneumeth.2004.10.020

Meyer, H. S., Wimmer, V. C., Oberlaender, M., de Kock, C. P. J., Sakmann, B., & Helmstaedter, M. (2010). Number and laminar distribution of neurons in a thalamocortical projection column of rat vibrissal cortex. *Cerebral Cortex (New York, N.Y. : 1991)*, *20*(10), 2277–86. http://doi.org/10.1093/cercor/bhq067

Michon, F., Aarts, A., Borghs, G., Bruce, M., & Fabian, K. (2014). Integration of silicon-based probes and micro-drive array for chronic recordings of large populations of neurons in behaving animals. In *GDR2904 Multielectrode systems and Signal processing for Neuroscience*.

Moffitt, M. A., & McIntyre, C. C. (2005). Model-based analysis of cortical recording with silicon microelectrodes. *Clinical Neurophysiology : Official Journal of the International Federation of Clinical Neurophysiology*, *116*(9), 2240–50. http://doi.org/10.1016/j.clinph.2005.05.018

Moore-Kochlacs, C. E. (2016). *Extracellular electrophysiology with close-packed recording sites: spike sorting and characterization*. Boston University.

Musa, R. (2011). *Design, fabrication and characterization of a neural probe for deep brain stimulation and recording.* Retrieved from https://lirias.kuleuven.be/handle/123456789/316157

Musa, S., Rand, D. R., Cott, D. J., Loo, J., Bartic, C., Eberle, W., ... Borghs, G. (2012). Bottom-up SiO 2 embedded carbon nanotube electrodes with superior performance for integration in implantable neural microsystems. *ACS Nano*, *6*(6), 4615–4628. http://doi.org/10.1021/nn201609u

Najafi, K., & Wise, K. D. (1986). An implantable multielectrode array with on-chip signal processing. *IEEE Journal of Solid-State Circuits*, *21*(6), 1035–1044. http://doi.org/10.1109/JSSC.1986.1052646

Najafi, K., Wise, K. D., & Mochizuki, T. (1985). A high-yield IC-compatible multichannel recording array. *IEEE Transactions on Electron Devices*, *32*(7), 1206–1211. http://doi.org/10.1109/T-ED.1985.22102

Nam, Y. (2012). Material considerations for in vitro neural interface technology. *MRS Bulletin*, *37*(6), 566–572. http://doi.org/10.1557/mrs.2012.98

Nelson, M. J., Bosch, C., Venance, L., & Pouget, P. (2013). Microscale Inhomogeneity of Brain Tissue Distorts Electrical Signal Propagation. *Journal of Neuroscience*, *33*(7), 2821–2827. http://doi.org/10.1523/JNEUROSCI.3502-12.2013

Nelson, M. J., Pouget, P., Nilsen, E. A., Patten, C. D., & Schall, J. D. (2008). Review of signal distortion through metal microelectrode recording circuits and filters. *Journal of Neuroscience Methods*, *169*(1), 141–157. http://doi.org/10.1016/j.jneumeth.2007.12.010

Neto, J. P., Lopes, G., Frazão, J., Nogueira, J., Lacerda, P., Baião, P., ... Kampff, A. R. (2016). Validating silicon polytrodes with paired juxtacellular recordings: method and dataset. *Journal of Neurophysiology*, *116*(2), 892–903. http://doi.org/10.1152/jn.00103.2016

Nicolelis, M. A. ., Ghazanfar, A. A., Faggin, B. M., Votaw, S., & Oliveira, L. M. . (1997). Reconstructing the Engram: Simultaneous, Multisite, Many Single Neuron Recordings. *Neuron*, *18*(4), 529–537. http://doi.org/10.1016/S0896-6273(00)80295-0

Nicolelis, M. A. L. (2011). *Beyond Boundaries: the new neuroscience of connecting brains with machines - and how it will change our lives*. New York: St. Martins's Griffin.

Nicolelis, M. A. L., Dimitrov, D., Carmena, J. M., Crist, R., Lehew, G., Kralik, J. D., & Wise, S. P. (2003). Chronic, multisite, multielectrode recordings in macaque monkeys. *Pnas*, *100*(19), 11041–11046. http://doi.org/10.1073/pnas.1934665100

Nordhausen, C. T., Maynard, E. M., & Normann, R. A. (1996). Single unit recording capabilities of a 100 microelectrode array. *Brain Research*, *726*(1–2), 129–140. http://doi.org/10.1016/S0006-8993(96)00321-6

Nunez, P. L., & Srinivasan, R. (2009). *Electric Fields of the Brain: The neurophysics of EEG*. *Electric Fields of the Brain: The neurophysics of EEG*. http://doi.org/10.1093/acprof:oso/9780195050387.001.0001

O'Doherty, J. E., Lebedev, M. A., Ifft, P. J., Zhuang, K. Z., Shokur, S., Bleuler, H., ... Nicolelis, M. A. L. (2011). Active tactile exploration enabled by a brain-machine-brain interface. *Nature*, *479*(7372), 228–231. http://doi.org/10.1038/nature10489

O'Keefe, J., & Dostrovsky, J. (1971). The hippocampus as a spatial map. Preliminary evidence from unit activity in the freely-moving rat. *Brain Research*, *34*(1), 171–175. http://doi.org/10.1016/0006-8993(71)90358-1

O'Keefe, J., & Recce, M. L. (1993). Phase relationship between hippocampal place units and the EEG theta rhythm. *Hippocampus*, *3*(3), 317–330. http://doi.org/10.1002/hipo.450030307

Obien, M. E. J., Deligkaris, K., Bullmann, T., Bakkum, D. J., & Frey, U. (2015). Revealing neuronal function through microelectrode array recordings. *Frontiers in Neuroscience*, *8*(JAN), 423. http://doi.org/10.3389/fnins.2014.00423

Open Ephys. (2017). Headstages — Open Ephys. Retrieved September 6, 2017, from http://www.open-ephys.org/headstages/

Pachitariu, M., Steinmetz, N., Kadir, S., Carandini, M., & Harris, K. D. (2016). *Kilosort: realtime spike-sorting for extracellular electrophysiology with hundreds of channels. bioRxiv*. Cold Spring Harbor Labs Journals. http://doi.org/10.1101/061481

Pagliardini, S., Gosgnach, S., & Dickson, C. T. (2013). Spontaneous Sleep-Like Brain State Alternations and Breathing Characteristics in Urethane Anesthetized Mice. *PLoS ONE*, *8*(7), e70411. http://doi.org/10.1371/journal.pone.0070411

Paxinos, G., & Watson, C. (2007). *The rat brain in stereotaxic coordinates* (6th ed.). Elsevier.

Petreanu, L., Gutnisky, D. A., Huber, D., Xu, N., O'Connor, D. H., Tian, L., ... Svoboda, K. (2012). Activity in motor–sensory projections reveals distributed coding in somatosensation. *Nature*, *489*(7415), 299–303. http://doi.org/10.1038/nature11321

Pettersen, K. H., Lindén, H., Dale, A. M., & Einevoll, G. T. (2010). Extracellular spikes and current-source density. In *Handbook of Neural Activity Measurement*.

Quian Quiroga, R., & Panzeri, S. (2009). Extracting information from neuronal populations: information theory and decoding approaches. *Nature Reviews. Neuroscience*, *10*(3), 173–85. http://doi.org/10.1038/nrn2578

Quinn, C. J., Coleman, T. P., Kiyavash, N., & Hatsopoulos, N. G. (2010). Estimating the directed information to infer causal relationships in ensemble neural spike train recordings. *Journal of Computational Neuroscience*, *30*(1), 17–44. http://doi.org/10.1007/s10827-010-0247-2

Quiroga, R. Q., Nadasdy, Z., & Ben-Shaul, Y. (2004). Unsupervised spike detection and sorting with wavelets and superparamagnetic clustering. *Neural Computation*, *16*(8), 1661–87. http://doi.org/10.1162/089976604774201631

Raducanu, B. C., Yazicioglu, R. F., Lopez, C. M., Ballini, M., Putzeys, J., Wang, S., ... Mitra, S. (2016). Time multiplexed active neural probe with 678 parallel recording sites. In *European Solid-State Device Research Conference* (Vol. 2016–Octob, pp. 385–388). IEEE.

http://doi.org/10.1109/ESSDERC.2016.7599667

Raducanu, B. C., Yazicioglu, R. F., Lopez, C. M., Ballini, M., Putzeys, J., Wang, S., ... Mitra, S. (2017). Time Multiplexed Active Neural Probe with 1356 Parallel Recording Sites. *Sensors*, *17*(10), 2388. http://doi.org/10.3390/s17102388

Rajangam, S., Tseng, P.-H., Yin, A., Lehew, G., Schwarz, D., Lebedev, M. A., & Nicolelis, M. A. L. (2016). Wireless Cortical Brain-Machine Interface for Whole-Body Navigation in Primates. *Scientific Reports*, *6*(1), 22170. http://doi.org/10.1038/srep22170

Ramon y Cajal, S. (1899). *Texture of the Nervous System of Man and the Vertebrates* (Vol. 1). Madrid: Imprenta Y Libreria De Nicolas Moya. http://doi.org/10.1016/S0090-3019(03)00249-0

Ramon y Cajal, S. (1923). Recuerdos de mi vida. *Juan Pueyo, Madrid*. Retrieved from http://scholar.google.com/scholar?hl=en&btnG=Search&q=intitle:Recuerdos+de+mi+vida#2

Ray Cooper. (1971). *Recording Changes in Electrical Properties in the Brain in Methods of Psychobiology*. (R. D. Myers, Ed.) (Volume 1). London and New York: Academic Press.

Rey, H. G., Pedreira, C., & Quian Quiroga, R. (2015). Past, present and future of spike sorting techniques. *Brain Research Bulletin*. http://doi.org/10.1016/j.brainresbull.2015.04.007

Rios, G., Lubenov, E. V., Chi, D., Roukes, M. L., & Siapas, A. G. (2016). Nanofabricated Neural Probes for Dense 3-D Recordings of Brain Activity. *Nano Letters*, *16*(11), 6857–6862. http://doi.org/10.1021/acs.nanolett.6b02673

Rivnay, J., Wang, H., Fenno, L., Deisseroth, K., & Malliaras, G. G. (2017). Next-generation probes, particles, and proteins for neural interfacing. *Science Advances*, *3*(6), e1601649. http://doi.org/10.1126/sciadv.1601649

Robinson, A. L. (1984). CMOS Future for Microelectronic Circuits: Low power consumption of complementary metal-oxide-semiconductor integrated circuits drives next stage of ultraminiaturization. *Science*, *224*(4650), 705–707. http://doi.org/224/4650/705 [pii]\r10.1126/science.224.4650.705

Robinson, D. A. (1968). The electrical properties of metal microelectrodes. *Proceedings of the IEEE*, *56*(6), 1065–1071. http://doi.org/10.1109/PROC.1968.6458

Rossant, C., Kadir, S. N., Goodman, D. F. M., Schulman, J., Belluscio, M., Buzsaki, G., & Harris, K. D. (2015). *Spike sorting for large, dense electrode arrays*. *bioRxiv*. Cold Spring Harbor Labs Journals. http://doi.org/10.1101/015198

Rossant, C., Kadir, S. N., Goodman, D. F. M., Schulman, J., Hunter, M. L. D., Saleem, A. B., ... Harris, K. D. (2016). Spike sorting for large, dense electrode arrays. *Nature*

Neuroscience, *19*(4), 634–641. http://doi.org/10.1038/nn.4268

Ruiz-Mejias, M., Ciria-Suarez, L., Mattia, M., & Sanchez-Vives, M. V. (2011). Slow and fast rhythms generated in the cerebral cortex of the anesthetized mouse. *Journal of Neurophysiology*, *106*(6), 2910–2921. http://doi.org/10.1152/jn.00440.2011

Ruther, P., & Paul, O. (2015). New approaches for CMOS-based devices for large-scale neural recording. *Current Opinion in Neurobiology*, *32*, 31–37. http://doi.org/10.1016/j.conb.2014.10.007

Santos, L., Neto, J. P., Crespo, A., Baião, P., Barquinha, P., Pereira, L., ... Fortunato, E. (2015). Electrodeposition of WO3 Nanoparticles for Sensing Applications. In *Electroplating of Nanostructures*. InTech. http://doi.org/10.5772/61216

Santos, L., Neto, J. P., Crespo, A., Nunes, D., Costa, N., Fonseca, I. M., ... Fortunato, E. (2014). WO 3 Nanoparticle-Based Conformable pH Sensor. *ACS Applied Materials & Interfaces*, *6*(15), 12226–12234. http://doi.org/10.1021/am501724h

Santos, L., Silveira, C. M., Elangovan, E., Neto, J. P., Nunes, D., Pereira, L., ... Fortunato, E. (2016). Synthesis of WO3 nanoparticles for biosensing applications. *Sensors and Actuators B: Chemical*, *223*, 186–194. http://doi.org/10.1016/j.snb.2015.09.046

Santucci, D. M., Kralik, J. D., Lebedev, M. A., & Nicolelis, M. A. L. (2005). Frontal and parietal cortical ensembles predict single-trial muscle activity during reaching movements in primates. *European Journal of Neuroscience*, *22*(6), 1529–1540. http://doi.org/10.1111/j.1460-9568.2005.04320.x

Scholten, K., & Meng, E. (2016). Electron-beam lithography for polymer bioMEMS with submicron features. *Microsystems & Nanoengineering*, *2*, 16053. http://doi.org/10.1038/micronano.2016.53

Scholvin, J., Kinney, J. P., Bernstein, J. G., Moore-Kochlacs, C., Kopell, N., Fonstad, C. G., & Boyden, E. S. (2016). Close-packed silicon microelectrodes for scalable spatially oversampled neural recording. *IEEE Transactions on Biomedical Engineering*, *63*(1), 120–130. http://doi.org/10.1109/TBME.2015.2406113

Schomburg, E. W., Anastassiou, C. a, Buzsáki, G., & Koch, C. (2012). The spiking component of oscillatory extracellular potentials in the rat hippocampus. *The Journal of Neuroscience : The Official Journal of the Society for Neuroscience*, *32*(34), 11798–811. http://doi.org/10.1523/JNEUROSCI.0656-12.2012

Schwarz, D. A., Lebedev, M. A., Hanson, T. L., Dimitrov, D. F., Lehew, G., Meloy, J., ... Nicolelis, M. A. L. (2014). Chronic, wireless recordings of large-scale brain activity in freely moving rhesus monkeys. *Nature Methods*, *11*(6), 670–676.

http://doi.org/10.1038/nmeth.2936

Scott, K. M., Du, J., Lester, H. a, & Masmanidis, S. C. (2012). Variability of acute extracellular action potential measurements with multisite silicon probes. *Journal of Neuroscience Methods*, *211*(1), 22–30. http://doi.org/10.1016/j.jneumeth.2012.08.005

Seymour, J. P., Wu, F., Wise, K. D., & Yoon, E. (2017). State-of-the-art MEMS and microsystem tools for brain research. *Microsystems & Nanoengineering*, *3*, 16066. http://doi.org/10.1038/micronano.2016.66

Shobe, J. L., Claar, L. D., Parhami, S., Bakhurin, K. I., & Masmanidis, S. C. (2015a). Brain activity mapping at multiple scales with silicon microprobes containing 1,024 electrodes. *Journal of Neurophysiology*, *114*(3).

Shobe, J. L., Claar, L. D., Parhami, S., Bakhurin, K. I., & Masmanidis, S. C. (2015b). Brain activity mapping at multiple scales with silicon microprobes containing 1024 electrodes. *Journal of Neurophysiology*, *114*(3), 2043–52. http://doi.org/10.1152/jn.00464.2015

Shoham, S., O'Connor, D. H., & Segev, R. (2006). How silent is the brain: is there a "dark matter" problem in neuroscience? *Journal of Comparative Physiology. A, Neuroethology, Sensory, Neural, and Behavioral Physiology*, *192*(8), 777–84. http://doi.org/10.1007/s00359-006-0117-6

Shu, Y., Duque, A., Yu, Y., Haider, B., & McCormick, D. A. (2007). Properties of Action-Potential Initiation in Neocortical Pyramidal Cells: Evidence From Whole Cell Axon Recordings. *Journal of Neurophysiology*, *97*(1), 746–760. http://doi.org/10.1152/jn.00922.2006

Somogyvári, Z., Cserpán, D., Ulbert, I., & Érdi, P. (2012). Localization of single-cell current sources based on extracellular potential patterns: the spike CSD method. *European Journal of Neuroscience*, *36*(10), 3299–3313. http://doi.org/10.1111/j.1460-9568.2012.08249.x

Stein, R. B., Weber, D. J., Aoyagi, Y., Prochazka, A., Wagenaar, J. B. M., Shoham, S., & Normann, R. A. (2004). Coding of position by simultaneously recorded sensory neurones in the cat dorsal root ganglion. *The Journal of Physiology*, *560*(Pt 3), 883–896. http://doi.org/10.1113/jphysiol.2004.068668

Steinmetz, N. A. (2016). NeuroPixel project. Retrieved from http://data.cortexlab.net/dualPhase3/

Stevenson, I. (2017). Tracking Advances in Neural Recording. Retrieved June 19, 2017, from http://stevenson.lab.uconn.edu/scaling/

Stevenson, I. H., & Kording, K. P. (2011). How advances in neural recording affect data analysis. *Nature Neuroscience*, *14*(2), 139–142. http://doi.org/10.1038/nn.2731

Suner, S., Fellows, M. R., Vargas-Irwin, C., Nakata, G. K., & Donoghue, J. P. (2005). Reliability of signals from a chronically implanted, silicon-based electrode array in non-human primate primary motor cortex. *IEEE Transactions on Neural Systems and Rehabilitation Engineering : A Publication of the IEEE Engineering in Medicine and Biology Society*, *13*(4), 524–41. http://doi.org/10.1109/TNSRE.2005.857687

Takahashi, K., & Matsuo, T. (1984). Integration of multi-microelectrode and interface circuits by silicon planar and three-dimensional fabrication technology. *Sensors and Actuators*, *5*(1), 89–99. http://doi.org/10.1016/0250-6874(84)87009-2

Theuwissen, A. (2007). CMOS image sensors: State-of-the-art and future perspectives. In *ESSCIRC 2007 - 33rd European Solid-State Circuits Conference* (pp. 21–27). IEEE. http://doi.org/10.1109/ESSCIRC.2007.4430242

Tønnesen, J., Inavalli, V. V. G. K., & Nägerl, U. V. (2018). Super-Resolution Imaging of the Extracellular Space in Living Brain Tissue. *Cell*, *172*(5), 1108–1121.e15. http://doi.org/10.1016/j.cell.2018.02.007

Truccolo, W., Donoghue, J. A., Hochberg, L. R., Eskandar, E. N., Madsen, J. R., Anderson, W. S., ... Cash, S. S. (2011). Single-neuron dynamics in human focal epilepsy. *Nature neurOSCIenCe*, *14*(5). http://doi.org/10.1038/nn.2782

Vargas-Irwin, C. E., Shakhnarovich, G., Yadollahpour, P., Mislow, J. M. K., Black, M. J., & Donoghue, J. P. (2010). Decoding Complete Reach and Grasp Actions from Local Primary Motor Cortex Populations. *Journal of Neuroscience*, *30*(29). Retrieved from http://www.jneurosci.org/content/30/29/9659?ijkey=79c742f1de8144a8ab9a03c732afe663a1b1a9f6&keytype2=tf_ipsecsha

Veigas, B., Fortunato, E., & Baptista, P. V. (2015). Field effect sensors for nucleic Acid detection: recent advances and future perspectives. *Sensors (Basel, Switzerland)*, *15*(5), 10380–10398. http://doi.org/10.3390/s150510380

Velliste, M., Perel, S., Spalding, M. C., Whitford, A. S., & Schwartz, A. B. (2008). Cortical control of a prosthetic arm for self-feeding. *Nature*, *453*(7198), 1098–1101. http://doi.org/10.1038/nature06996

Wehr, M., Pezaris, J. S., & Sahani, M. (1999). Simultaneous paired intracellular and tetrode recordings for evaluating the performance of spike sorting algorithms. *Neurocomputing*, *26–27*, 1061–1068. http://doi.org/10.1016/S0925-2312(99)00105-8

Wessberg, J., Stambaugh, C. R., Kralik, J. D., Beck, P. D., Laubach, M., Chapin, J. K., ... Nicolelis, M. A. (2000). Real-time prediction of hand trajectory by ensembles of cortical neurons in primates. *Nature*, *408*(6810), 361–5. http://doi.org/10.1038/35042582

Wilson, M., & McNaughton, B. (1993). Dynamics of the hippocampal ensemble code for space. *Science*, *261*(5124), 1055–1058. http://doi.org/10.1126/science.8351520

Wise, D. K., & Ji, J. (1992). An Implantable CMOS Circuit Interface for Multiplexed Microelectrode Recording Arrays. *IEEE Journal of Solid-State Circuits*, *27*(3), 433–443. http://doi.org/10.1109/4.121568

Wise, K. D., Angell, J. B., & Starr, A. (1970). s. *IEEE Transactions on Biomedical Engineering*, *BME-17*(3), 238–247. http://doi.org/10.1109/TBME.1970.4502738

Yger, P., Spampinato, G. L. B., & Esposito, E. (2016). Fast and accurate spike sorting in vitro and in vivo for up to thousands of electrodes. *bioRxiv*, 1–21. http://doi.org/10.1101/067843

Yuste, R. (2015). From the neuron doctrine to neural networks. *Nature Reviews Neuroscience*, *16*(8), 487–497. http://doi.org/10.1038/nrn3962

Zacksenhouse, M., Lebedev, M. A., Carmena, J. M., O'Doherty, J. E., Henriquez, C., & Nicolelis, M. A. L. (2007). Cortical Modulations Increase in Early Sessions with Brain-Machine Interface. *PLoS ONE*, *2*(7), e619. http://doi.org/10.1371/journal.pone.0000619

Zhao, Z., Gong, R., Zheng, L., & Wang, J. (2016). In vivo neural recording and electrochemical performance of microelectrode arrays modified by rough-surfaced aupt alloy nanoparticles with nanoporosity. *Sensors (Switzerland)*, *16*(11), 1851. http://doi.org/10.3390/s16111851

Appendix A

The Appendix A provides complementary information about the dataset used to generate Figure 2.9b in Chapter 2. We observed that extracellular neural probes are fabricated with increasing number of microelectrodes and the majority of the studies did not use polytrodes.

Table A.1 Literature data used to investigate the relationship between the number of electrodes in neural probes and the number of neurons simultaneously recorded. For each individual study we described the number of electrodes, the number of neurons simultaneously recorded and the type of neural probe. In the neural probe type, microwires represent microwire bundles or microwire arrays, and silicon represents polytrodes.

Work	Year	Electrodes number	Neurons number	Neural probe
(Wilson & McNaughton, 1993)	1993	48	148	Tetrodes
(Nordhausen, Maynard, & Normann, 1996)	1996	100	196	Utah
(Nicolelis, Ghazanfar, Faggin, Votaw, & Oliveira, 1997)	1997	48	100	Microwires
(Wessberg et al., 2000)	2000	96	100	Microwires
(Csicsvari et al., 2003)	2003	64	120	Microwires
(Nicolelis et al., 2003)	2003	384	247	Microwires
(Hatsopoulos, Joshi, & O'Leary, 2004),	2004	200	143	Utah
(Barthó et al., 2004)	2004	64	144	Microwires
(Stein et al., 2004)	2004	100	100	Microwires
(Blanche, 2005)	2005	54	100	Silicon
(Lin et al., 2005)	2005	96	260	Stereotrodes
(Santucci, Kralik, Lebedev, & Nicolelis, 2005)	2005	64	147	Microwires
(Hatsopoulos, Xu, & Amit, 2007)	2007	96	145	Utah
(Zacksenhouse et al., 2007)	2007	96	183	Microwires
(Fujisawa, Amarasingham, Harrison, & Buzsáki, 2008)	2008	64	142	Microwires

(Velliste, Perel, Spalding, Whitford, & Schwartz, 2008)	2008	96	116	Utah
(Ganguly & Carmena, 2009)	2009	128	100	Microwires
(Fitzsimmons, 2009)	2009	128	334	Microwires
(Kim et al., 2009)	2009	96	192	Utah
(Kelly, Smith, Kass, & Lee, 2010)	2010	96	129	Utah
(Quinn, Coleman, Kiyavash, & Hatsopoulos, 2010)	2010	100	115	Utah
(Vargas-Irwin et al., 2010)	2010	96	122	Utah
(Truccolo et al., 2011)	2011	96	149	Utah
(O'Doherty et al., 2011)	2011	384	200	Microwires
(Kim, Kim, Hoffman-Kim, Song, & Palmore, 2011)	2011	96	99	Utah
(Churchland et al., 2012)	2012	192	218	Utah
(Fraser & Schwartz, 2012)	2012	96	106	Utah
(Ifft, Shokur, Li, Lebedev, & Nicolelis, 2013)	2013	768	497	Microwires
(Aggarwal, Mollazadeh, Davidson, Schieber, & Thakor, 2013)	2013	128	159	Microwires
(Schwarz et al., 2014)	2014	512	494	Microwires
(Goris, Movshon, & Simoncelli, 2014)	2014	96	136	Microwires
(Berényi et al., 2014)	2014	256	163	Silicon
(Shobe et al., 2015a)	2015	1024	315	Silicon
(Rajangam et al., 2016)	2016	256	144	Microwires
(Jun et al., 2017)	2017	768	741	Silicon

Appendix B

The Appendix B provides information about the dataset gathered to quantify the effect of electrode impedance on data quality. All experiments were performed with a commercially available 32-channel probe (A1x32-Poly3-5mm-25s-177-CM32, NeuroNexus), with 177 μm^2 electrodes and an inter-site pitch of 22-25 μm. Acute recordings from anesthetized rats are approximately 10 to 15 minutes long. Additionally, the recordings used to calculate the noise in saline and the electronic noise due to the recording system are also presented. This dataset is available online (http://www.kampff-lab.org).

Table B.1. Summary of the dataset used to quantify the effect of electrode impedance on data quality. For each recording (i.e., filename), we described the distance (depth) from the brain surface to the bottom electrode in the array, the estimated recorded brain region (M1 or CA1), the anaesthesia type (ketamine or urethane), and the number of putative neurons considered for each recording.

Filename	Depth (μm)	Brain region /Anaesthesia	Number of putative neurons
amplifier2015-05-05T17_20_09.bin	–	Short-circuit	–
amplifier2015-05-11T11_59_54.bin	–	Saline solution	–
amplifier2017-02-02T10_30_29.bin	–	Saline solution	–
amplifier2016-11-01T19_59_18.bin	–	Saline solution	–
amplifier2017-02-02T14_38_11.bin	715	M1 / urethane	4
amplifier2017-02-02T15_03_44.bin	915	M1 / urethane	7
amplifier2017-02-02T15_49_35.bin	1245	M1 / urethane	5
amplifier2017-02-02T16_57_16.bin	2149	Hippocampus / urethane	6
amplifier2017-02-02T17_18_46.bin	2243	Hippocampus / urethane	6
amplifier2014-11-13T14_59_40.bin	400	M1 / ketamine	10
amplifier2014-11-13T15_35_31.bin	700	M1 / ketamine	17
amplifier2014-11-13T18_05_50.bin	1100	M1 / ketamine	24
amplifier2014-11-25T20_32_48.bin	1300	M1 / ketamine	11
amplifier2014-11-25T21_27_13.bin	1400	M1 / ketamine	7
amplifier2014-11-25T23_00_08.bin	1300	M1 / ketamine	12

Appendix C

The Appendix C provides information about the datasets gathered using CMOS scanning neural probes and 256-channel probes. These datasets are available online (http://www.kampff-lab.org/)

Table C.1. Summary of the dataset used to validate CMOS-based probes. Acute recordings performed with different number of active groups, reference type configuration and recording depths. We targeted the brain regions under the stereotaxic coordinates, anterior-posterior -3.4 mm and medial-lateral 1.3 mm. The high-pass cut-off frequency for the AP mode was set to 500 Hz and the low-pass cut-off frequency for the LFP mode was set to 500 Hz. The bias voltage is a parameter that was adjusted for each recording depending mostly on the number of active groups.

Filename	Depth tip (mm)	Number of Active groups	Reference type	Time (min)	Bias voltage (V)
17_50_36.bin	6.7	2	Internal	1	2.25
17_52_36.bin	6.7	4	Internal	1	2.34
17_54_35.bin	6.7	6	Internal	1	2.37
17_56_25.bin	6.7	8	Internal	1	2.39
17_58_26.bin	6.7	10	Internal	15	2.425
18_15_12.bin	6.7	12	Internal	1	2.44
18_18_41.bin	6.7	2	External	1	2.3
18_20_31.bin	6.7	4	External	1	2.38
18_22_40.bin	6.7	6	External	1	2.4
18_24_20.bin	6.7	8	External	1	2.42
18_26_30.bin	6.7	10	External	15	2.43
18_40_36.bin	6.7	12	External	1	2.45
19_13_16.bin	7.6	12	Internal	15	2.43

Table C.2 Summary of the dataset gathered with the 256-channel probe. Acute recordings (30 minutes long) from anesthetized rats. The label indicates the recording positions identified in Figure 4.8a. The depth specifies the distance between the brain surface to the tip of the probe.

Label	Filename	Depth tip (mm)
Co1	amplifier2017-02-08T14_34_33.bin	0.6
Co2	amplifier2017-02-08T15_34_04.bin	0.7
Co3	amplifier2017-02-08T16_03_06.bin	0.8
H1	amplifier2017-02-08T18_06_19.bin	2.5
H2	amplifier2017-02-08T18_38_09.bin	3.3
H3	amplifier2017-02-08T20_04_54.bin	3.5
T1	amplifier2017-02-08T20_54_26.bin	4.6
T2	amplifier2017-02-08T21_38_55.bin	6.4
CR1	amplifier2017-02-16T15_37_59.bin	1.5
CR2	amplifier2017-02-16T16_14_15.bin	1.7
CR3	amplifier2017-02-16T16_58_01.bin	2.1
Co4	amplifier2017-02-23T14_38_33.bin	1.4
St1	amplifier2017-02-23T15_48_36.bin	3.8
St2	amplifier2017-02-23T17_29_48.bin	5.5
St3	amplifier2017-02-23T16_55_00.bin	5.6
CoP1	amplifier2017-02-23T18_25_19.bin	2.8
CoP2	amplifier2017-02-23T19_00_56.bin	3.2
CoP3	amplifier2017-02-23T19_36_39.bin	3.6

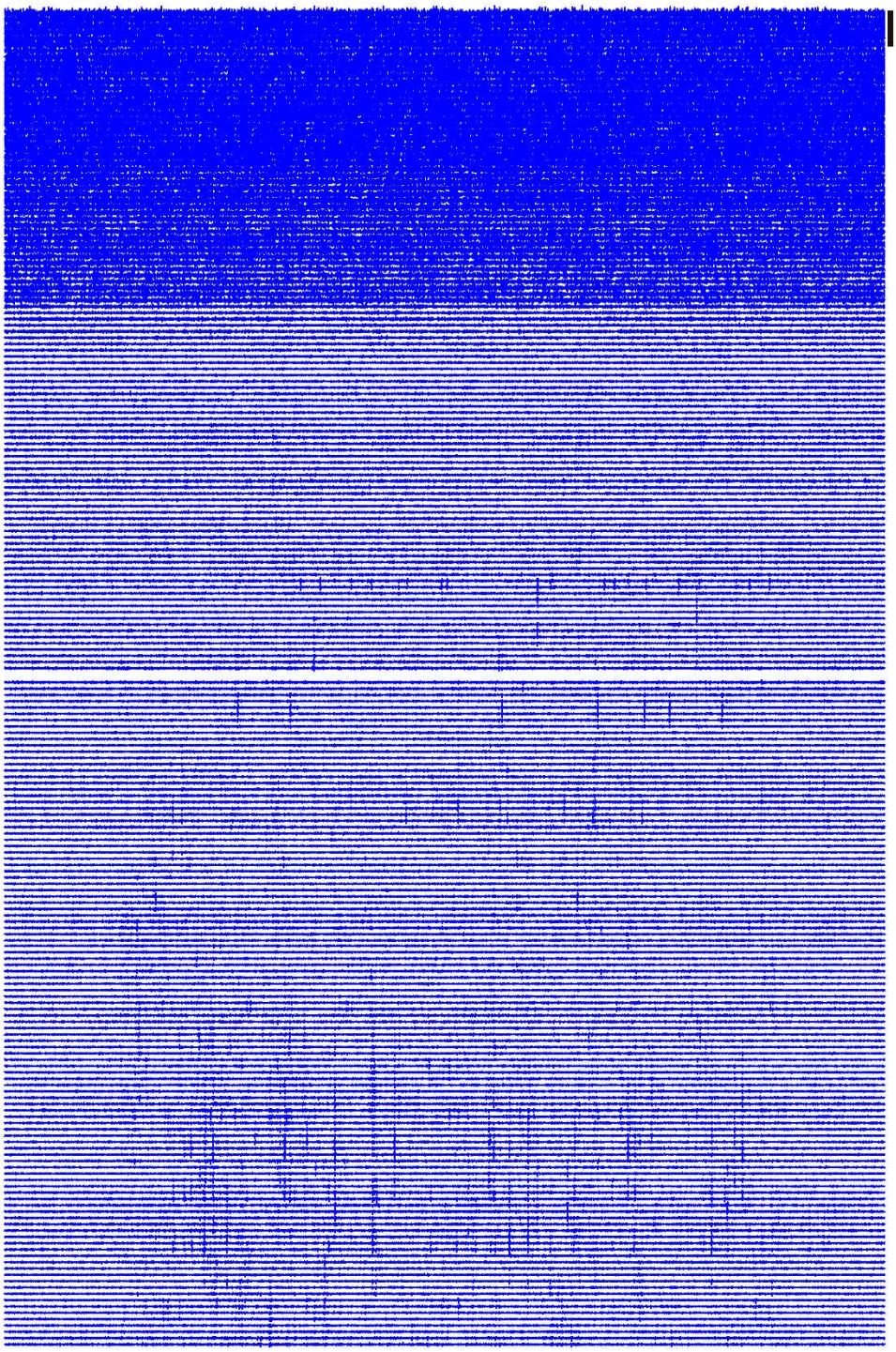

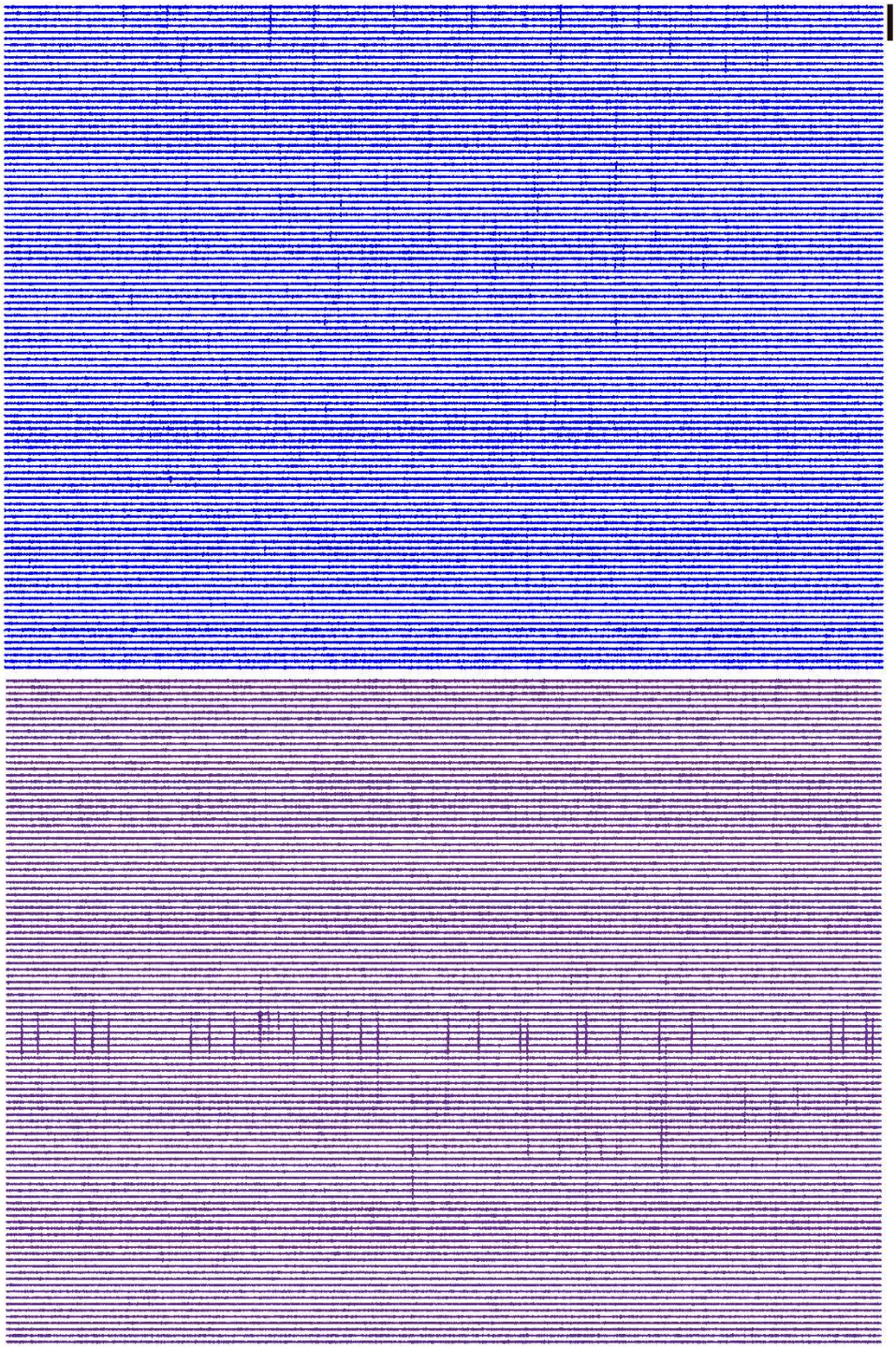

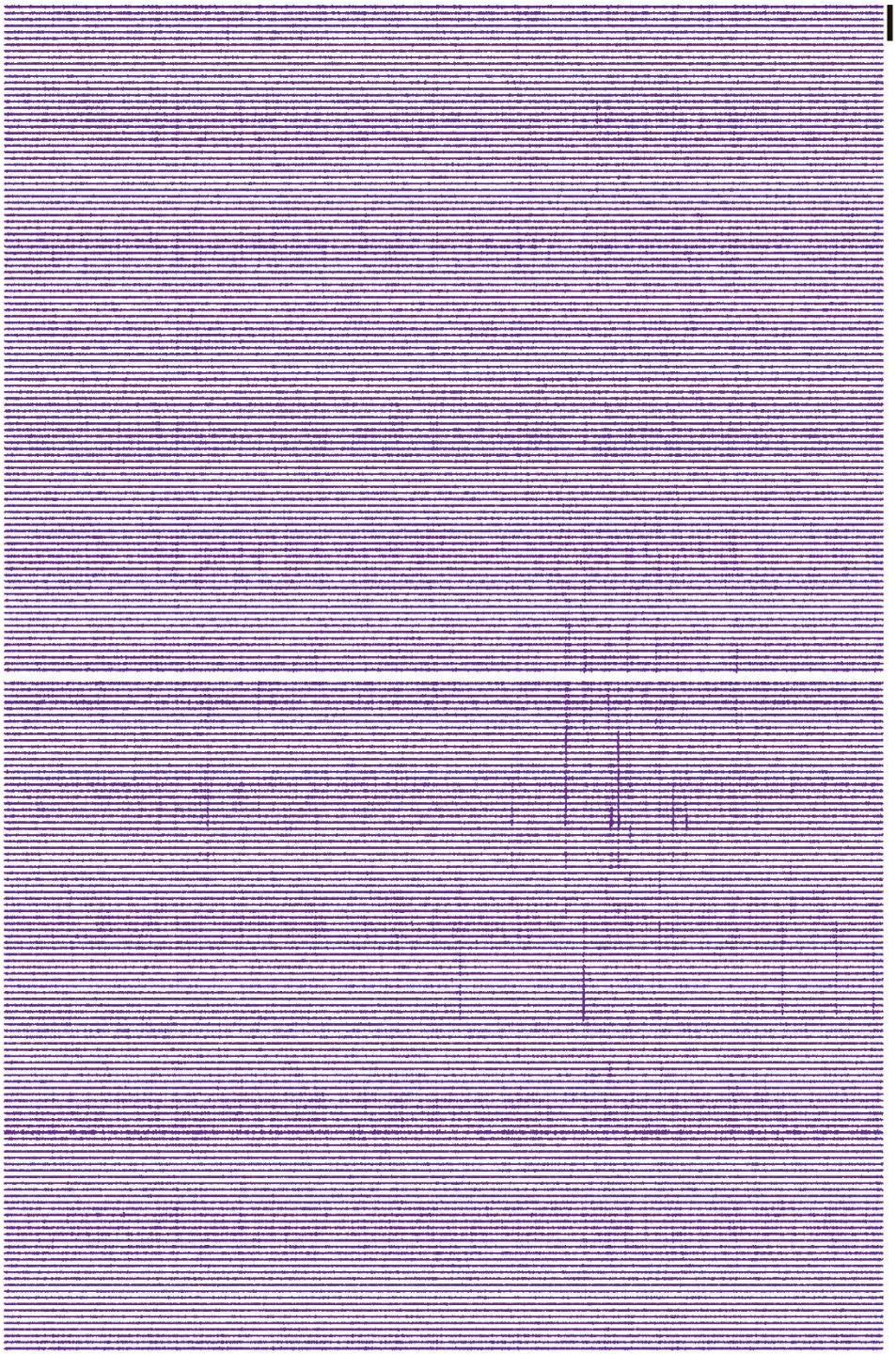

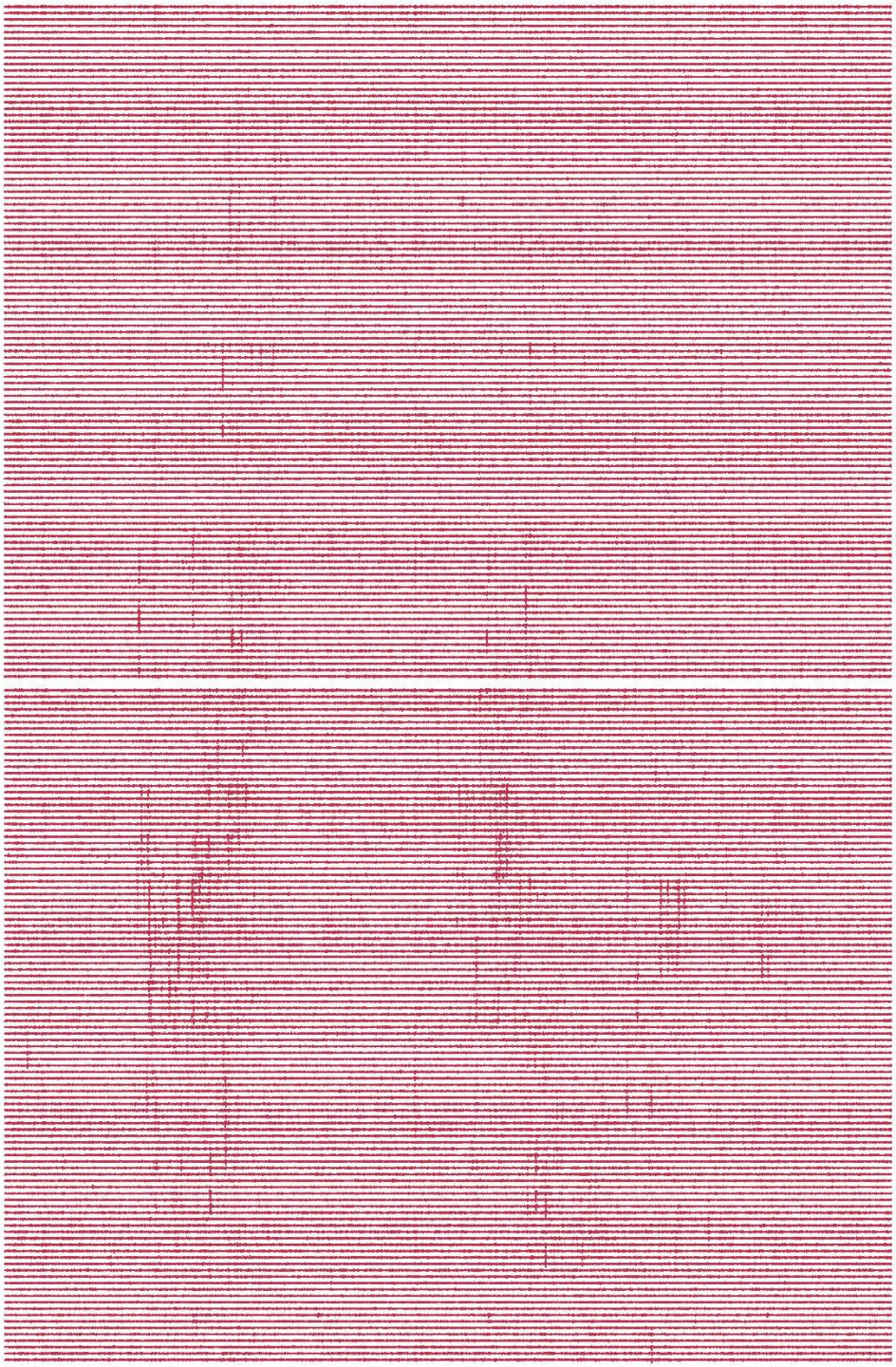

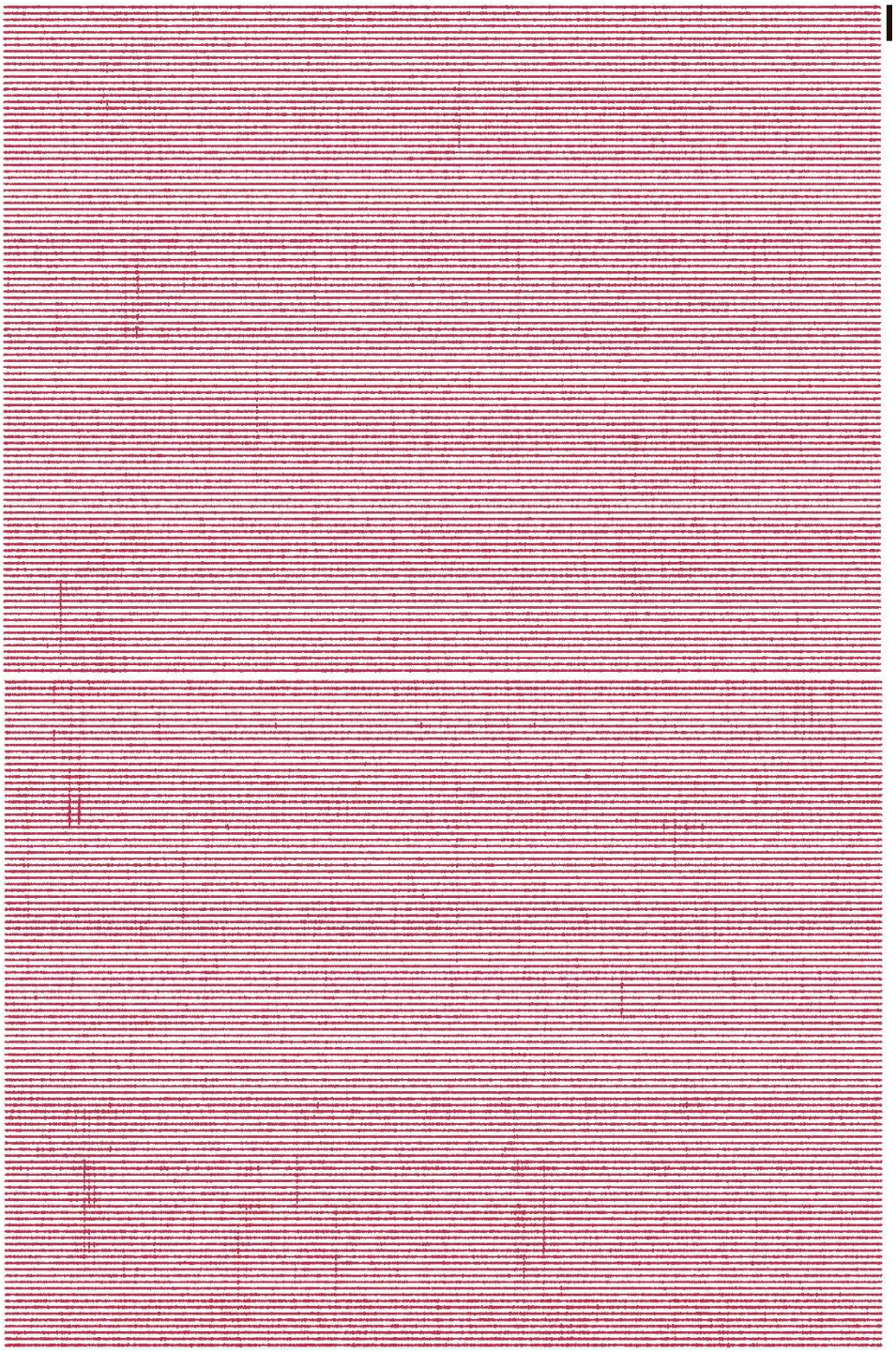

Figure C.1 Example of a recording (*18_26_30.bin*) segment performed by a CMOS scanning neural probe with 1060 electrodes set to AP mode. 500-ms-long AP traces from a probe spanning multiple brain regions (cortex shown in blue, hippocampus shown in purple and thalamus shown in red). In each page, two groups from the probe are represented; scale bar = 600 μm.